PROTON-PROTON CORRELATION FUNCTIONS MEASURED USING POSITION-SENSITIVE FAUST

A Dissertation

by

LAUREN ANN HEILBORN

Submitted to the Office of Graduate and Professional Studies of
Texas A&M University
in partial fulfillment of the requirements for the degree of

DOCTOR OF PHILOSOPHY

Chair of Committee,	Sherry J. Yennello
Committee Members,	Aldo Bonasera
	Charles M. Folden III
	Joseph B. Natowitz
Head of Department,	Simon North

December 2018

Major Subject: Chemistry

ABSTRACT

The nuclear Equation of State (nEoS) is important to a more fundamental understanding of nuclear matter, particularly in asymmetric systems such as neutron stars. Proton-proton (pp) correlation functions have been predicted to be sensitive to the density-dependence of the asymmetry energy in the nEoS in simulations using transport models. In order to examine this relationship, the Forward Array Using Silicon Technology (FAUST) has been commissioned with position-sensitive silicon detectors as the ΔE detectors to increase resolution in momentum space. The upgraded FAUST was used to measure charged particles produced in reactions of ^{40}Ar+^{58}Fe and ^{40}Ca+^{58}Ni at 40 MeV/u and ^{40}Ar+^{70}Zn and ^{40}Ar+^{58}Fe at 30 MeV/u. These systems were chosen in order to vary the neutron-proton asymmetry between systems of similar size. Light charged particle correlation functions and proton-proton correlation functions were extracted for all four of these systems. Correlation functions extracted from simulations using a Boltzmann-Uehling-Uhlenbeck transport model show no difference between soft and stiff parametrizations of the asymmetry energy. Comparisons of the strength of experimental proton-proton correlation functions amongst the same beam energy and the same system with varying system composition or energy provide another experimental observable for future comparison with simulation results.

DEDICATION

with thanks for the surprisingly obvious

ACKNOWLEDGMENTS

Thank you to the SJY group, particularly Alan McIntosh and Mike Youngs, without whom this work would not have been possible. Thank you especially to my advisor, Sherry Yennello, for her signature delivery of maddening freedom and guidance throughout my work. I would like to thank the Texas A&M University Cyclotron Institute staff for the excellent beam quality, shop time, and general support. It's lovely to work with such good people.

As for personal support, it is impossible to properly thank the people who have loved me deeply and well here. Thank you to my many roommates and friends who shared ice cream with me after long days or met up for coffee in the morning, particularly Jennifer Erchinger, Carrie Carpenter Werke, and Joanna Mullins. I am grateful to my church family at Bryan Nazarene for welcoming me with open arms and being grandparents, aunts, uncles, cousins and siblings as the need arose.

Deep thanks to my family for supporting my decision to move to Texas. Twice. For writing me letters and sending me packages on the days I needed them most, braving the heat to help me move multiple times, and encouraging me to persevere.

CONTRIBUTORS AND FUNDING SOURCES

Contributors

This work was supported by a dissertation committee consisting of Professor Sherry J. Yennello, Professor Charles M. Folden III and Professor Joseph B. Natowitz of the Department of Chemistry and Professor Aldo Bonasera of the Department of Physics.

Experimental data was collected with the help of the SJY group of the Cyclotron Institute. The pBUU calculations analyzed in section 4.4.2 were provided by Dr Michael D. Youngs with discussions with Dr Brent Barker. The HIPSE calculations used in chapter 4 were provided by Dr Jerome Gauthier.

The ASICs electronics were borrowed from and used successfully with guidance from the RET group at Texas A& M University and the Sobotka group at Washington University in St Louis.

Funding Sources

This work was made possible by supported from the Department of Energy (DE-FG02-93ER40773) and the Robert A. Welch Foundation (A-1266).

The ASICs were paid for by grant DE-SC0004972.

TABLE OF CONTENTS

Page

LIST OF FIGURES

FIGURE Page

LIST OF TABLES

TABLE Page

1 INTRODUCTION AND MOTIVATION

1.1 Asymmetry-Dependence of Nuclear Equation of State

The nuclear equation of state (nEoS) is of general interest for fundamental understanding of nuclear physics and astrophysics. This equation describes the relationship between density, pressure, temperature, energy, and chemical potential of nuclear material. Normal nuclear matter (cold beta-stable nuclear material near saturation density) can be interrogated by looking at the thickness of neutron skins [1], dipole resonances and monopole resonances [2, 3]. In addition to the energetics of near-ground state nuclei, the nEoS describes the behavior of nuclear matter over a wide variety of thermodynamic properties. Nuclei are described at varying temperatures, at asymmetries like in neutron stars and nuclei close to the neutron dripline, and densities near and far from saturation density [4]. Nuclear matter in astrophysical environments, such as neutron stars and Type Ia supernovae, are in very different regimes for temperature, pressure, and isospin asymmetry than normal nuclear matter in its ground state [5, 6, 7, 8]. Very asymmetric (N≠Z) systems, such as neutron stars and nuclei close to the neutron dripline are also described, with a dependence upon the neutron-proton asymmetry. The zero-temperature nEoS can be expressed for a nucleus in parabolic form, the binding energy per nucleon as a function of proton-neutron asymmetry($\Delta \equiv (N-Z)/A$) and density (ρ) is written as an expansion around $\Delta = 0$ as [4]:

$$\frac{E}{A}(\rho, \Delta) = \frac{E}{A}(\rho) + \frac{E_{asy}}{A}(\rho)\Delta^2. \tag{1.1}$$

The first term of equation 1.1 represents the binding energy of symmetric nuclear matter (SNM, N=Z), and depends upon density. The asymmetry energy[1] term depends upon the isospin asymmetry, which is well understood near normal nuclear density (0.16 fm^{-3}), but less well constrained away from normal nuclear density. This dissertation will focus on subsaturation densities. The

[1] Although this has often been called the "symmetry energy", this term is poorly named in that it refers to the energy destabilization due to the neutron-proton asymmetry of the nucleus.

second term accounts for neutron-proton asymmetry, and depends upon Δ and ρ [4].

Figure 1.1 shows Equation 1.1, plotted as a function of nuclear density, for representatives of microscopic, variational and phenomenological calculations, for pure neutron matter (top curves) and SNM (bottom curves) [9]. The differences between these various approaches need to be constrained by experiment and observation. The binding energy of the pure neutron matter is always positive and increases with density for all models; pure neutron matter is unbound. The binding energy of SNM dips below zero at very low density, reaches a minimum near saturation density, where SNM is most bound, and then increases towards zero density and with increasing density.

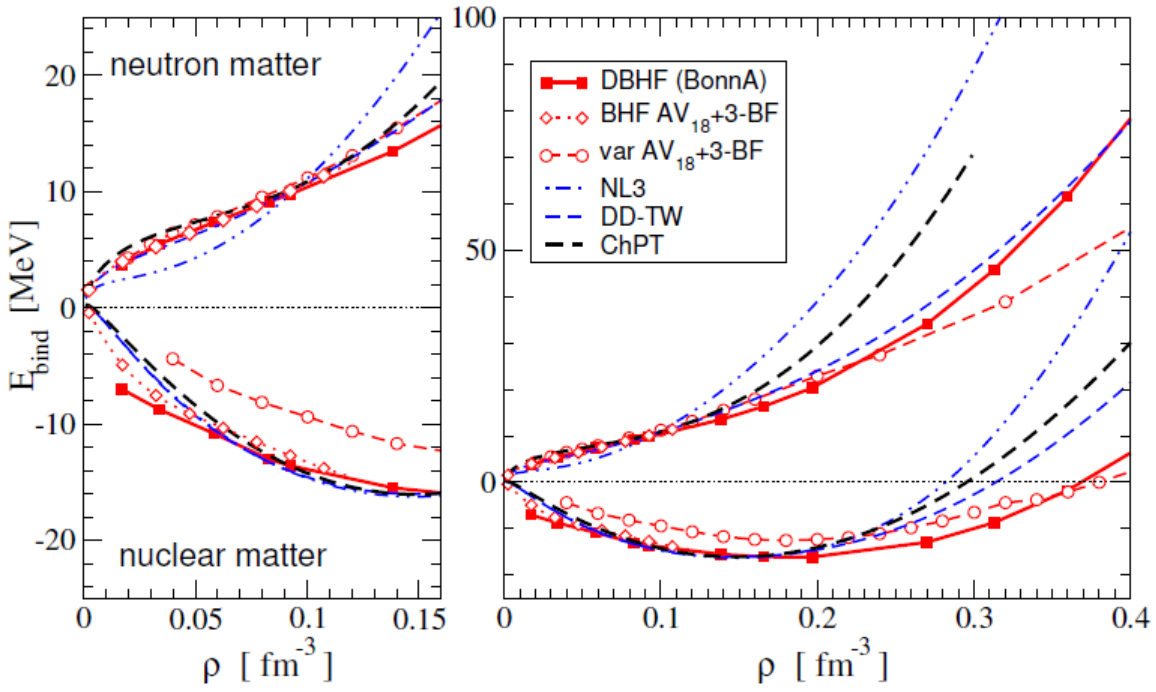

Figure 1.1: The binding energy from Eq. 1.1 calculated from various microscopic microscopic models for pure neutron matter (Z=0, top set of curves on left and right panels) and SNM (N=Z, bottom set of curves in left and right panels) for different methods of calculation. The same curves are plotted in the left and right panels, the left hand side is simply zoomed in below saturation density. Reprinted from [9].

The difference between the curves calculated for the neutron matter and SNM gives the asym-

metry energy term, which is also density-dependent. Pressures that move the density of nuclear matter far from saturation density (ρ_0=0.16 fm^{-3}) are important to nuclear reactions in astrophysical systems such as neutron stars. Temperatures higher than those experienced by normal nuclear matter are also of interest. These conditions are difficult to obtain terrestrially. In the laboratory, densities above and below normal nuclear density are reached through heavy-ion collisions. Comparison of these experimental data to meaningful and reasonable theoretical calculations is desirable, as transport models and microscopic calculations can vary widely in their predictions. Some such calculations are shown in Figures 1.1 and 1.2 [9]. Figure 1.2 shows the difference between the upper and lower curves on Figure 1.1 of E_{asy}, from equation 1.1, plotted as a function of reduced density of nuclear matter.

The density-dependence of E_{asy} is often referred to as being either "soft" or "stiff". A stiff density-dependence refers to a formulation of the asymmetry energy that has a dependence upon density which remains the same or increases at high densities, such as the NL3 or ChPT lines on Figure 1.2. A softer density-dependence of the asymmetry energy has a slope of asymmetry energy vs. density which decreases at higher densities, such as the SKM* or SkLya lines on Figure 1.2. The interactions labeled "soft" or "stiff" can vary widely between models, and are most meaningful when used to compare two different parametrizations of the asymmetry energy within the same code. The interactions mentioned in Figure 1.2 suggest that E_{asy} goes to 0 MeV as the density approaches zero. However, experimental evidence indicates that, due to clustering, E_{asy} reaches a finite value in the vicinity of 10 MeV as the density approaches zero [10].

In nuclear reactions, temperatures and densities over the range of these parametrizations can be reached. In particular, the asymmetry energy can affect the sizes and velocities of fragments resulting from the multifragmentation of an excited nucleus. Many different observables from this process have been proposed and investigated for the purpose of constraining this asymmetry term, including competition of reaction mechanisms, collective flows, and correlation functions [4]. Astrophysical measurements such as neutron star masses and radii also contribute to our knowledge of the nEoS, so constraints from both reactions and astronomical measurements are

used in concert [9]. Proton-proton (pp) correlation functions are the observable chosen for this work because they have been predicted to be sensitive to the asymmetry energy [11].

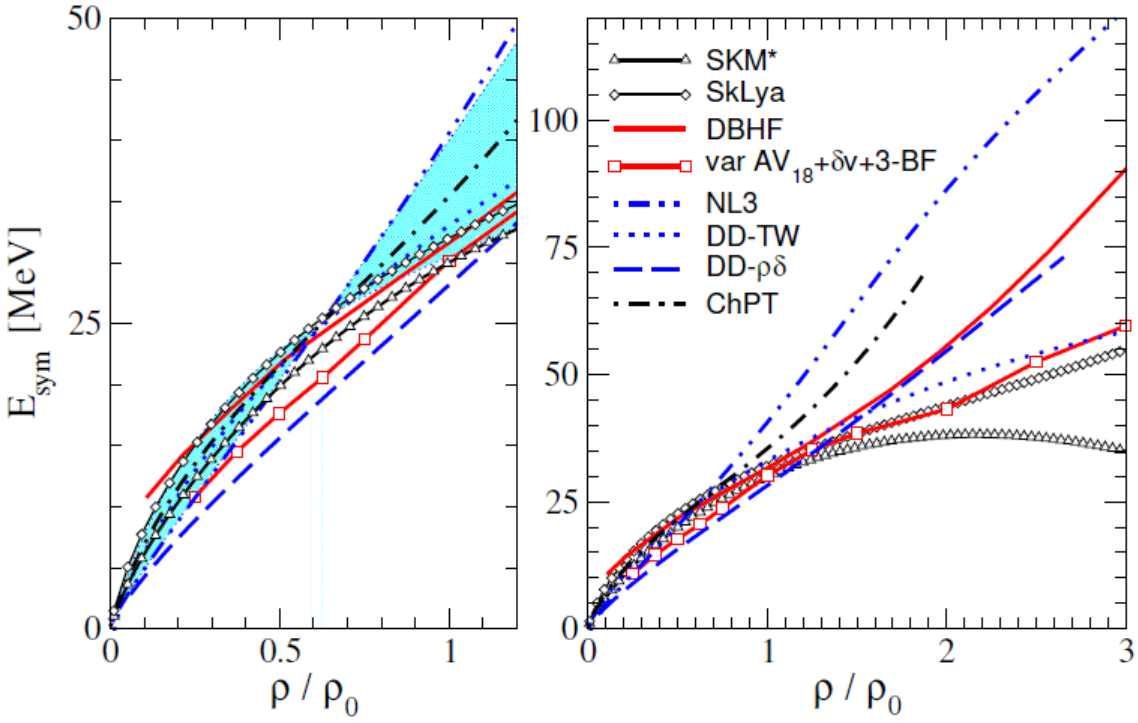

Figure 1.2: The asymmetry energy contribution (second term) of different parametrizations of the nEoS from Equation 1.1. Reprinted from [9].

1.2 Interferometry

The interpretation of pp correlation functions comes from interferometry, which uses the interference of two waves to extract information about the waves, about their path, or about their prior interactions. The basis for amplitide interferometry (used in a Michelson interferometer [12]) comes from Young's double-slit experiment, which showed the wave-particle duality of light from the interference pattern formed by the destructive and constructive interference, of a photon passing through two slits [13, 14]. This amplitude interferometry has limited use in astronomy due to phase-shifting as a result of photons passing through the earth's atmosphere.

Hanbury-Brown and Twiss first used intensity interferometry, which is not sensitive to these distortions, to calculate the diameter of distant stellar objects in the 1950s by using two photon detectors, placed a large distance apart [15]. In intensity interferometry, schematically illustrated in figure 1.3, two photons are emitted from the excited source on the left, which could be an excited nucleus, a star or a galaxy. Both photons contribute to the intensity readings at two disparate points in space [16]. These contributions are depicted in a naive way in this figure by the dotted arrows. Photons are detected in coincidence in the two detectors after their interaction [17]. The correlation function can be defined as a function of photon momentum [16]. The symmetrization of the wavefunctions of individual photons causes interference even in the absence of other interactions. This interference and the resultant intensities at the two detectors allow the radius of the star to be determined [16].

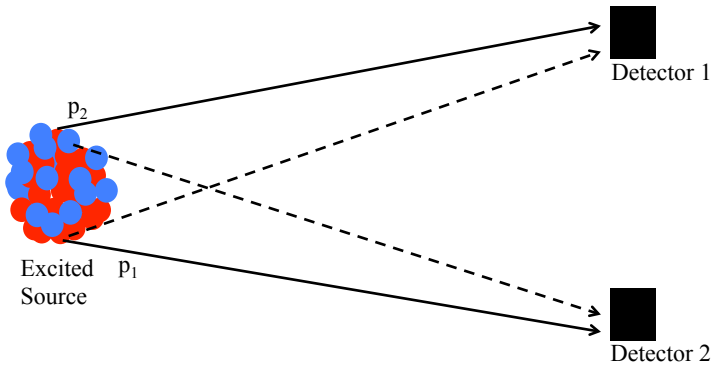

Figure 1.3: Two particles (p_1 and p_2) are emitted from the excited source on the left. The dashed and solid lines both apply for photons, due to interference. A coincidence can be measured at both detectors. These particles will interact and interfere with one another before detection at detector 1 and detector 2.

The wave-particle duality of all particles enables a similar measurement with fragments resulting from nuclear reactions [18]. Intensity interferometry has been used in nuclear physics to extract information about the spatial extent of the reaction volume, starting in high-energy experiments with information about antiproton-proton annihilations extracted from angular correlations

of π mesons [19].The particles emitted and detected in figure 1.3 could also be pions or protons. If the particles did not interact at all on their way to being detected in detector 1 and detector 2, the resulting yield in detector 1 at a specific energy would be the same regardless of the measurement in detector 2. The product of the singles yields in each of the two detectors alone would be equal to the yield of simultaneous measurements. Due to interactions, the yield is different in detector 1 if a specific energy is detected in detector 2 in this example. One way to see the difference in energy distributions of particles caused by correlations between the particles is to construct a correlation function, in this case for protons.

1.3 Definition of Correlation Function

The correlation function is constructed as a function of relative momentum between any two protons (q_{Rel}):

$$q_{Rel} = |\mathbf{q}_{Rel}| = \frac{1}{2}|\mathbf{p}_1 - \mathbf{p}_2|, \tag{1.2}$$

in order to account for the momenta of both protons in each of the myriad of different possible combinations of momenta. The correlation function is not defined for any pair of particles, but rather for the ensemble of particles [20, 21]. The theoretical formulation of this, the Koonin-Pratt equation is [22, 21]:

$$C(q_{Rel}) = 1 + R(q_{Rel}) = 1 + \int drS(\mathbf{r}) \cdot K(\mathbf{r}, \mathbf{q}), \tag{1.3}$$

where $C(q_{Rel})$ is the correlation function and $R(q_{Rel})$ is the degree of correlation, which goes to zero at infinite distance between the particles. S(r) is the source function, or the probability of emitting two protons, separated in time and space by the vector $\mathbf{r}$ [22]. This is usually assumed to be Gaussian in nature, although this may not always be the case [23]. The kernel function, K($\mathbf{r}$,$\mathbf{q}$), accounts for the interaction between the particles in question and includes the antisymmetrization of the two wavefunctions. The integral encompasses all angles and energies at which particles are emitted. The correlation function is defined using the three-momentum, but for the sake of notation, the vector notation will be implicit for the rest of this dissertation.

Protons interact through Coulomb, Pauli-blocking and antisymmetrization of wavefunctions.

The shape of the correlation function results from these final-state interactions of the wavefunctions for the particles [16]. The Watson-Migdal method considers the actual emission of the protons and their mutual interactions as separate events, which simplifies the three-body problem of the proton pair and the emitting nucleus [24, 25]. Attractive final-state interactions are assumed to be solely the result of the singlet s-wave interaction, which account for the scattering cross section of two protons [16, 24].

Koonin's formalism of the correlation function for protons can be used to extract information about the spatial and temporal characteristics of the emitting source [20, 16]. The shape of the correlation function shows the strength of the interaction between the nucleons, so pp correlation functions show effects from Pauli blocking, Coulomb, and other final-state interactions between protons. The size and shape of the correlation functions depend upon the size and lifetime of the source which emitted the particles [22]. Figure 1.4 shows the pp correlation function calculated based on a Gaussian source, using Equation 1.3, considering two different source radii (2.5 fm on top, 5 fm on bottom). The correlation function that merely considers the Coulomb contribution has a gradual slope down to zero at moderate q_{Rel}, and a steeper slope at low q_{Rel}. This shape is due solely to the Coulomb repulsion between the protons. The addition of the antisymmetrization consideration for wavefunctions of identical fermions has a correlation function that is normalized to 1 at large q_{Rel} and dips down below 1 for q_{Rel} <50 MeV/c with a more gradual slope but overall larger hole at low q_{Rel}. The addition of antisymmetrization further reduces the correlation function at low q_{Rel}. Inclusion of the nuclear final-state interaction introduces a strong peak in the function near q_{Rel}=20 MeV/c. This peak is due to the attractive s-wave interaction between protons, which is strong enough to increase the yield of correlated protons between 5 and 50 MeV/c. All three contributions are required to recreate the shape of known experimental correlation functions, such as those shown in Figure 1.5 [26]. Also, the smaller source, 2.5 fm, has a much stronger correlation peak [22].

Correlation functions have been used extensively to extract spatial and temporal information about excited emitting sources from nucleon-nucleon interactions [27, 28, 20, 21, 29]. Theoretical

predictions have suggested that the contribution of the asymmetry potential to the behavior of nucleon-nucleon interactions may be large enough that nn, pp, and pn correlation functions in experimental data could be used to constrain the density-dependence of the asymmetry energy [30]. For this work, pp interactions are used to construct correlation functions for this purpose.

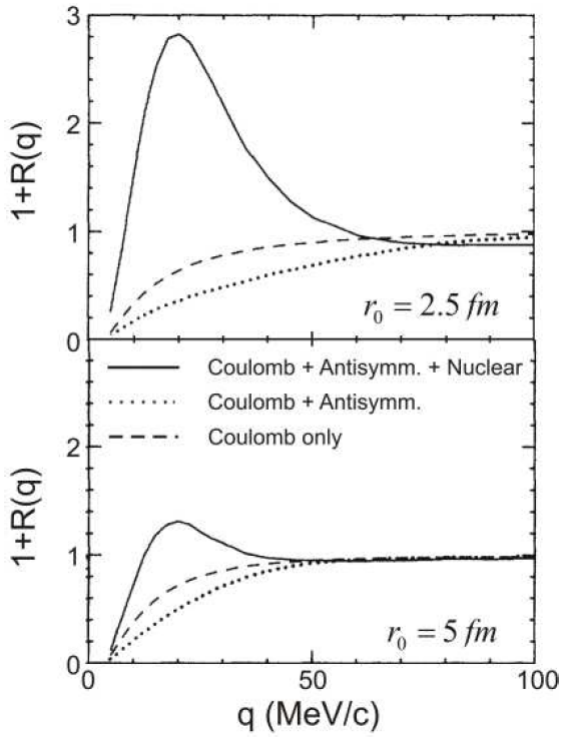

Figure 1.4: Calculated two proton correlation functions for two different r_0, according to Equation 1.3, with a Gaussian source function, S(r) $\propto exp(-r^2/r_0^2)$. Reprinted from [22].

The function C($\mathbf{p}_1$, $\mathbf{p}_2$), from the Koonin-Pratt formalism, can be written for experimental data as [28, 20, 21]

$$1 + R(q_{Rel}) = C(q_{Rel}) = N\frac{Y_c(q_{Rel})}{Y_{uc}(q_{Rel})}, \tag{1.4}$$

and plotted as a function of q_{Rel}. The R(q_{Rel}) term is taken from Equation 1.3. The individual momenta of proton 1 and proton 2 are denoted $\mathbf{p}_1$ and $\mathbf{p}_2$. The normalization coefficient, N, is defined to make C(p_1,p_2)=1 at large values of q_{Rel} (the protons have very little correlation when

they have a large spatial separation or are emitted at very different times). The numerator, $Y_c(q_{Rel})$, is the yield of pairs of protons at each q_{Rel} from the same event, some of which are correlated. The denominator, $Y_{uc}(q_{Rel})$, is the yield of the uncorrelated portion of the ratio. This represents the yield calculated from proton pairs which have no correlation, taken from different events for each q_{Rel} in a technique known as "event mixing" [28, 31, 16].

The shapes of the correlation functions are due to the attractive strong force, Pauli blocking, and Coulomb repulsion. The magnitude of these effects on the shape of the correlation function depends on the size of the source and the timescale of its decay. A value for $C(q_{Rel})$ of greater than one means that correlated pairs of protons are more likely to be emitted at that relative momentum, while a ratio of less than one indicates an anticorrelation for that region in q_{Rel} (e.g. the "Coulomb hole"). The low values of C(q) in Figure 1.4 at low q_{Rel} are due to both the Pauli exclusion principle and Coulomb interactions between protons [16].

The correlation is stronger with a shorter distance (in time and space) between the emissions of the protons. A source that appears larger could simply emit proton pairs with a larger amount of temporal separation [16]. The pp correlation function is affected by all of the interactions of the two protons: Coulomb, nuclear, and the antisymmetry requirement of fermions [16]. The height of the ratio around q=20 MeV/c, where the correlation is greatest, is inversely proportional to source volume, (see Figure 1.4) which is related to the density [22, 16].

1.3.1 Experimental Correlation Functions

Correlation functions have been measured from a wide variety of reaction systems and energies [32, 33, 27, 28]. Larger correlations have been seen in reactions involving larger target nuclei [16]. Figure 1.5 shows correlation functions from nn, pp and np combinations from a reaction of ^{58}Ni + ^{27}Al at 45 MeV/A. The functions are normalized, as shown in equation 1.4, above $q_{Rel} \approx 40$ MeV/c. The nn and np correlation functions (panels a and c, respectively) show increasing correlation with decreasing relative momentum. The pp correlation function (panel b) shows the characteristic "Coulomb hole" expected for two charged particles. The open markers have a denominator (eq. 1.4) constructed by the "event-mixing" technique and the closed markers use the "singles-product".

No appreciable difference is observed, demonstrating that either technique may be utilized for constructing the correlation function, without affecting the basic shape [27]. It is of note that these correlation functions were extracted only from particular detectors that were "equidistant," the full angular range is not represented [27].

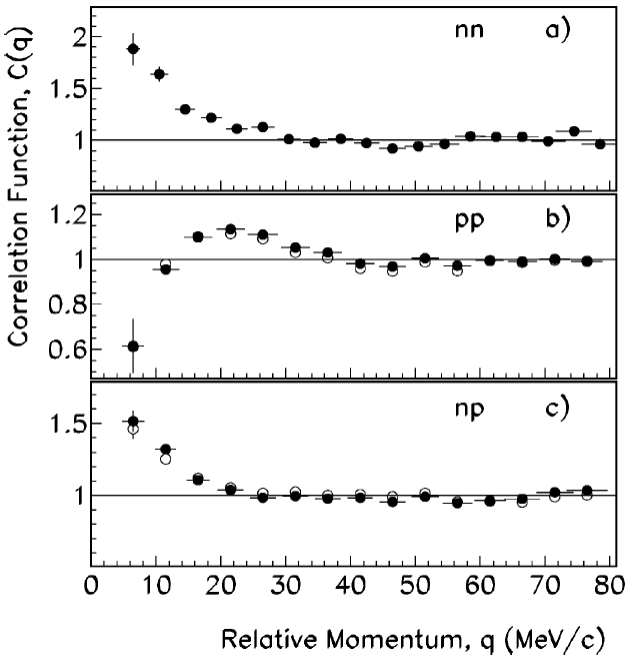

Figure 1.5: Correlation functions from 45 MeV/A ^{58}Ni + ^{27}Al reaction. The open markers have a denominator (Eq. 1.4) constructed by the "event-mixing" technique, the closed markers use the "singles-product". Reprinted from [27].

Correlation functions have also been extracted using mixed pairs of other light charged particles and even intermediate mass fragments [22, 16, 34]. Composite particles can be emitted on a different timescale from the free protons, so they can probe different regions of the reaction [16]. Clusters of nucleons are easier to detect than free nucleons [4]. The interactions of composite fragments are more complicated than the simple interactions depicted for pp correlation functions in Figure 1.4, as shown in Figure 1.6. The two particles are not identical, so two different types of pairings, based on the velocities of the fragments, are shown. The open markers show $v_p > v_\alpha$ and

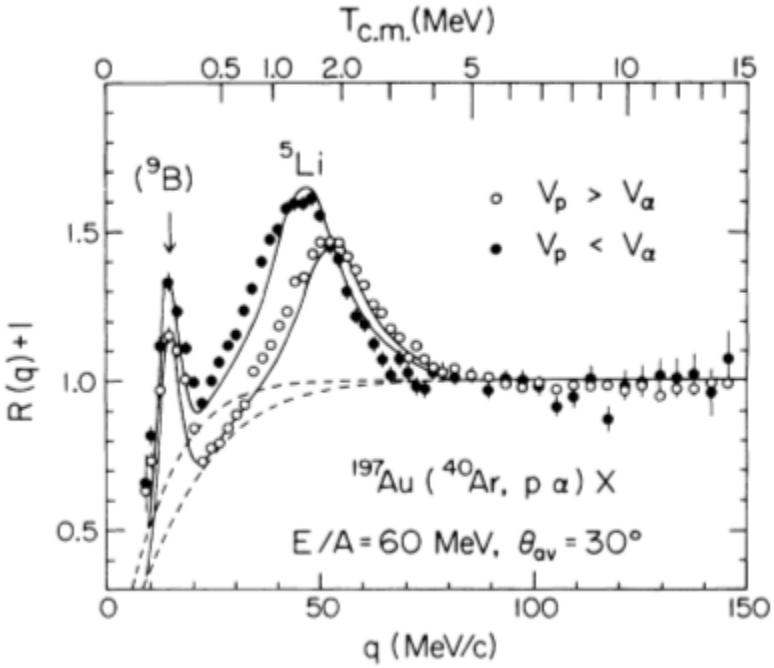

Figure 1.6: Correlation functions calculated for proton-alpha pairs from 60 MeV/A reaction of ^{40}Ar + ^{197}Au. Reprinted from [34].

the closed denote $v_p < v_\alpha$ [22, 34]. Regions of high correlation are observed for unbound ^{5}Li and ^{9}B (sequential decay, resulting in one proton and two αs) resonance states shown in Figure 1.6. These correlation functions are more complicated, but also can give another measurement of the extent of the source function.

1.3.2 Predicted sensitivity of pp correlation functions to the asymmetry energy

The correlation function contains information about the radius of the source [29, 23]. However, the effect of the density convoluted with the relative time of emission needs to be understood. The protons are assumed to not be able to be emitted concurrently in the Koonin-Pratt correlation function formalism [20, 21]. Interactions between any two nucleons [proton-proton (pp), neutron-neutron (nn), proton-neutron (pn)], although of the same general form, differ depending upon the two nucleons involved [16, 30, 27, 28, 25, 29]. Correlation functions, which can help characterize these interactions, are sensitive to the size of the source and the timescale of the particle emission

from the source [30, 27, 28]. Chen *et al.* have shown that the emission timescale of protons, and, therefore, the shape of the correlation function, is sensitive to the nuclear asymmetry energy using results from the isospin-dependent Boltzmann-Uehling-Uhlenbeck (iBUU04) transport model [30].

The shape of correlation functions is affected not only by the size, shape, and decay timescale of the source, but also by the interactions between individual nucleons after emission. It is useful to be able to investigate the effect of the nEoS on the size and shape of the correlation function using models. This interaction, which has been investigated by Chen *et al.* in iBUU, includes the asymmetry energy [30]. In isospin-dependent BUU, the asymmetry energy of the nEoS is included by changing a parameter (γ in figures 1.7 and 1.8) in the momentum dependent interaction. Different parametrizations of the nEoS in iBUU result in different nuclear potential pressures between the nucleons, which influence emission time of different particle types. When the timescale or relative orders of emission are changed for nucleons, the resultant correlation functions change. A larger pressure leads to overall faster emission of particles [4].

The majority of theoretical works extracting pp correlation functions have used transport models such as iBUU [30] or pBUU [28], Brownian One-Body [35], or Boltzmann-Nordheim-Vlasov [22, 36, 37]. Stochastic Mean Field calculations have been used to construct fragment-fragment correlation functions [38]. Relativistic Quantum Molecular Dynamics [39] has been used to reproduce correlation functions from relativistic heavy-ion collisions with some success [40].

Chen *et al.* have reported that the shape of correlation functions from iBUU for the very neutron-rich reaction of ^{52}Ca+^{48}Ca at 80 MeV/A and central impact parameters is affected by the parametrization of the asymmetry energy due to the effect of the asymmetry potential and pressure on the emission times of neutrons and protons [30]. Figure 1.7 shows relative emission times for protons and neutrons using two different parametrizations of the asymmetry energy from iBUU. The nucleons of highest momentum are emitted earliest, on average. In a soft density-dependence parametrization of the asymmetry energy, nucleons are emitted at later times than in a stiff parametrization. This is in agreement with the overall higher asymmetry pressure seen for this

soft interaction. The neutrons (open markers) are emitted before the protons at larger momenta in both the stiff and soft nEoS, but after the protons at lower momenta in the stiff parametrization [30].

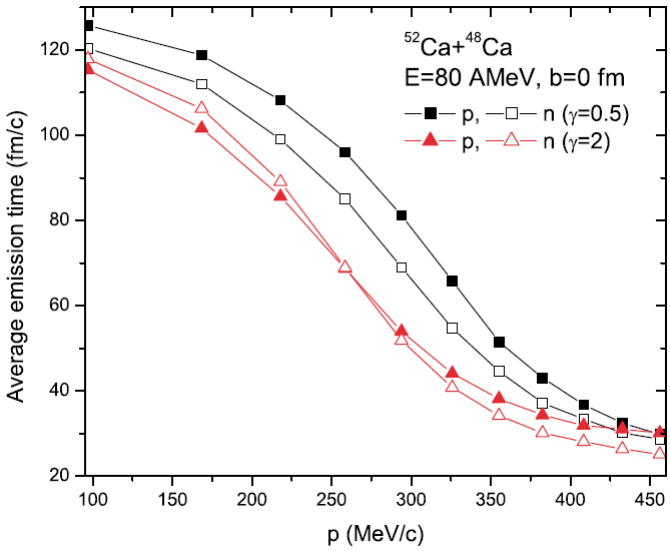

Figure 1.7: Relative emission times for neutrons and protons from different density-dependences of the asymmetry energy. Reprinted from [30]. The black markers are the soft density-dependence, and the red markers are the stiff density-dependence.

Figure 1.8 shows correlation functions calculated for pp, nn, and np pairs using the $\gamma = 0.5$ (soft) and $\gamma = 2$ (stiff) parametrizations of the asymmetry energy in iBUU discussed earlier [30]. The overall correlation is greater in the stiff density dependence. The largest differences in the ratios extracted using the two parametrizations occurs in the larger P_{Tot} case. These nucleons were likely emitted earlier in the simulation, before expansion and cooling of the source. The largest differences in the ratios extracted using the two parametrizations occurs in the larger $\mathbf{P}_{Tot}=\mathbf{p}_1+\mathbf{p}_2$ case, where emitted nucleons have more interactions. The nn correlation function shows increased correlation with decreased momentum, due to the lack of Coulomb interaction.

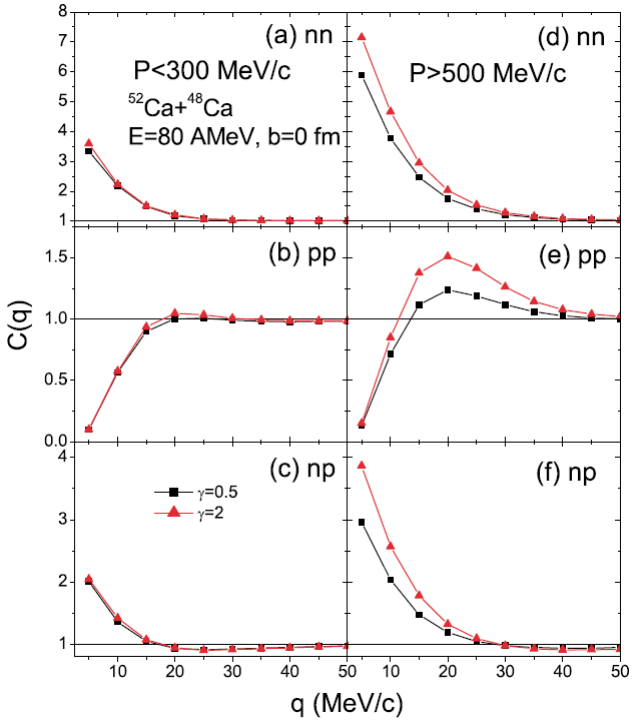

Figure 1.8: Correlation functions calculated for pp, nn, and np pairs from 80 MeV/A reactions of ^{52}Ca + ^{48}Ca, using $\gamma = 0.5$ (soft) and $\gamma = 2$ (stiff) parametrizations of the asymmetry energy in iBUU. Reprinted from [30].

1.3.3 Previous Experimental Work

Experimental correlation functions are often constructed using all measured energies and angles [16]. Events used to create the correlation function can be cut to observe only events with similar amounts of excitation energy and therefore violence of collision [27]. These similar events can be differentiated based upon $\mathbf{P}_{Tot}$ and even angular orientation in the lab [28, 16].

The shape and size of the correlation function depends heavily on the shape of the source function [S(r)]. Work has been done to extract the actual source function (from Equation 1.3) from the correlation function [29, 41]. The source cannot necessarily be assumed to be Gaussian [29]. The timescales of the emission of the protons are also very important. The source function is symmetric for like particles.

The most recent experiment to probe the iBUU-predicted sensitivity of the correlation functions

to the asymmetry energy was run at Michigan State University by Kilburn [42]. The experiment used symmetric systems of ^{40}Ca and ^{48}Ca at 80 MeV/nucleon and pBUU as the transport model comparison. The resultant correlation functions are shown in figure 1.9. The correlation function is plotted as a function of relative momentum of the proton pair for both of the calcium systems at midrapidity, $-0.05 < y_{cms} < 0.05$. These correlation functions were constructed using the event-mixing technique. There is a characteristic s-wave interaction at 20 MeV/c in momentum space. The ^{40}Ca system has a higher and slightly more broad peak, indicating higher levels of correlation for the smaller projectile, a larger source size for the larger, more neutron-rich ^{48}Ca system.

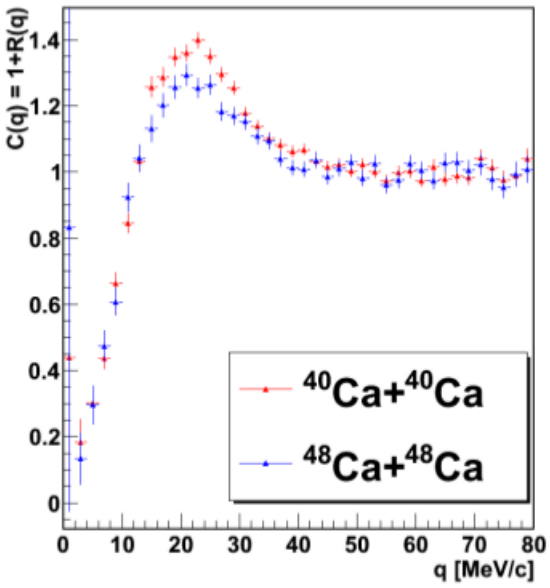

Figure 1.9: Experimental correlation functions extracted from protons resulting from symmetric collisions of ^{40}Ca+^{40}Ca and ^{48}Ca+^{48}Ca at 80 MeV/nucleon. Reprinted from [42]. The ^{40}Ca system has a higher peak, indicating higher levels of correlation for the smaller projectile.

When this data is cut on bins (low: 500-640 MeV/c, high: 740-900 MeV/c) of total momentum of the proton pairs (p_{pair}), as well as laboratory angles of 18-26°, 26-33°, and 33-58°, as in reference [28], differences emerge in the correlation functions. Figure 1.10 shows the resulting correlation

functions. These correlation functions are compared to three different techniques (Gaussian source, with and without time component, and imaging [23, 41]) of determining the size of the source, via the source function (Equation 1.3). The largest correlation of the proton pairs occurs when the protons have the largest p_{pair} or the most backward angle in the laboratory [28].

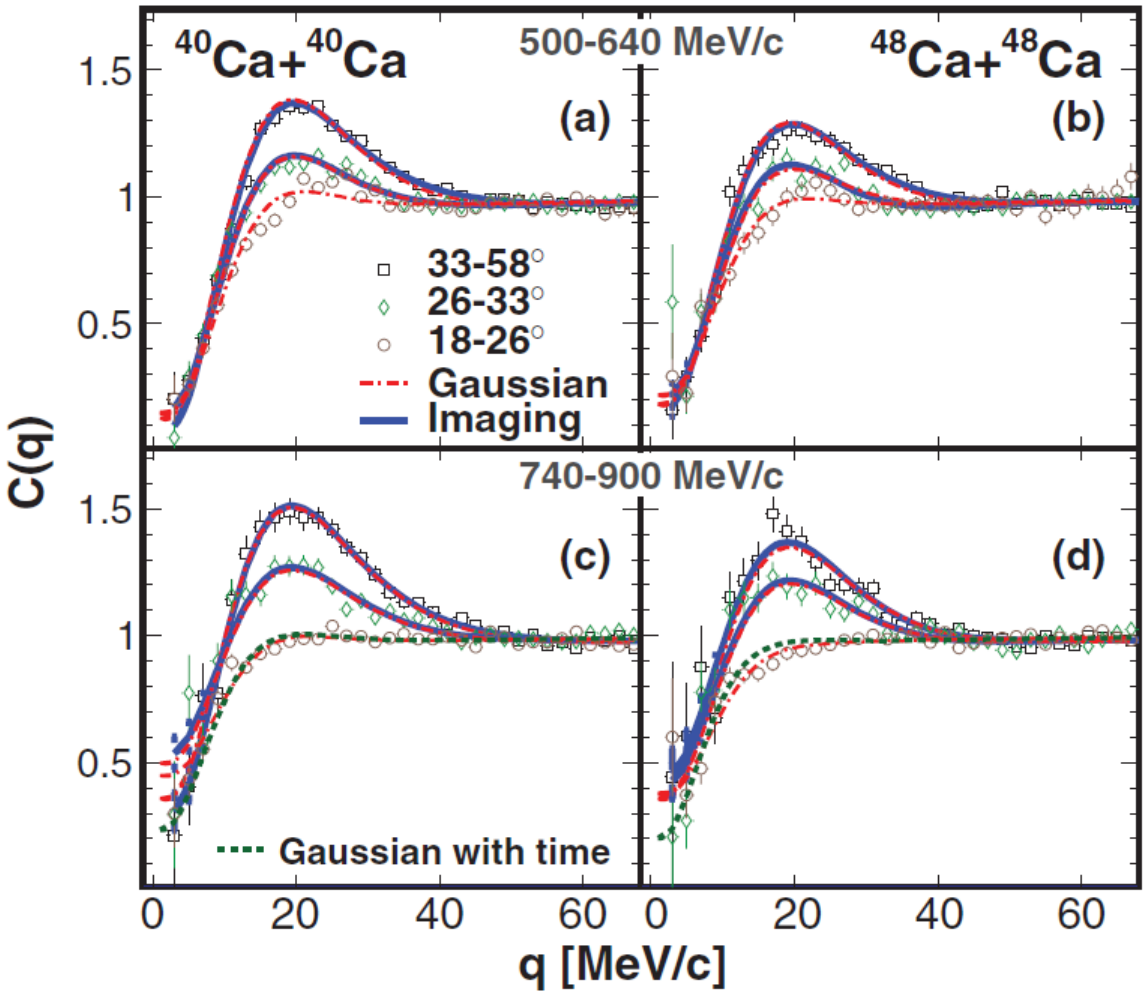

Figure 1.10: Experimental pp correlation functions cut on total momentum of the proton pair and on protons detected at different laboratory angles. Reprinted from [28]. The points are experimental data, the lines are fits for to extract source size.

The sources resulting from the ^{48}Ca+^{48}Ca collisions were larger than from the symmetric ^{40}Ca

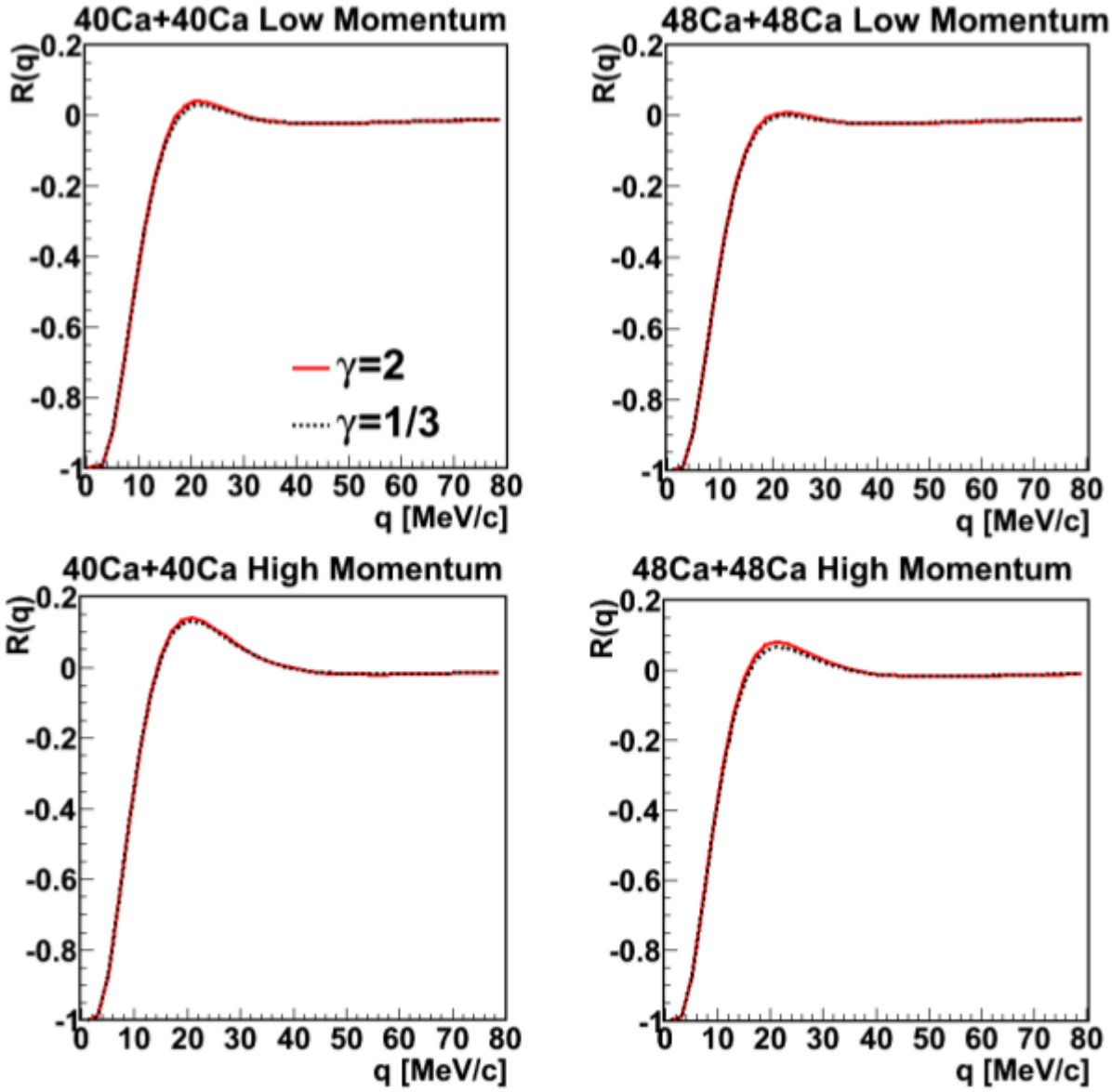

Figure 1.11: Correlation functions extracted pBUU simulations of ^{40}Ca+^{40}Ca and ^{48}Ca+^{48}Ca at 80 MeV/nucleon. Reprinted from [42].

system, so the more neutron-rich system had a weaker correlation function. However, the projectiles were different sizes to start with, so a dependence on Δ is masked by that fact.

A study using pBUU was also undertaken along with this experiment in the style of [11]. This provided the theoretical motivation for cutting on the total momentum of the proton pair. Figure 1.11 shows the result of the study by Kilburn [42]. Regardless of cuts on the momentum of the

proton pair or the system, no large difference is seen between γ=2 and γ=$\frac{1}{3}$. The systems were not compared to one other directly in that experimental or transport model analysis. It may be possible to see a difference in the ordering of the strength of the correlation functions based upon the asymmetry energy if these comparisons are made while keeping the system size similar. This is the aim of the work presented in this dissertation.

2 EXPERIMENTAL DETAILS

This section describes all of the experimental details, starting with section 2.1, which outlines the reactions. The detectors used are described in section 2.2. The configuration of the Forward Array Using Silicon Technology (FAUST) is discussed in section 2.2.1, with the individual telescopes discussed in section 2.2.2 and the silicon upgrade discussed in section 2.2.3. The electronics used to process the signals from each of the detectors are discussed in section 2.3.

2.1 Beams and Targets

This experiment used ^{40}Ar and ^{40}Ca at 40 MeV/nucleon impinged upon ^{58}Fe and ^{58}Ni targets, respectively. A 0.015" aluminum degrader upstream of the target provided 30 MeV/nucleon ^{40}Ar beam. This beam was run on ^{58}Fe and ^{70}Zn targets. This resulted in the systems listed in table 2.1.

The calibration beams, used for checking the energy calibrations of both Si and CsI(Tl) detectors and checking the position information from the Si detectors, were 15 MeV/nucleon α and 10 MeV/nucleon p-α, both elastically scattered off of the thick ^{197}Au target. The Au target was sometimes covered by a thick Al collimator with a hole of 1 mm in diameter, to approximate a point source. This method was used for acquisition of both beam and source data with the mask (described in section 2.4). Because the data was collected in three separate runs, these calibration beams were run at the end of both beamtimes in fall 2014 and in spring 2015. All of the aforementioned beams were accelerated using the K500 cyclotron at the Cyclotron Institute at Texas A&M University.

These systems keep either the total A or total Z of the system constant, while changing the isospin asymmetry ($\Delta = \frac{N-Z}{A}$) as shown in table 2.2. Notice that the Δ of the Ca+Ni system is significantly less neutron-rich than the other systems. This was done to investigate the effects of the asymmetry of the system and system size (and subsequent size and lifetime of an emitting source) on the correlation function.

Beam Material	Energy (MeV/nucleon)	Target Material	Thickness	Percent Purity	Number of Proton Pairs
^{40}Ca	40	^{58}Ni	505 μg/cm^2	99.89	935925
^{40}Ar	40	^{58}Fe	1.8 mg/cm^2	98	95232
^{40}Ar	30	^{58}Fe	1.8 mg/cm^2	98	78427
^{40}Ar	30	^{70}Zn	985 μg/cm^2	95	996499
$^{4}\alpha$	15	^{197}Au	12 mg/cm^2	100	
$^{4}\alpha$-p	10	^{197}Au	12 mg/cm^2	100	

Table 2.1: Reaction systems and targets, including the two calibration beams.

	Beam			Target			System		
System	Z	A	Δ	Z	A	Δ	Z	A	Δ
^{40}Ar+^{58}Fe	18	40	0.100	26	58	0.103	44	98	0.102
^{40}Ca+^{58}Ni	20	40	0.000	28	58	0.034	48	98	0.020
^{40}Ar+^{70}Zn	18	40	0.100	30	70	0.143	48	110	0.127

Table 2.2: System Z, A, and isospin composition.

2.2 Forward Array Using Silicon Technology (FAUST)

The Forward Array Using Silicon Technology (FAUST) was designed to measure fragments from the excited projectile-like fragment (PLF*) from intermediate energy heavy ion collisions in the angular range of 1.6-45.5° [**?**]. It consists of sixty-eight Si/CsI(Tl) ΔE-E telescopes, an example of which is pictured in figure 2.1. The silicons are nominally 300 μm thick.

2.2.1 FAUST Detector Configuration

The 68 detector telescopes (Det 0-67) are arranged in five concentric square "rings" with the center of the front square surface of each detector within a single ring equidistant from the target position. These distances are indicated in table 2.3 their relative spatial orientation can be seen in the CAD drawing in figure 2.2. The faces of the telescopes are arrayed to cover forward of the target position, as depicted in figure 2.3. This alignment greatly reduces the "dead space" in the array.

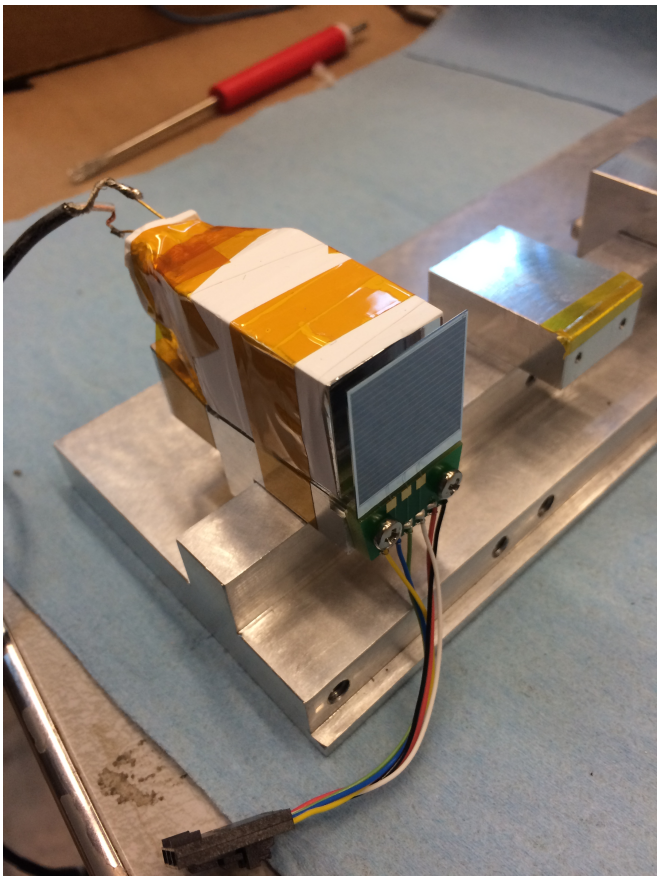

Figure 2.1: Picture of a single FAUST telescope. The DADL Si is mounted to the front, with the large CsI(Tl) crystal, light guide, and photodiode for readout following.

The detectors in the closest ring to the target position (Ring E) cover the largest angular range. The range subtended by the detectors decreases as the rings increase in distance from the target position. The angular coverage of each ring of the array is given in table 2.3. The arrangement of the detectors in each ring has D_4 symmetry. The detector positions which cover the same theta and a rotaionally symmetric phi are shown as the same color in figure 2.3. The angles subtended by each different type of detector are indicated by Table 2.3.

The telescopes are packed closely together in FAUST. The θ_{lab} and ϕ_{lab} of the FAUST, along with the fractional coverage of the array are shown in figure 2.4. There is space for protective aluminized mylar foils between the rings to protect the silicon detectors from electrons knocked free of the target when bombarded by the beam. Each mylar sheet has an open square cut around

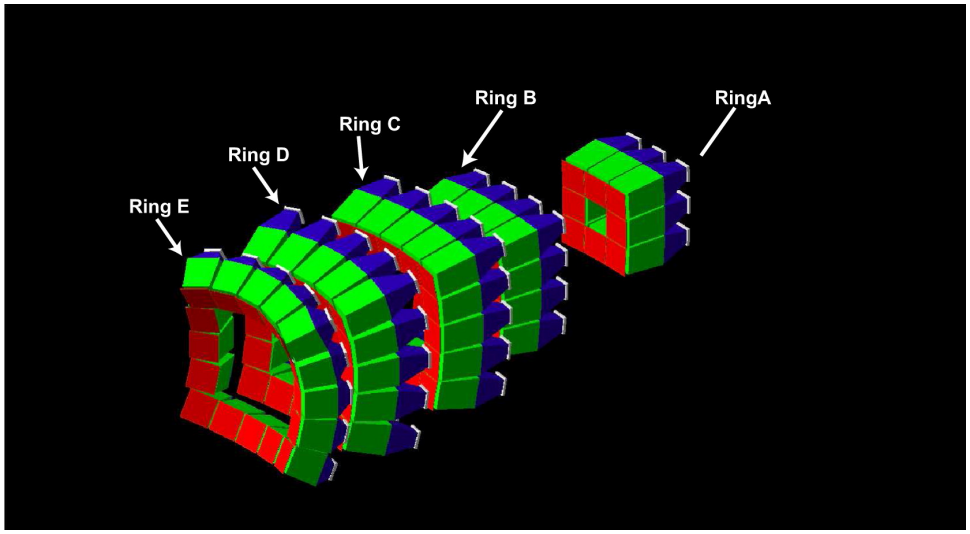

Figure 2.2: GEANT4 rendering of FAUST. Silicon DADL detectors are shown in red, CsI(Tl) crystals shown in green, light guides in blue, photodiodes for light collection in white.

Ring	Distance from Target (cm)	Detector Position	Detector Numbers	$\theta_{low}(^\circ)$	$\theta_{center}(^\circ)$	$\theta_{high}(^\circ)$	$\phi_{center}(^\circ)$
A	40.0	0	1, 3, 5, 7	1.6	3.1	4.8	0
		1	0, 2, 4, 6	2.3	4.3	6.4	45
B	27.9	2	9, 10, 12, 13, 15, 16, 18, 19	4.5	7.0	9.7	18.4
		3	8, 11, 14, 17	6.4	9.4	12.3	45
C	21.8	4	22, 26, 30, 34	8.8	11.5	14.4	0
		5	21, 23, 25, 27, 29, 31, 33, 35	9.3	12.8	16.4	26.3
		6	20, 24, 28, 32	12.3	16.0	19.6	45
D	14.3	7	38, 42, 46, 50	14.3	18.3	22.7	0
		8	37, 39, 41, 43, 45, 47, 49, 51	15.0	20.2	25.6	26
		9	36, 40, 44, 48	19.4	25.1	30.1	45
E	10.1	10	54, 58, 62, 66	22.6	28.4	34.5	0
		11	53, 55, 57, 59, 61, 63, 65, 67	23.3	30.8	38.5	25.2
		12	52, 56, 60, 64	29.3	37.4	45.5	45

Table 2.3: Defining Rings A-E of FAUST, moving from the most central (furthest from the target) to the more peripheral rings (closest to the target position). The different symmetric detector positions are depicted in figure 2.3.

the path of the beam, so that each charged fragment only passed through one layer of mylar. The first layer was placed in front of Ring E, to shield both Rings E and D – this layer was 0.833mg/cm^2.

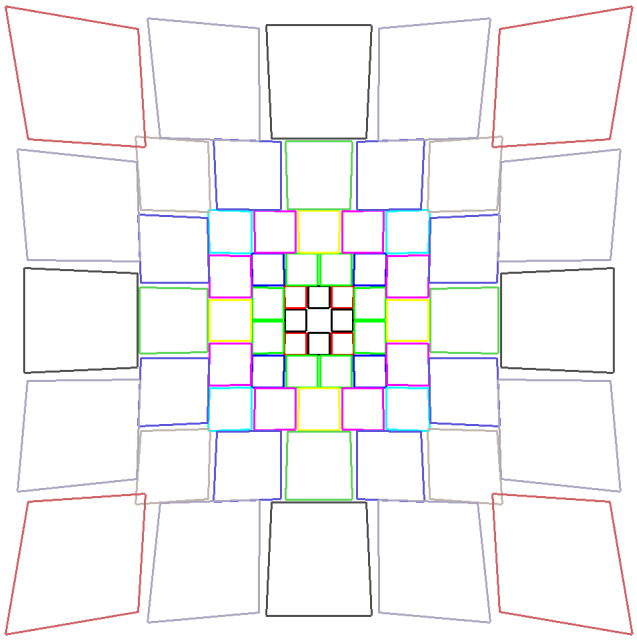

Figure 2.3: A view of the FAUST detectors as seen from the target position. Each of the rings of FAUST are made of the same size detectors, but as the rings move further back from the target position, the detectors subtend a smaller angle in the laboratory frame. The different colors indicate detectors which cover different ranges in θ, which are rotationally symmetric.

The second layer was placed in front of Ring C, to shield both Rings B and C, was 2.535 mg/cm^2. The last layer, in front of only Ring A, was at the greatest forward angle, so this mylar sheet was the thickest; it was 4.778 mg/cm^2.

Within each ring of the FAUST, there are several different lab angles at which the detectors are set, in order to have the square detector surfaces within a single ring equidistant from the target. Altogether, there are thirteen effectively different detector positions, which each are covered by a different effective thickness of mylar. The effective thickness of the mylar varies across the face of the detector with a 1/cos dependence (see table 2.3 for angular ranges of detectors). While one could Monte Carlo sample the energy loss across the entire face of the detector and take the average energy loss, there is a 1% error at worst using the effective mylar thickness only at the center position of each detector. Due to the fact that these sheets are very thin, this mylar essentially only affects electrons from the target bombardment during the experiment. Due to the angular position

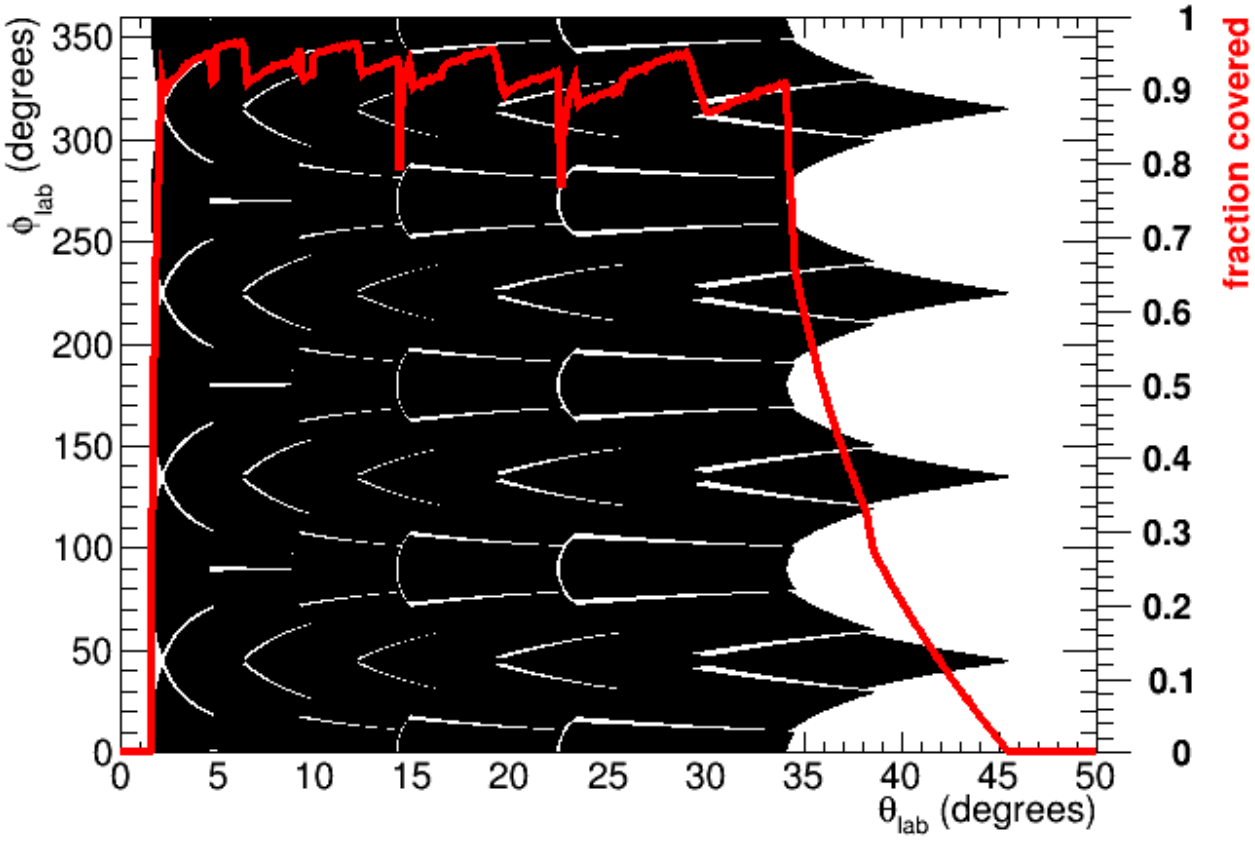

Figure 2.4: Detector coverage of the FAUST, shown in θ_{lab} vs ϕ_{lab}. The red line indicates the fraction covered by the FAUST.

of the detector, however, when a ^{228}Th source is set at the target position for the purpose of energy calibrating the silicon detectors, the effective thickness of mylar through which the α particles are degraded changes, depending upon the angle (θ) of each detector. For the calibration beams, the energy loss in the target was about 2% in the target, and about 1% in the mylar delta-ray shields.

2.2.2 FAUST Telescopes

Each of the 68 telescopes in FAUST consists of an edge-mounted 2x2 cm-faced 300 μm-thick Si detector backed by a thallium-doped cesium iodide scintillating crystal. The CsI is of differing length depending upon the ring (CsI in rings A-D are 3 cm, CsI in ring E are 2.26 cm [43]), optically coupled to a light guide, and read out by a photodiode. A photograph of a representative

telescope is shown in figure 2.1.

2.2.3 Dual-Axis Duo-Lateral Detectors

The FAUST system had good spatial resolution, but increased angular resolution allows for precision correlation functions. Rather than increase the number of detectors, the decision was made to use detectors with position-sensitivity in order to increase the position resolution of the array. Many popular models of position-determining silicon detectors use individual strips of silicon within the wafer to create "pixels" to determine the position of ionizing fragments in "x" and "y". Rather than reading many 200 μm individual strips of silicon, which would drastically increase the amount of dead space on the detector surface and the number of channels needed for electronics, a new type of silicon detector was used, previously developed by S. Soisson, then at Texas A&M University, in concert with Micron Semiconductor Ltd. [44]. A schematic of the detector design is shown in figure 2.5.

The incident charge from ionizing radiation on the biased crystalline diode detector results in the production of both positive ions (hereafter referred to as "holes") and electrons in the silicon lattice. The front surface of the detector and the front guard ring (shown in Figure 2.5) is reverse-biased to -40 V, while the back of the detector is grounded. This reverse-bias collects holes to the front and electons to the back of the detector. The surfaces of the detector are uniformly resistive, so the currents split across the surface.

Two signals are collected from the front (top and bottom, in detector coordinate space) and two are collected from the back (right and left). The front surface of the detector tells the position of the incident radiation in the local Y axis, and the back of the detector tells the position in the local X coordinate. The local x and y are calculated in the following way, where "Q" is the raw charge signal from the detector:

$$X_{local} = \frac{Q_{Left} - Q_{Right}}{Q_{Left} + Q_{Right}} \qquad (2.1) \text{ and} \qquad Y_{local} = \frac{Q_{Top} - Q_{Bottom}}{Q_{Top} + Q_{Bottom}}. \qquad (2.2)$$

Figure 2.6 is a photograph of the front (target-facing) surface of a DADL silicon detector. Conductive stripes of aluminum punctuate the resistive layer at regular intervals across the surface to facilitate the flow of charge to the sides of the face where the charge is collected. These equipoten-

Table 2.4: Thickness of Si detectors according to Micron Semiconductor. Separated by ring.

Detector	Thickness (μm)
0	316
1	311
2	324
3	311
4	324
5	311
6	310
7	316

Detector	Thickness (μm)
8	314
9	324
10	325
11	320
12	324
13	324
14	324
15	317
16	324
17	324
18	310
19	310

Detector	Thickness (μm)
20	317
21	316
22	321
23	324
24	324
25	314
26	324
27	320
28	314
29	320
30	317
31	315
32	322
33	322
34	316
35	316

Detector	Thickness (μm)
36	314
37	315
38	325
39	314
40	314
41	321
42	317
43	321
44	325
45	310
46	311
47	324
48	322
49	314
50	314
51	314

Detector	Thickness (μm)
52	316
53	317
54	311
55	322
56	320
57	316
58	322
59	322
60	317
61	314
62	314
63	317
64	320
65	324
66	314
67	316

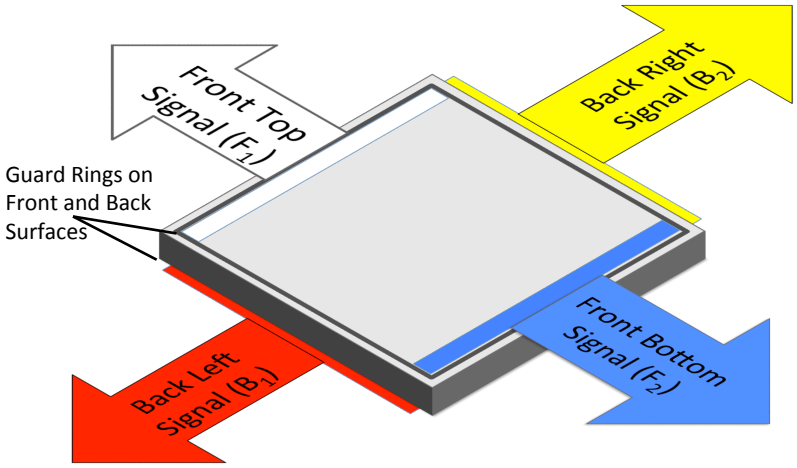

Figure 2.5: Schematic depiction of DADL detector. The signals from the front (back) of the detector (relative to the target position) are indicated by red (green) arrows, and represent the holes (electrons) collected on the front (back) surface. The front and back are equipotential across the surface, due to both ends of the surface being biased or held at ground.

tial lines run horizontally across the front surface because the charge splits to local up and down on this side. On the back surface of the detector, these lines run vertically because the charge splits local right and left on this side. The attachments for the front two signals and front guard ring are the three silver squares, which trace to the blue, green, and white wires. The yellow, red, and black wires attach through the trapezoidal green PC board to the back right, left, and back guard ring. The two holes in the PC board are used to screw the silicon to the front of the aluminum FAUST telescope mount (as shown in figure 2.1).

2.3 Signal Processing

The mounting structure of each ring of FAUST is shown in figure 2.7. The circular aluminum piece fits into the FAUST cradle, which is then aligned in the FAUST chamber in place in the beamline using a transit. Ring A consists of eight detector telescopes, Ring B, twelve, and Rings C-E consist of sixteen telescopes each. These telescopes are arranged in a square on a FAUST ring via mounting structure not visible in this picture. The wires that attach directly to the PC board on the detector were stiff and there was not much room inside the FAUST cradle, so they needed

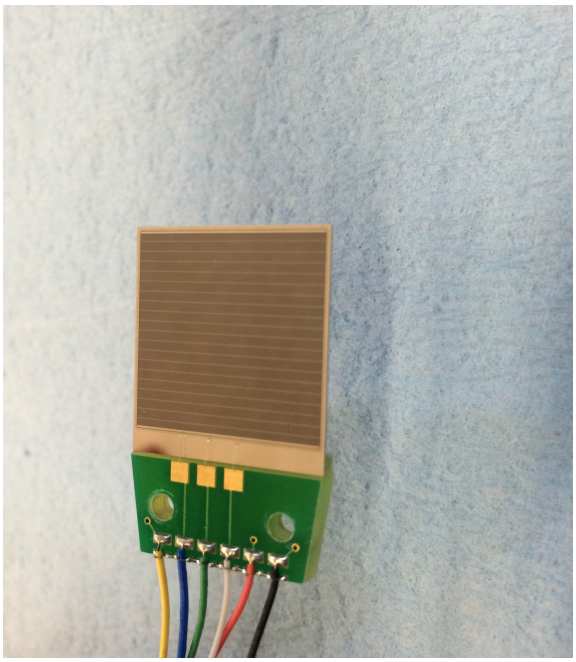

Figure 2.6: Representative DADL silicon detector. As indicated by the horizontal stripes, the charge is split in the vertical dimension on the front of the detector. Signalling across the bottom is as shown in Table 2.5

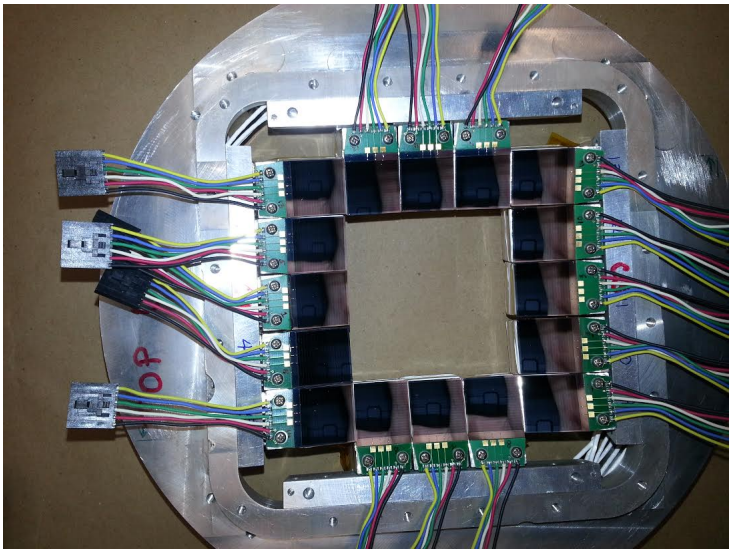

Figure 2.7: Ring C DADL silicon detectors mounted on the ring structure of FAUST, before the ring is added to the FAUST cradle in figure 2.9.

to be contained and then directed out of the cradle. The wires attached to the PC board made a 90 degree turn, so in order to relieve the tension, a strain relief bar was made to sandwich these wires between layers of vacuum-safe cushioning. This set up for the 8 Ring A detectors is shown in figure 2.8.

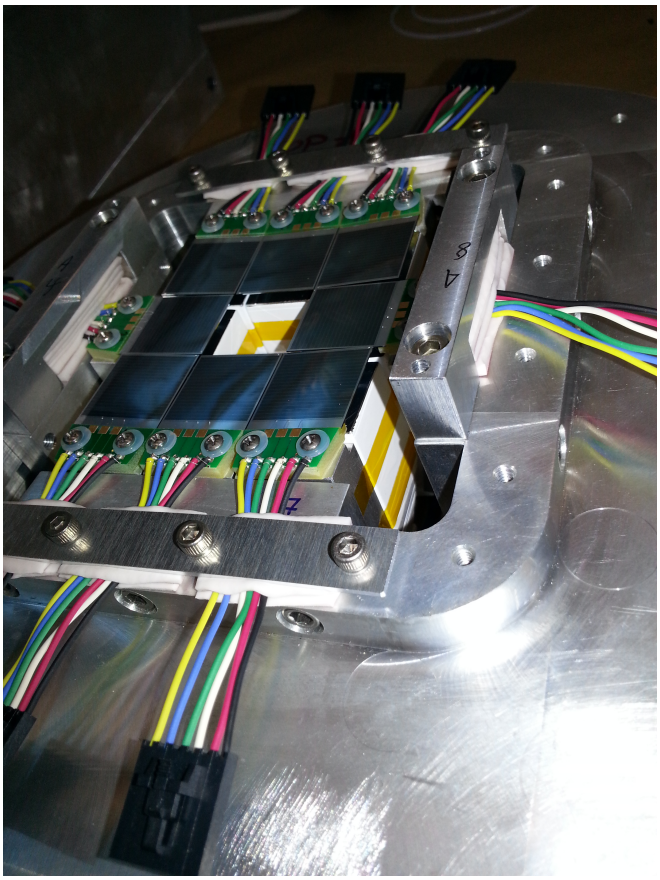

Figure 2.8: Ring A DADL-CsI telescopes and strain relief structure. Buckles at the end of DADL-attached cables fit into buckles attached to low-capacitance cables.

After the strain relief bars were fixed in place, the wires that attach directly to the DADL silicons were secured with kapton tape and buckled to low-capacitance cables to pass through the holes in the cradle visible in figure 2.9. These cables connected to the adapter boards, the drawings for which are shown in appendix A. These PC boards combine the individual signals and Guard Rings from four DADL detectors into a single 32-pin header cable that attached to a

feedthrough in the FAUST chamber wall. These cables were made with very low-capacitance (9.9 pF/ft) 3601/34 ribbon cable manufactured by 3M. They were surrounded by a hollow grounding braid with a grounding strap inside to allow for connections to reduce noise before the signals go to the preamplifiers outside of the chamber.

Figure 2.9: Fully cabled FAUST. The green board in the bottom left is an adapter board, which contains traces to combine the raw signals from four DADL detectors into a 34-pin header to go through feedthroughs in the FAUST chamber faceplate.

In a previous configuration, the preamplifier boards attached directly to the wall of the FAUST chamber. Due to the drastic increase in the number of signals, this configuration would not allow preamplification of a sufficient number of signals for this experiment. The "tower boxes" were designed in order to hold all 340 preamplifiers (CsI and Si) for the experiment and to supply bias

Wire Color	Face	Purpose	Bias
Yellow	Back (right)	Signal	Ground
Blue	Front (Bottom)	Signal	-40V
Green	Front	Guard Ring	-36.4V
White	Front (Top)	Signal	-40V
Red	Back (left)	Signal	Ground
Black	Back	Guard Ring	Ground

Table 2.5: Local wiring and bias scheme for DADL detectors, all directions from point of view of looking straight at the front face of the detector.

(and ground) to all of the FAUST detectors. Details of the wiring can be found in appendix A. The basic signal processing scheme for the DADL detectors up to the chamber wall and then on through the preamplifiers and ASICs is in figure 2.10. Each of the arrows indicates the use of cables. The cables on the inside of the FAUST chamber were low capacitance, to maximize resolution. All of the cables used outside of the chamber were coaxial to reduce noise.

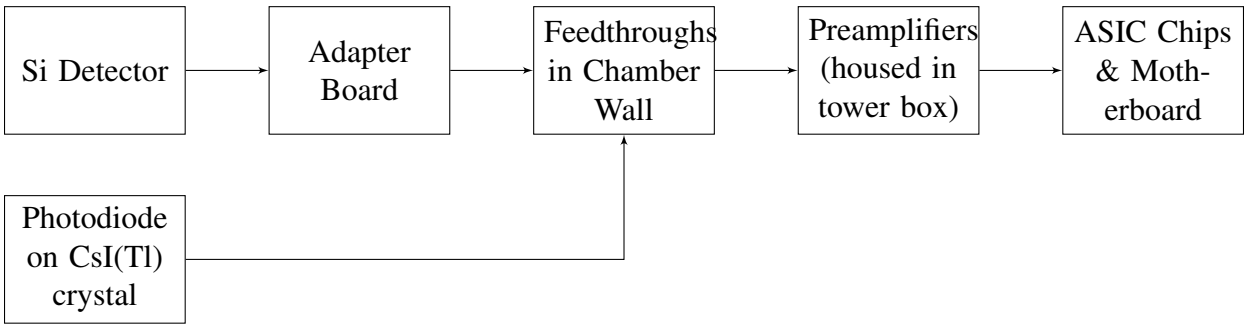

Figure 2.10: Raw signal processing for the FAUST experiment. Cables are indicated by arrows.

Bias was applied to both photodiodes and DADL detectors using the Wiener Mpod bias supply module via the motherboards holding the ~40 mV/MeV ZeptoSystem preamplifiers inside of the tower boxes. The bias was applied to the photodiodes via the method described by the diagram in figure 2.11. These detectors were biased ring-by-ring through the preamplifier motherboard to 9 V.

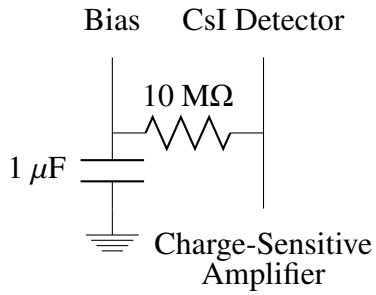

Figure 2.11: Biasing diagram for the photodiodes that read out CsI signals.

DADL detectors were individually biased to -40 V. The connection to each of the preamplifier motherboards, through which the DADL detectors were biased, was made through the PC board which is the back plane of the tower boxes. There was one box for each of the rings of FAUST. Each tower box had the capacity to hold five preamplifier motherboards. Sixteen preamplifiers fit on a preamplifier motherboard. So the sixteen detector rings (C, D, and E) had full tower boxes, with two full preamplifier motherboards used for the front signals, two motherboards full of preamplifiers for the back signals, and one preamplifier motherboard for biasing and processing the signals from all of the cesium iodide detectors. Rings A and B, which contain eight and twelve telescopes, respectively, used only partial tower box capacity. The full biasing circuit for one surface of a DADL detector is shown in figure 2.12.

The Application-Specific Integrated Circuit for HINP (Heavy Ion Nuclear Physics), developed by the Sobotka group at Washington University in St. Louis [45] were used to amplify the signals from the preamplifiers and send the peak voltage to the XLM-XXV (JTEC Universal Logic Module) for digitization. The signal-splitting depending upon position of the particle on the surface DADL detector meant that the amplitude of interesting signals from the silicon detectors would be much smaller than had previously been detected in the original FAUST electronics. Also, it was desirable to get as much of the light charged particle distribution as possible in this experiment. Much higher-gain preamplifying circuits were desirable for this upgrade. Preamplifiers of 110 mV/MeV, designed and manufactured by RisCorp Inc. were used to handle the Si signals, as depicted in figure 2.10 [46].

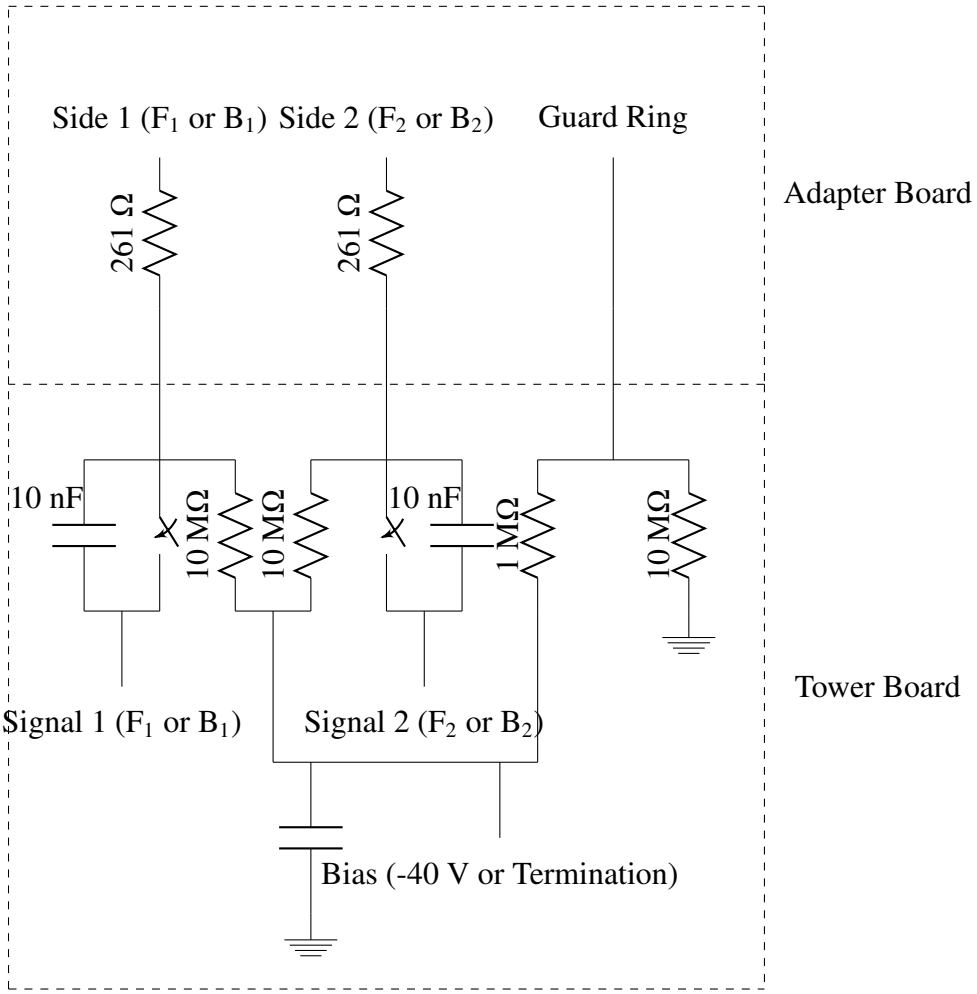

Figure 2.12: Circuit diagram for the biasing scheme for one surface of a single DADL detector. For the front face, the bias is at -40 V. For the back surface, the bias goes to ground via a 50 Ω terminator. Dotted lines correspond to where the components are located, straight lines refer to cables or traces on PC boards.

Because these preamplifiers are such large gain, keeping the noise to a minimum became very important for this experiment. A copper wire mesh around the preamplifier tower boxes during the experiment acted as a Faraday cage and cut down the ambient noise considerably (see photograph in figure 2.13).

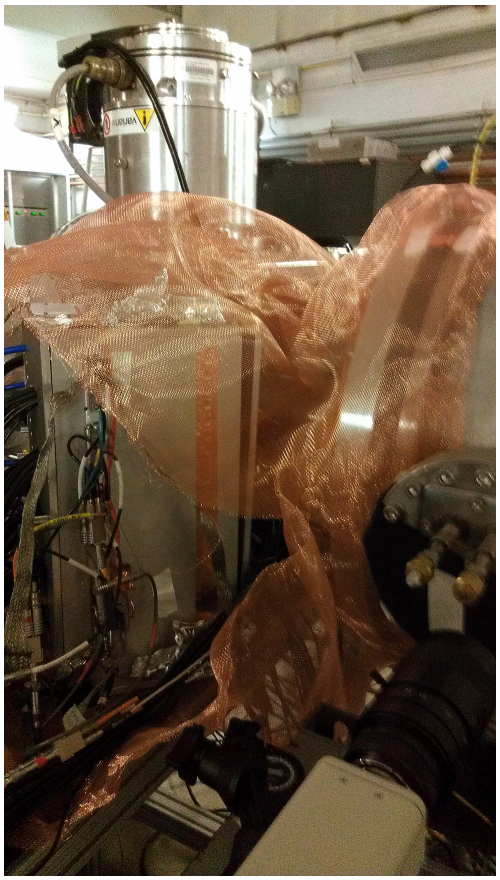

Figure 2.13: Copper mesh enclosing "Tower Boxes" which housed the preamplifiers during this experiment. During running configuration, the copper mesh completely enclosed the preamplifiers and the wires from the chamber to the tower boxes, forming an effective Faraday cage.

During beam, the trigger chosen in the ASIC interface was the cesium iodide detectors, rather than the silicons, which were noisier due to the large preamplifier gain. The trigger logic was set up as shown in figure 2.14. The preamplified signals came from the Tower Boxes as shown in figure 2.10 into the ASIC chips in the box at the top left of the electronics diagram. These signals were

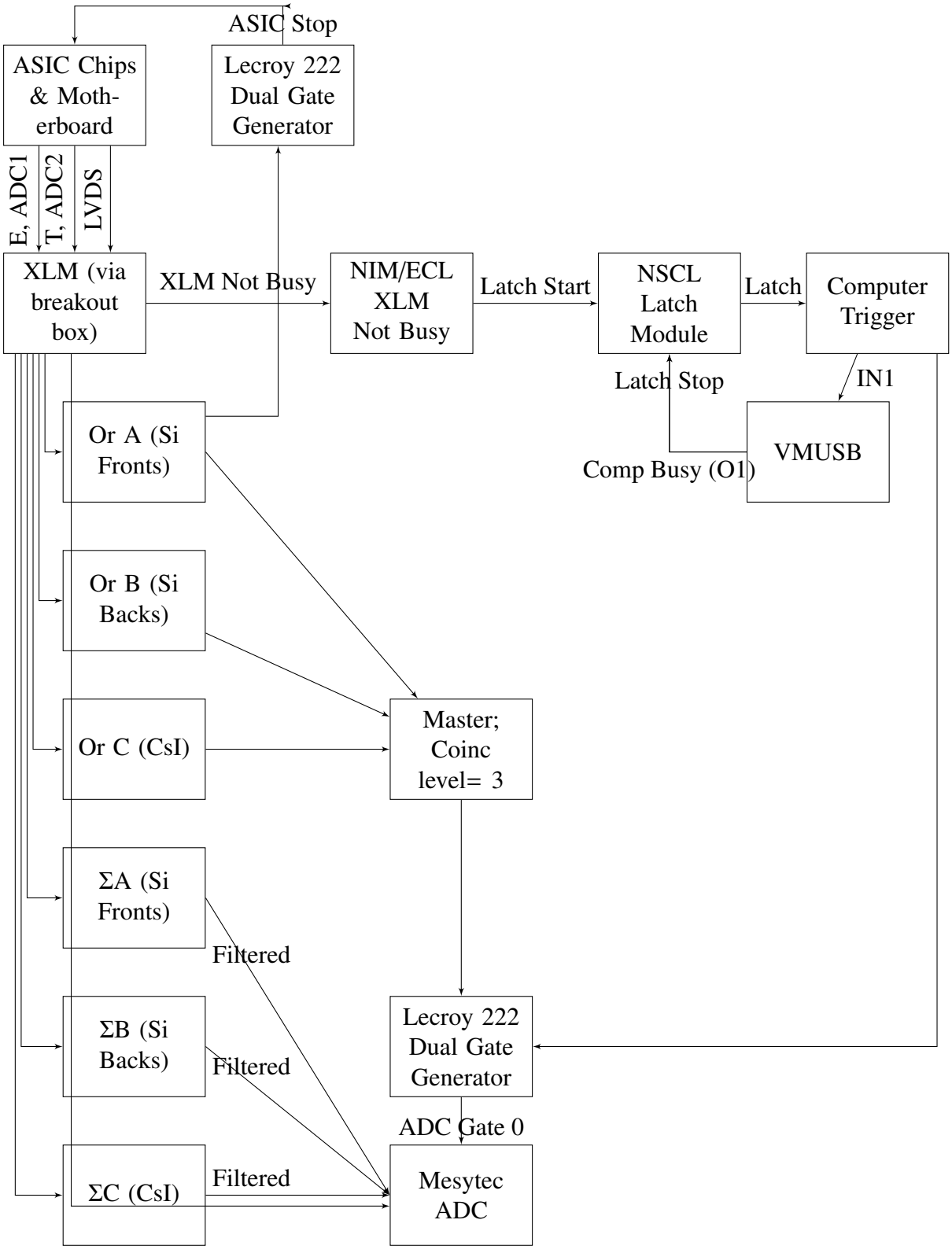

Figure 2.14: Electronics diagram of ASIC trigger logic for the FAUST experiment.

sent to the XLM. From the XLM, all of the signals were sent to the Mesytec ADC. A coincidence of at least one each of Si front (A), Si back (B) and CsI (C) with the computer trigger (see "Master" in figure 2.14) were required to create the ADC gate with the Lecroy 222 Dual Gate Generator. The computer trigger was generated starting with an XLM Not Busy signal and a signal from any cesium iodide. This acted as the Latch Start, and sent the Latch to the Computer Trigger. The Latch Stop came from the Computer Busy signal from the Versa Module Universal Serial Bus (VMUSB). A DC signal proportional to the number of Si Front channels fired was sent to the Mesytec ADC. Other such signals for the Si-Backs and the CsI were also sent to the ADC.

2.4 Position Determination

This was the commissioning experiment for the position-sensitive silicons in the FAUST. Once the DADL detectors are mounted in the FAUST cradle and aligned in the beam, it was important to know that the position-sensitivity of the signals was working properly and all of the local-to-global transposing of the position signals was correct. In order to do this and allow finer calibration of the detector-to-detector relative position in the future, to maximize the benefit of the improved angular resolution of the silicon detectors, some method had to be devised. The mylar foils present in front of the silicon detectors added a degree of difficulty to this endeavor, as the silicon detectors are not optically visible from the target position once FAUST is assembled and in place in the beamline. It became clear that a method needed to be created that would allow specific shapes to be projected via source alphas or elastically scattered calibration beams from the target position uniquely across all detectors of the FAUST. The complexity of this problem is compounded by the unique angling of the detectors at the different positions in FAUST, listed in table 2.3. Also, the ring A detectors are 40 cm away from the target position, so the pattern needed to be very small on the frontplate of FAUST to be visible on a 2x2 cm detector that distance away.

A slotted mask was designed to sit 3 cm downstream of the target position between the target and the FAUST array. The slots were angled to allow the passage of particles only in narrow and well defined angular ranges. The thickness of the piece of tungsten needed to be thick enough to stop 60 MeV alpha particles (the maximum of the calibration beams). The resultant design is

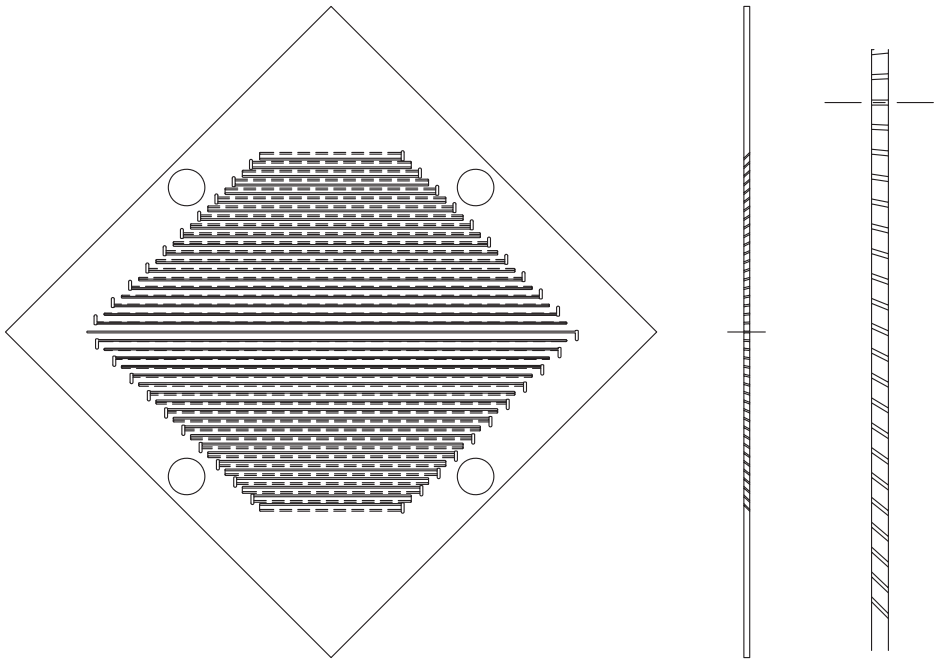

Figure 2.15: CAD drawing of the mask, demonstrating the different angles of the slits.

shown in figure 2.15. The left figure shows where the angled slits hit the front (solid) and back (dashed) of the mask, where all of the slits are slanted to allow maximum passage of particles to the detectors in FAUST. The middle rectangle shows a side view of the mask (note dashed center line) with the target position to the left, FAUST silicons to the right. The far right of the figure shows a zoomed in side view, where the middle stripe is perpendicular to the plane of the mask, while the lowest stripe has the maximum angle, to reach the detectors with the largest θ in Ring E.

A tungsten mask meeting these specifications was manufactured by wire EDM by Reliable EDM in Houston, TX. The actual mask is shown in figure 2.16. The mask allowed each of the detectors to "see" the collimated source or scattered α beam. The mask was used in-beam and with a collimated thorium source. Using the local position and the position of the detector in the FAUST design, a global position of the incident particle within the array can be determined.

The front plate of FAUST is designed to shield the detectors of FAUST from charged particles

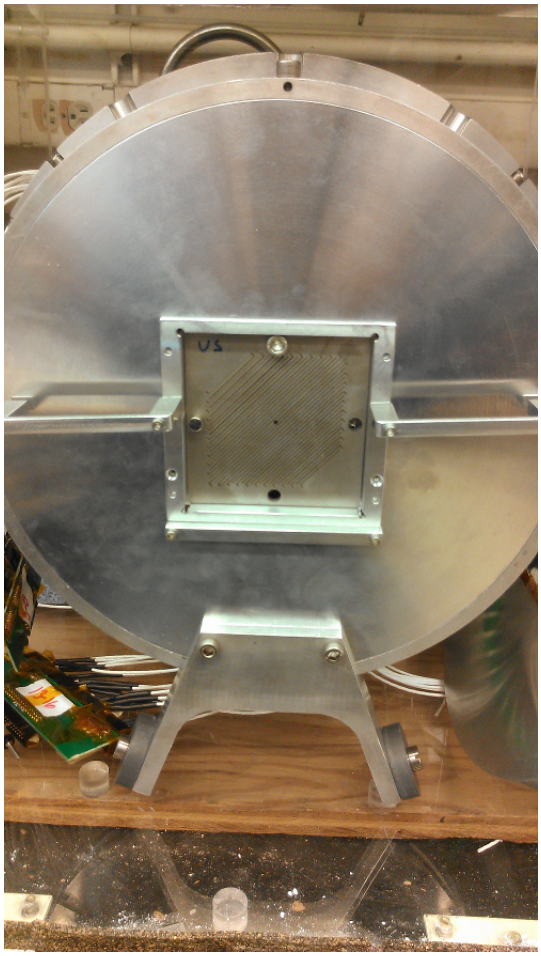

Figure 2.16: Mask on FAUST.

originating upstream of the target position. The mask needed to be set back into the front plate in order for each of the detectors to "see" the collimated source or scattered α beam. A modified front plate (with a plug for regular running) and an assembly to mount the mask were also manufactured. It is shown on the front plate in figure 2.16 and in a CAD drawing with the mounting structure for holding a collimated ^{228}Th source at the target position in figure 2.17.

A projection of the position of each alpha particle onto a plane 3 cm from the target (on the FAUST front plate) creates a visualization of the array from the target. This projection is shown below in section 2.4 for a source run using a collimated ^{228}Th, cut on the highest alpha energy. These stripes were used to assure the relative position alignment of the detectors was correct.

The variability in relative position of the silicon surface once the detector is fully mounted in the

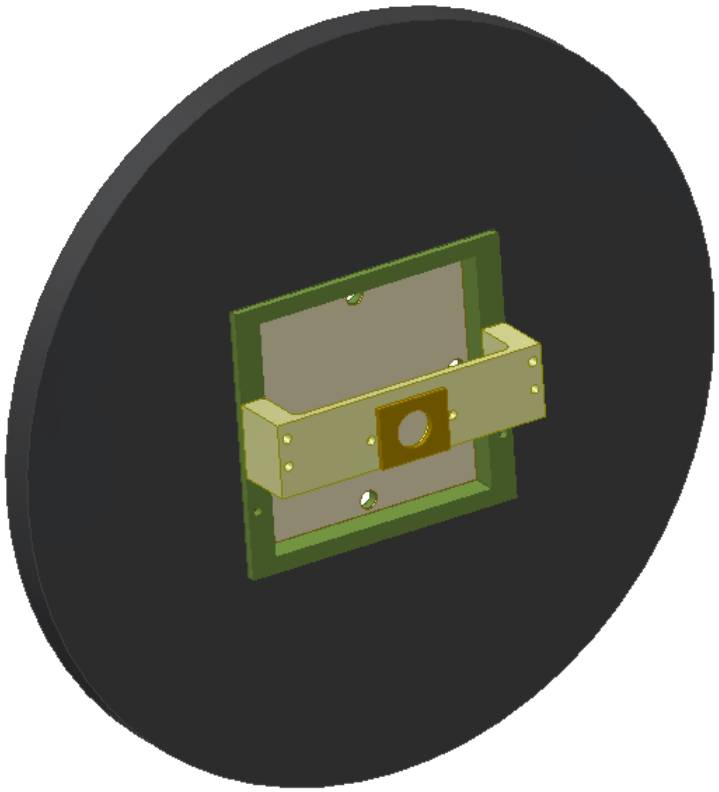

Figure 2.17: CAD drawing of assembly to hold collimated Th source at a fixed distance (target position) from the mask on FAUST frontplate.

beamline, with all of the points of connection, is less than 1 mm, which translates to a very small angular uncertainty. The treatment of the raw position signals described in section 2.2.3 gives a local x and y position on the detector. Due to offsets in the electronics, the area these local positions cover can be somewhat less than the 2x2 cm covered by the DADL detectors. This is accounted for by a stretching parameter in the calibration database, which increases the local position to cover the appropriate amount of area, while taking into account the fact that the guard ring means that the active area of the detectors does not go to the physical edge of the detector. When the positions of stripes of alpha particles on the detector are viewed in local space, large differences in gain between the two front or two back signals would be apparent in a squished version of the anticipated striped

pattern on the detector. Regularly sized stripes across the detector faces, properly aligned, mean that the position data is ready for calibration.

The silicon and cesium iodide signals from each FAUST telescope were used to find the identity and momentum of each light charged particle detected in the FAUST. This involved energy calibrations for the silicon detectors (section 3.1), isotopic particle identification using the ΔE-E technique (section 3.2) and energy calibrations for the cesium iodide detectors (section 3.3) of each telescope.

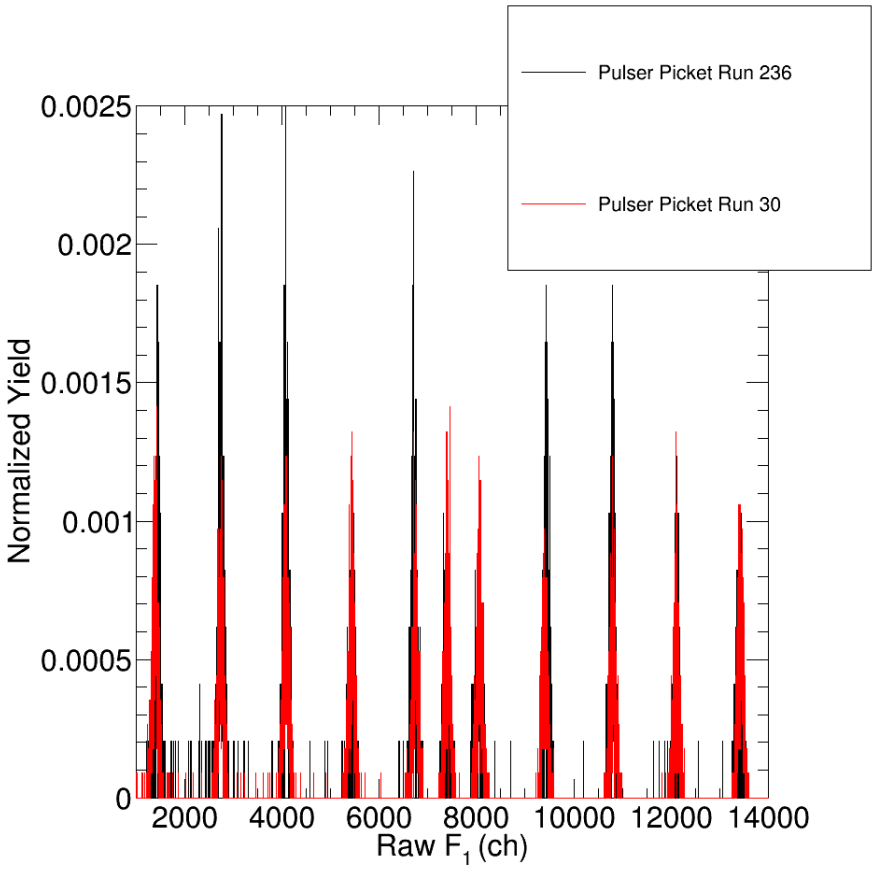

Figure 3.1: Pulser picket run at 1x, 2x, 3x, 4x, 5x, 5.5x, 6x, 7x, 8x, 9x, and 10x over the entire range of the ASIC shaper on detector 30 of FAUST. Run 236 was taken at the end of the Ca beam run (spring 2015). Run 30 was taken at the end of the Ar beam run (fall 2014). The silicon signals were stable over time.

3.1 Silicon Calibrations

The silicon calibration is described below. This includes the position correction due to the energy defect (section 3.1.1), the energy calibration in section 3.1.2, and the calculated signal in the case of front or back signal below the channel threshold or saturated in energy, discussed in section 3.1.3. The silicon calibration also includes a check of the position signals being treated appropriately in section 3.1.4. Silicon detector characterization and energy calibration was accomplished using α particles from a ^{228}Th source. In order to check the stability of the electronics gain and offset over time, pulser pickets were run with a pulser set to the same 11 settings after the argon and position beam times in fall 2014 and after the calcium beam in spring 2015. The electronics channels for the silicon signals were stable over this time, as shown in figure 3.1.

Calibration beams were used at the conclusion of the argon and mask beamtimes (fall 2014) and at the conclusion of the calcium beam (spring 2015). Two different calibration beams were used for this purpose, each scattered off of a 12 mg/cm^2 thick ^{nat}Au target. One beam was comprised of 15 MeV/nucleon α, the other was a molecular beam of p-α at 10 MeV/nucleon.

3.1.1 Position Correction

The position-sensitive capability of the DADL detectors allowed an investigation of and correction for the position-dependent nature of the energy distribution due to the electrons' passage through the resistive surface in the Si detectors. The "front" of the DADL detectors is defined as the surface facing the target position, the "back" is the face oriented towards the CsI(Tl) crystal.

When a ^{228}Th source is placed in front of the FAUST silicon detectors for calibration, plotting Front(Back) 1 vs Front(Back) 2 from either face (Front or Back) reveals the six distinct lines of single-energy α particles emitted by the source, shown in figure 3.2. As shown clearly in figure 3.2, the bands have a slight curvature to them.

A raw spectrum of Front 1+Front 2 (F_1+F_2) is shown in figure 3.3. The FWHM of the highest peak is 146 channels. This is 1.3%, which is not bad, but we can make it better. This sum is approximately proportional to the energy deposited in the detector, but must be corrected for the

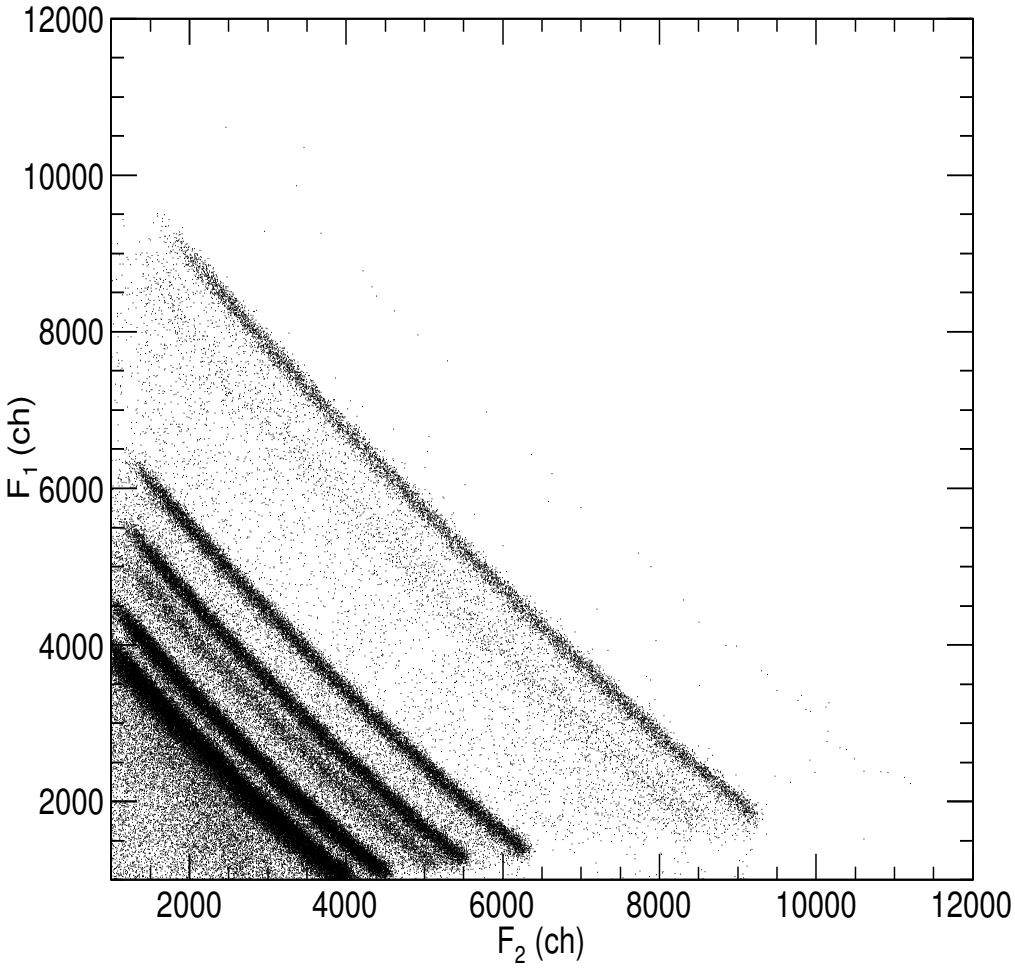

Figure 3.2: Raw data for a ^{228}Th source on detector 22. Signal from side 1 of Front vs side 2 of Front on detector 22. Note the slight curvature of the lines.

position defect which arises from the resistive surface of the detector. In order to correct for the position defect, the sum (raw energy) vs the difference (raw position) of the raw signals (sum = chF_1 + chF_2 and difference = chF_2 - chF_1) was plotted. This is shown in figure 3.4 with a cut applied to remove small signal amplitudes corresponding to electronic noise. If the energies deposited by the single energy alpha particles were not dependent upon the position at which the alpha particle hit the detector, these lines would be flat and parallel to the ordinate.

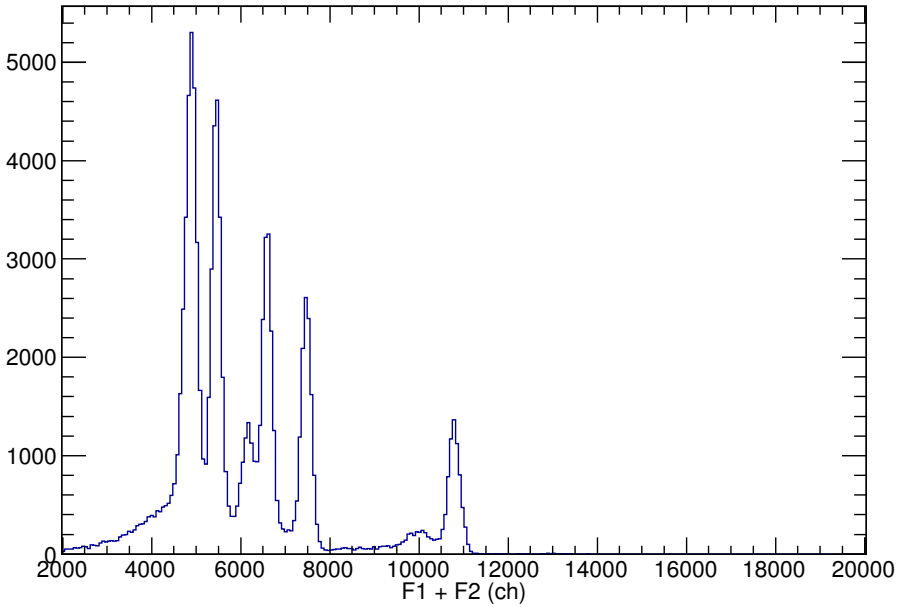

Figure 3.3: Energy spectrum of the alpha particles emitted by the ^{228}Th on detector 22. The raw FWHM on the highest energy alpha from the thorium is 145 channels.

This requires a correction to be made to the energies before they can be properly calibrated. A quadratic fit of each of the lines corresponding to monoenergetic alpha particles was performed to determine the curvature of the line (a), the linear component (b), and the y-intercept (c). In this case, when x=0, the alpha particle hit the middle of the detector. The results of these fits can be seen in Figure 3.4. The parameters corresponding to each of the fits are shown in Table 3.1.

The non-linear components of this fit are then subtracted from the overall energy to obtain a corrected spectrum and improve the energy resolution. Table 3.1 and figures 3.5 and 3.6 demonstrate that the curvature and linearity of the fits vary with the energy of the α particles. The "c" parameter of the fit is the sum and position where the single-energy alpha loses the greatest amount of energy across the resistive surface. In order to remove the position-dependence of the energy, the "a" and "b" parameters were plotted with respect to "c", as shown in figures 3.5 and 3.6 so as to characterize the curvature (a) and nonlinearity (b) as a function of the energy. These were fit with linear fits.

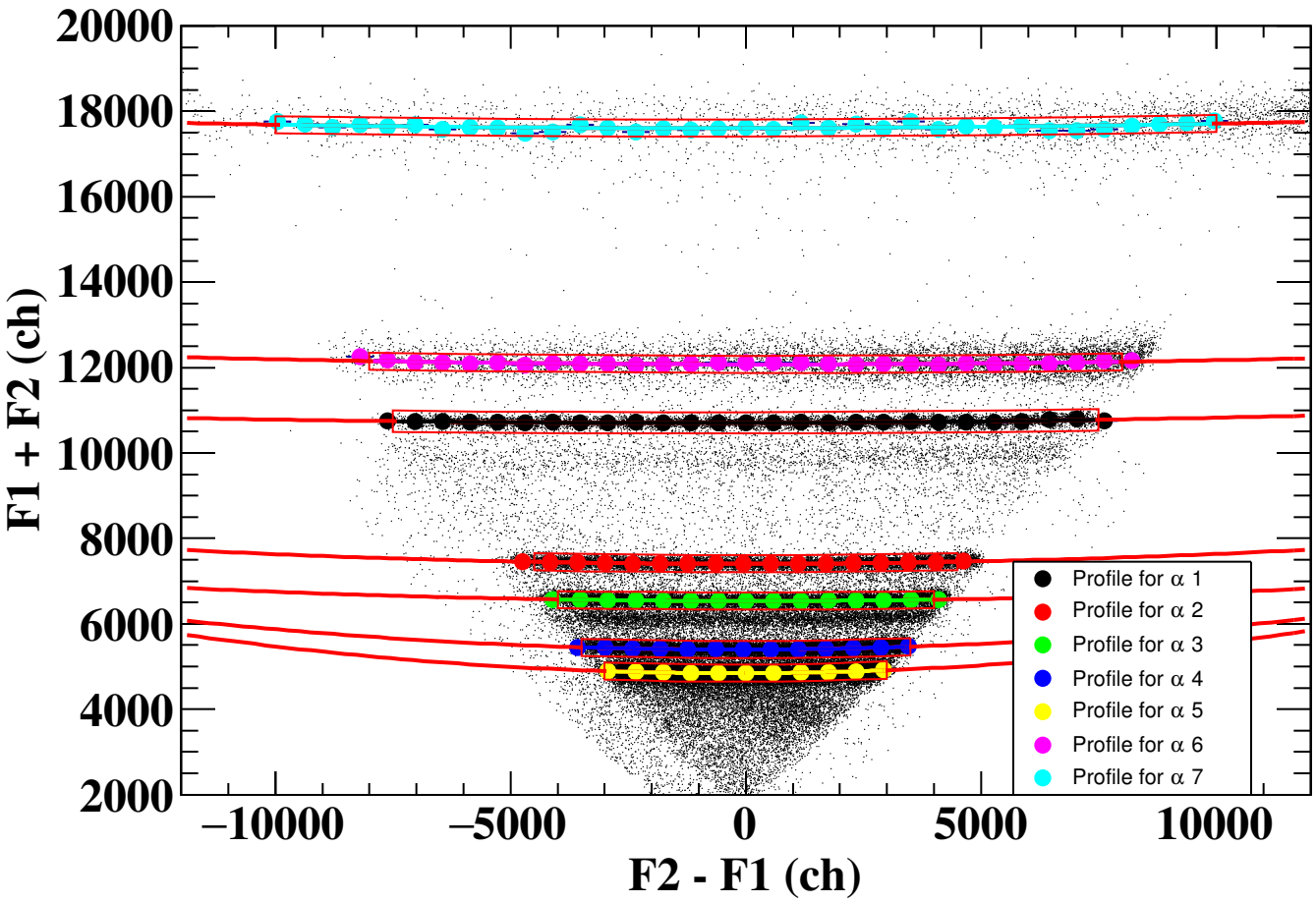

Figure 3.4: Sum vs difference of front signals plotted for ^{228}Th source and calibration beams of p-α at 10 MeV/nucleon and α at 15 MeV/nucleon on detector 22. These lines are somewhat parabolic in shape, and asymmetric about zero.

Because the magnitude of a and b changes with the energy deposited, the slope and intercept from figures 3.5 and 3.6 can be used to account for them at different energies. The entire equation for the corrected energy can be written as follows:

$$F_{corr} = s - a(s) * d^2 - b(s) * d, \tag{3.1}$$

where F_{corr} is the corrected sum of the front signals, s is the sum of the two signals, d is the difference of the two signals, a(s) is determined by the fit of a vs c and b(s) is determined by the fit

α	a (ch^{-1})	b	c (ch)
1	1.00E-8	2.24E-3	10704
2	2.28E-6	2.73E-4	7406
3	2.07E-6	-6.20E-4	6535
4	4.93E-6	1.97E-3	5399
5	6.62E-6	3.57E-3	4846
6	1.07E-6	-1.15E-3	12076
7	9.23E-7	1.25E-3	17607

Table 3.1: Showing the fit parameters for the quadratic fit of each of the alphas from figure 3.4.

of b vs c.

Because the position-dependent energy correction also depends upon the energy of the particles, it is desirable to empmirically determine the correction over the widest range of energies possible. In order to position-correct the energy spectra over a wider range of energies, the calibration beams were used along with the ^{228}Th source runs to determine an appropriate correction for light-charged particles (LCPs). The fit of all of these is shown in figure 3.4. Alphas 1-5 are, in order of descending energy, the alphas emitted from the ^{228}Th source. Alpha 6 is approximately 8.2 MeV, the amount deposited in the Si from the 15A MeV α beam. Alpha 7 is the α from the p-α at 10 MeV/nucleon beam, 11.6 MeV.

The lines are now straightened and horizontal, which improves the effective energy resolution considerably. The resultant corrected (but still uncalibrated) spectrum is shown in figure 3.7. The FWHM is now 101 channels on the raw spectrum. Even a merely cursory comparison between figures 3.3 and 3.7 shows the effective resolution of the detector is much improved by this correction. The raw energy vs position graph for the back of the detector (closest to the CsI crystal) was fit in an analogous way and the energy determined from the back signals was also corrected.

3.1.2 Energy Calibration

Following the position correction, the centroid of each Th peak was calculated, and a calibration from corrected channel to energy was obtained with a linear fit. Aluminized mylar was in

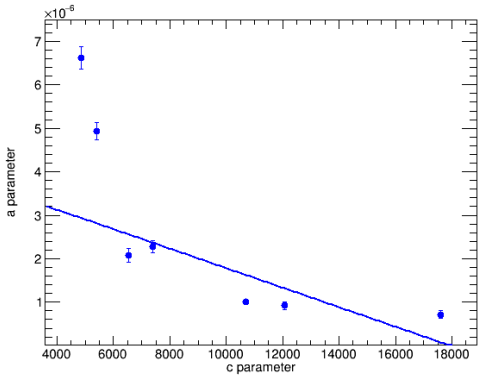

Figure 3.5: Quadratic component of fit a vs y-intercept for each fit for detector 22 from figure 3.4. Parameters from all 7 alphas are fit with a linear fit.

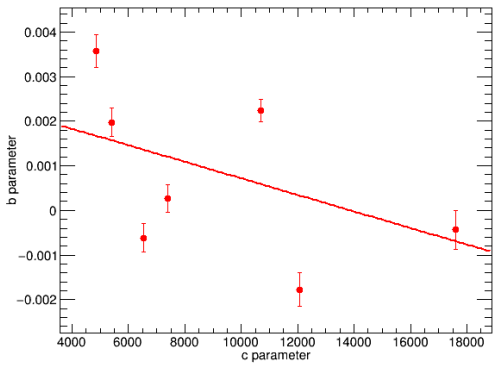

Figure 3.6: Linear component of fit b vs y-intercept for each fit for detector 22 fom figure 3.4. Parameters from all 7 alphas are fit with a linear fit.

front of the silicons to act as a delta-ray shield, as discussed in section 2.2. The mylar was of varying thickness between the radioactive source and the Si detectors and was taken into account in determining the incident energy of the alphas using the SRIM (The Stopping and Range of Ions in Matter) range tables [47, 48, 49]. The effective mylar thicknesses due to angle of the center of the detector and the relevant alpha energies in MeV are noted in table 3.2. The energy resolution for the highest energy alpha (8.785 MeV) was below 2% for all detectors, though many were significantly better; for example, detector 22 above had around 0.9% resolution around 9 MeV.

Figure 3.8 shows several calibrated ^{228}Th spectra recorded from the DADL front (top panel) and back (bottom panel) with detector 21 at several points during the experiment running. The silicon energy calibration was done once, before the first beam time. The four spectra lie on top of each other, even though they were taken at distinct times over a period of several months. This in addition to the pulser picket in figure 3.1 lends confidence to the silicon calibration over time.

The silicon energy extracted from the front signals and the back signals of the DADL were required to be within 300 keV or 5% of one another (whichever is greater) in order for the particle to be kept. The particles which pass these two cuts are demonstrated in figure 3.9. About 5% of particles do not pass this energy requirement.

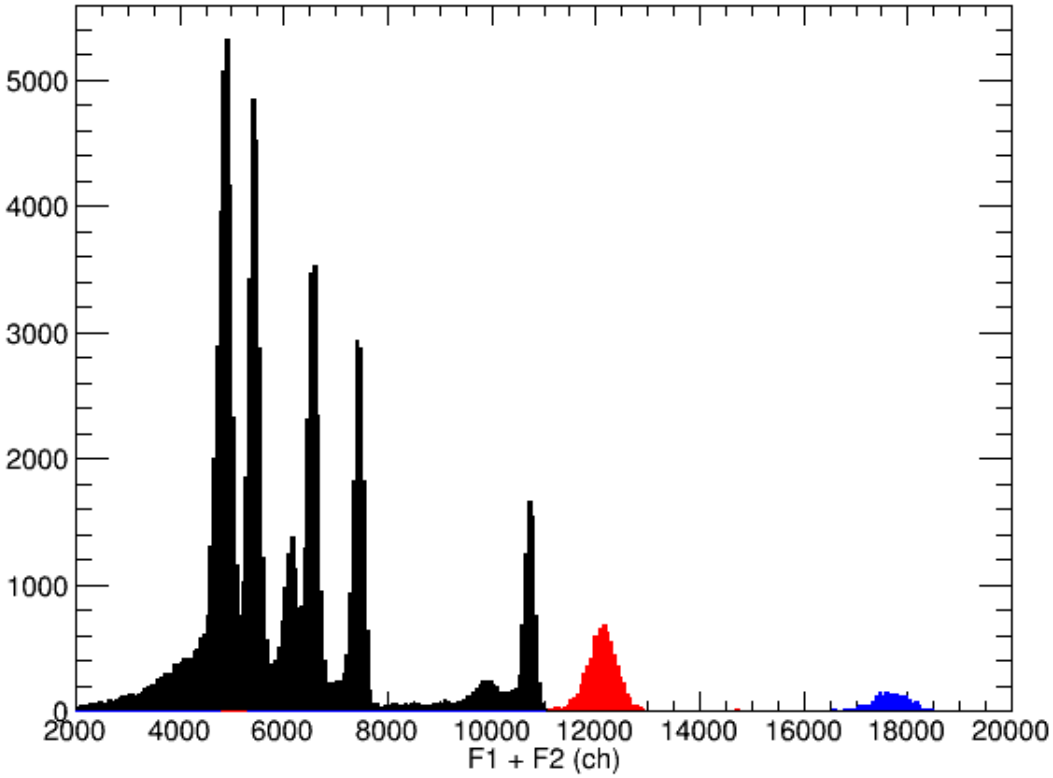

Figure 3.7: Position-corrected energy spectrum of the alpha particles emitted by the ^{228}Th on detector 22 and the calibration beams (red and blue). The raw FWHM on the highest energy alpha from the thorium (black) is now 101 channels, or 0.9%. This corresponds to 83 keV for a 9 MeV peak.

3.1.3 Missing Fourth Signal Calculation

Particles used in the silicon energy calibration were required to have energy signals above the threshold and below saturation of all four channels of the DADL detector. If a charged particle deposits very little energy in the detector or the charge-splitting due to position causes one of the four silicon signals to be very small, it is possible to measure three signals above threshold and have a "missing" fourth silicon signal.

For particles where three of the four signals were measured in the appropriate range, the equivalence of energy signals on the front and the back of the DADL detectors allowed for the recon-

Detector Position	Effective Mylar (mg/cm^2) Thickness	Th α Energy (MeV)				
		8.785	6.778	6.288	5.685	5.423
0	4.785	5.64	2.532			
1	4.792	5.635	2.523			
2	2.555	6.838	4.829	4.201	3.386	3.012
3	2.569	6.825	4.816	4.187	3.369	2.994
4	2.588	8.214	6.083	5.556	4.892	4.603
5	2.600	7.203	4.802	4.171	3.351	2.975
6	2.637	7.170	4.757	4.122	3.295	2.914
7	0.878	8.214	6.116	5.591	4.929	4.643
8	0.888	8.234	6.108	5.583	4.920	4.633
9	0.917	8.214	6.083	5.556	4.892	4.603
10	0.948	8.198	6.063	5.536	4.870	4.579
11	0.971	8.183	6.045	5.516	4.894	4.557
12	1.049	8.134	5.985	5.452	4.779	4.484

Table 3.2: Degraded alpha energies after mylar in front of each detector position for each of the alphas from the thorium source, calculated according to SRIM (srim.org). Effective thicknesses of mylar are calculated for the center of the detector.

stitution of the missing fourth signal. Because the position correction was applied to sharpen the effective resolution of the silicon detectors before the missing fourth signal could be calculated, the correlation between the position corrected data and the raw sum is necessary to calculate a missing signal. For particles with four legitimate signals, the position-corrected sum of the fronts vs the sum of the back two signals could be plotted, as well as the sum of the front signals vs the position-corrected sum of the back signals. These are both demonstrated in figure 3.10. A line was fit to both of these cases, which allowed for the calculation of the missing fourth signal in the case where the 4th signal was not above the noise. This had the desirable effect of increasing the total number of charged particles that could be identified and energy calibrated.

The bulk of the particles that were able to be resurrected via this method were low energy Z=1 particles (threshold effect) and high energy Z=2 particles (saturation effect). The success of adding this missing silicon channel back into the data is assessed in section 3.4. The range of energy of particles that were added back into the data set is demonstrated in figure 3.19. This is crucial for

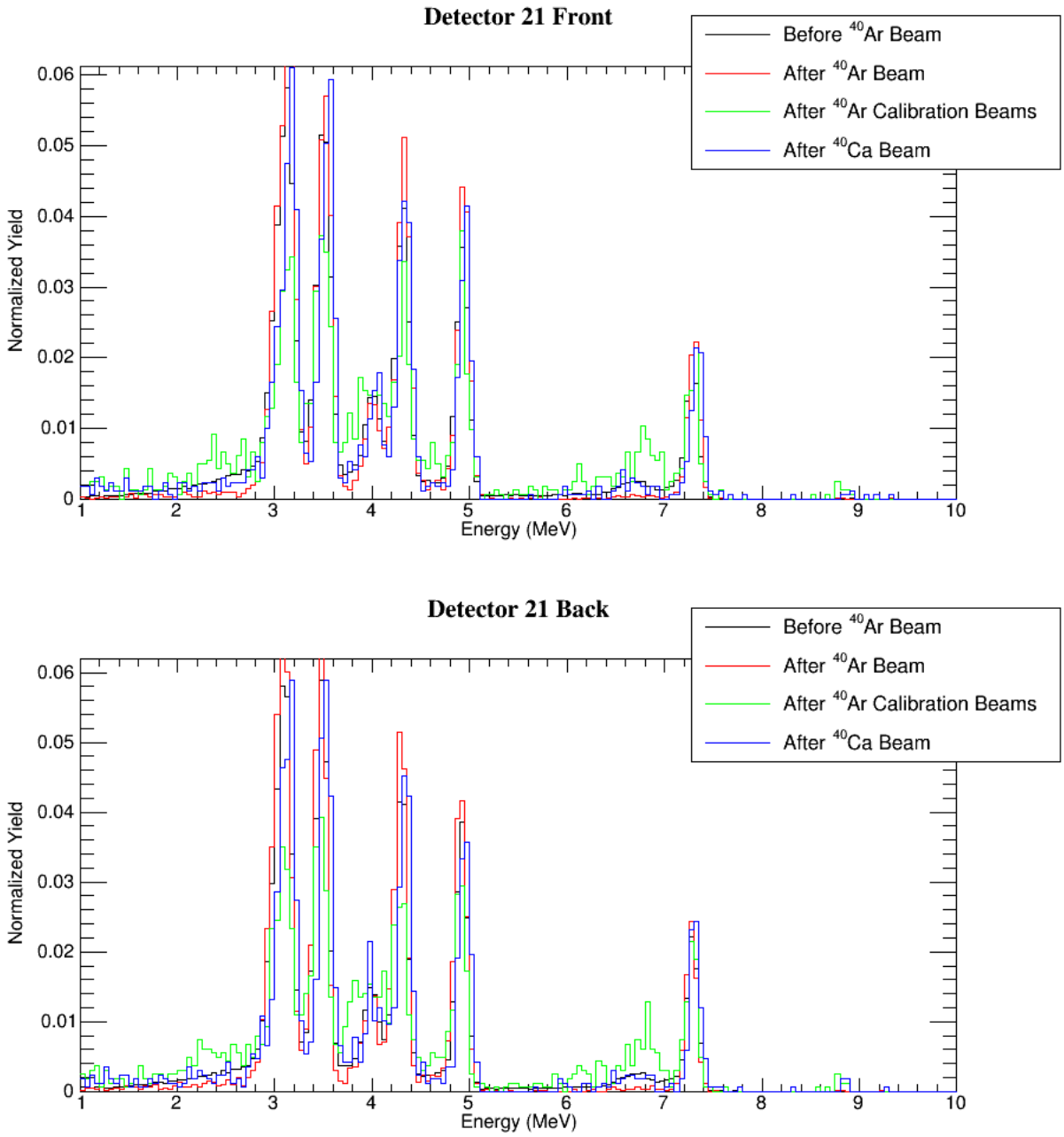

Figure 3.8: Th spectra taken at various times during the course of the experiment. The silicon calibration remained the same and the different peaks of alphas line up quite nicely.

detecting as many protons as possible. About 5% of the total cohort of protons have positions calculated in this method, while less than 1% of alphas are added back into the data stream with a calculated fourth silicon signal.

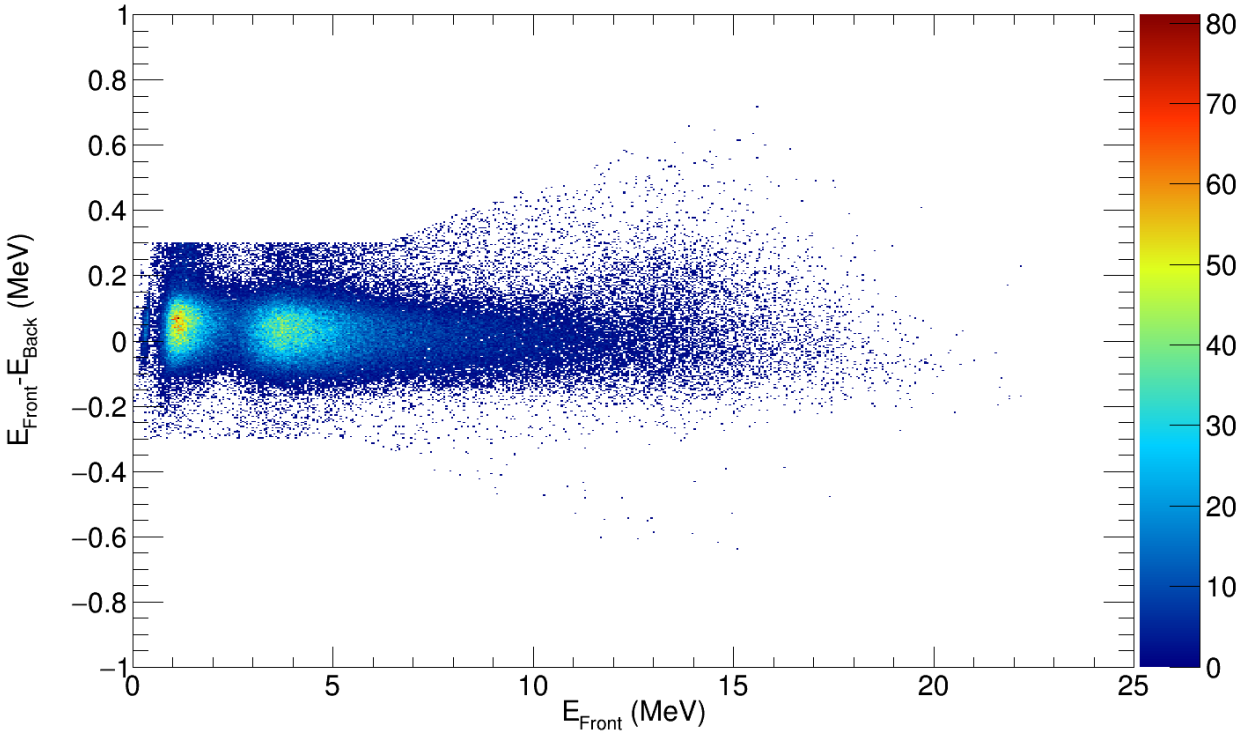

Figure 3.9: The difference between calibrated energy from the front and back of detector 21 vs the energy from the front for the Ar+Fe at 40 MeV/nucleon. The cuts on the data are described in the text.

3.1.4 Silicon Position

The resistive charge splitting described in section 2.2.3 allows calculation of a local position on the face of the silicon detector (front or back) using the ratio of the difference to the sum of the two signals (F_1, F_2 or B_1, B_2, equations 2.1 and 2.2). An example of this local position is shown for particles from the 40 MeV/nucleon Ar+Fe reaction in the left hand of figure 3.11. The silicons are 2x2 cm squares, so the local position of the particles hitting the surface of the detector should go from -1 to 1 cm in x and y in local space. If the offsets of the two channels from which local position is calculated are large, the local position fill the square. A scaling of the detector was added to the calibration database to compensate for this. The signals from the same DADL are

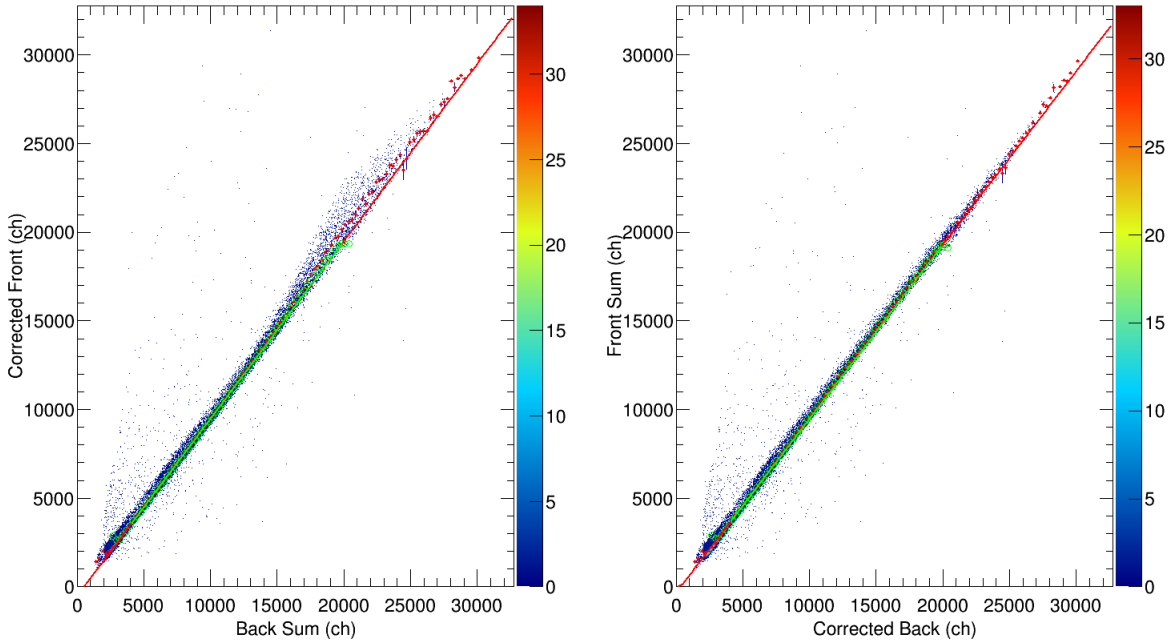

Figure 3.10: Correlation between the corrected sum and uncorrected sum of the front and back of the DADL detector. The fit to this narrow line is used to calculate the missing fourth signals possible from any side of the detector. Representative detector (detector 21) for representative system (Ca+Ni at 40 MeV/nucleon). The range over which this fit is made is indicated in green.

treated as similarly in the electronics as possible. If the gains were grossly mismatched, the stripes from the mask (right hand panel of figure 3.11 would be stretched to one side, but the width and positions of the stripes on the face of the detectors were approximately what was expected. For several detectors, a transposition of two signals was easily caught and corrected by looking at the apparent orientation of the stripes.

These local positions were then transposed to their global positions within the FAUST by using the known global theta and phi of the corners of the detector within the array. A projection of these global positions onto a spot approximately 3 cm from the target (approximately the front plate of FAUST) position results in figure 3.12 for the full range of light charged particles which hit the FAUST during the Ar+Fe system at 40 MeV/nucleon.

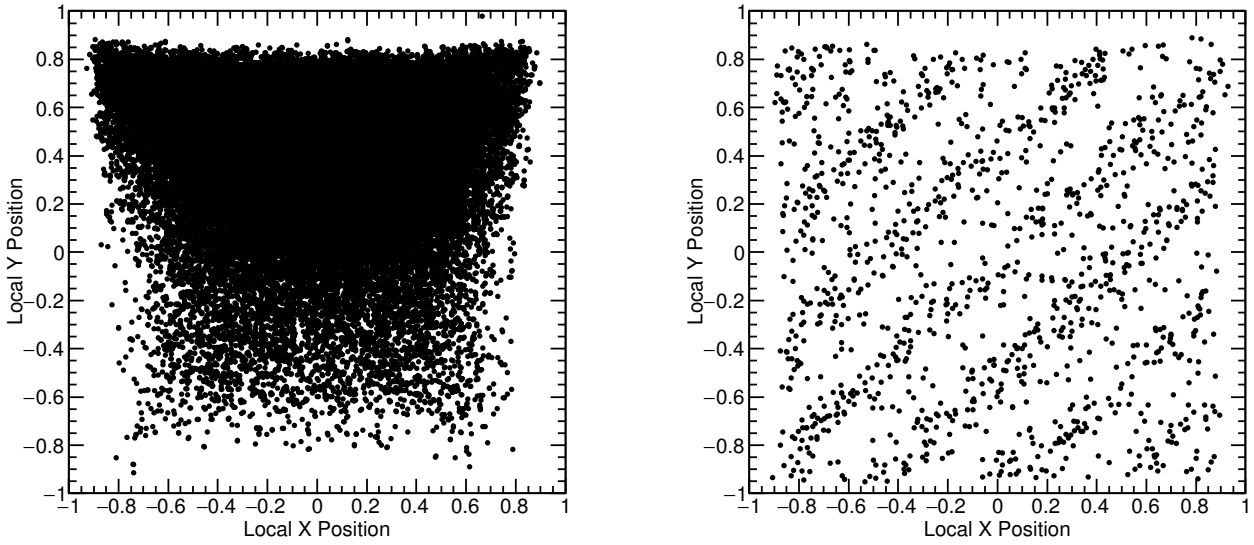

Figure 3.11: Local position of charged particles incident on detector 62. Left panel: Local position for charged particles on the detector surface from the reaction of Ar+Fe at 40 MeV/nucleon. Right panel: Highest energy (8.785 MeV) α from ^{228}Th source through the striped mask.

The tungsten mask described in section 2.4 was used as a check that the local positions of the detectors were transformed appropriately to their global position. The resultant alignment of the stripes is shown in figure 3.13 for the elastically scattered p-α calibration beam. The detectors which are furthest from the target position (rings A & B) show the best stripes with the scattered beam. Rings C-E are shown with greater advantage when a collimated Th source is masked from the detectors, instead. The ^{228}Th source, gated on the highest energy alpha particle, is shown in figure 3.14.

3.2 Particle Identification

Charged particles deposit energy in the two detectors of dE-E telescope in a way dependent on their charge and mass. This allows for separation and identification of particles. The excellent separation between the bands from different particle types is demonstrated in figure 3.15. The characteristic band separation of different particle types allows for visual particle identification. In this figure, the lowest and left-most band is protons, above and to the right are particles increasing

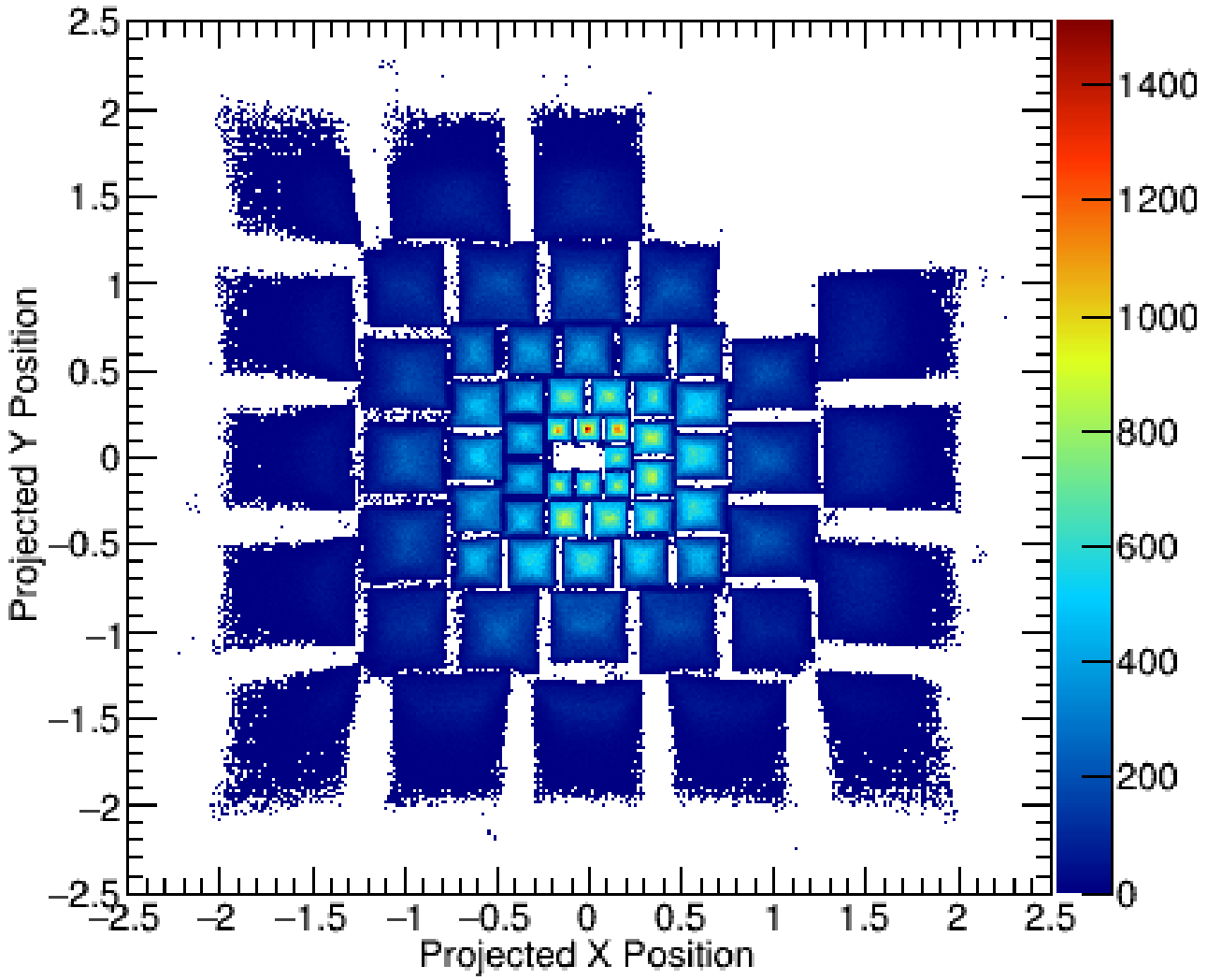

Figure 3.12: Projection of the particles resultant from the reaction of Ar+Fe at 40 MeV/nucleon hitting the detectors of the FAUST.

in charge and mass. In order to identify these particles on a case-by-case basis, the signals detected in the silicon and cesium iodide are processed to linearize the particle identification (PID) values so that simple cuts can be used on PID values to determine particle Z and A.

An equation which is based roughly upon the Bethe-Bloch equation was used to linearize the curves observed in the ΔE-E correlation in the manner used in [50]:

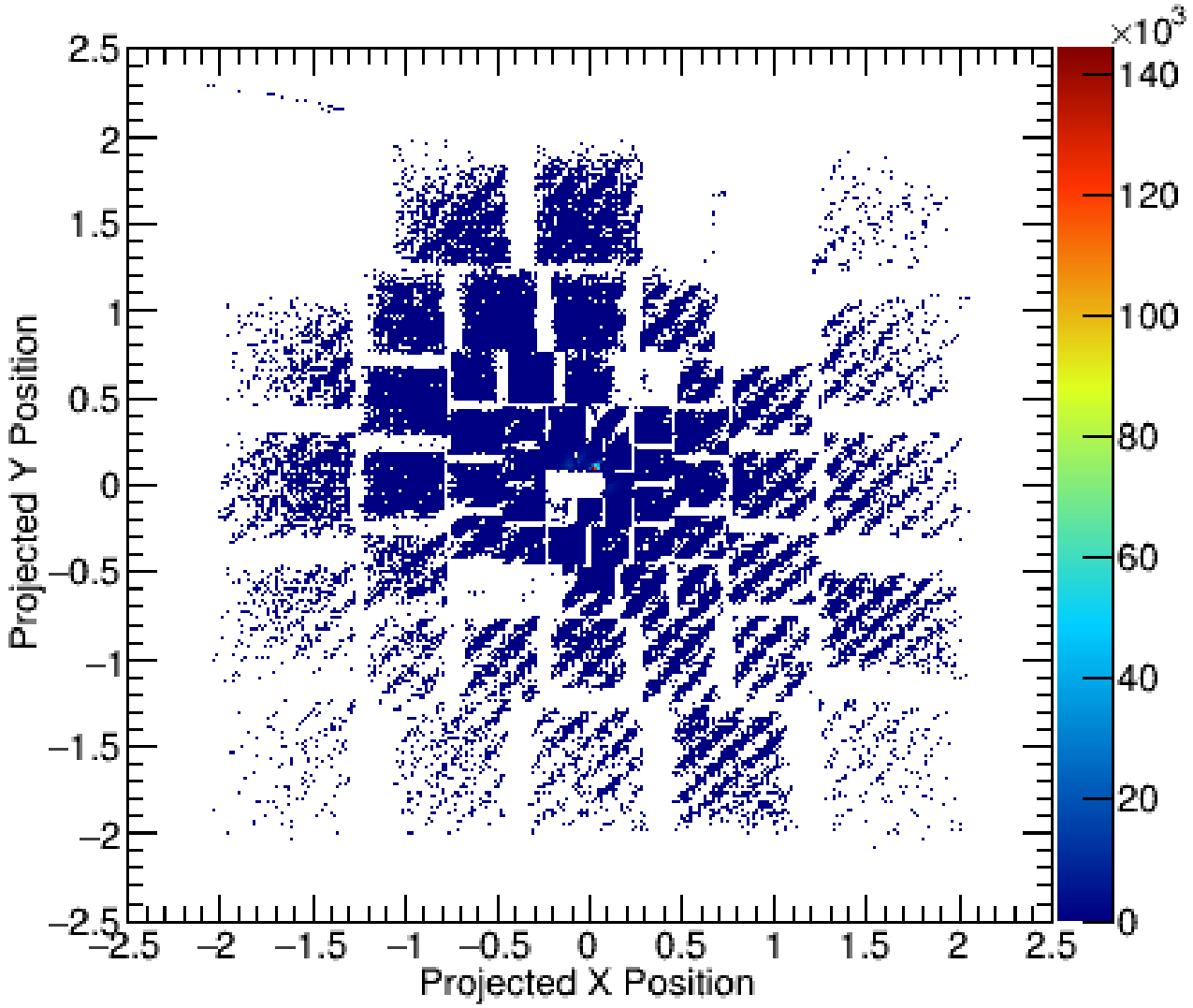

Figure 3.13: Projection of the elastically scattered calibration beam alphas from the molecular p-α at 10 MeV/nucleon hitting the detectors of the FAUST through the tungsten mask.

$$PID = bln(p_0) - ln(b\Delta E) - (b-1)ln(E + p_1\Delta E) \tag{3.2}$$

where

$$b = p_2 - p_3\Delta E/p_4, \tag{3.3}$$

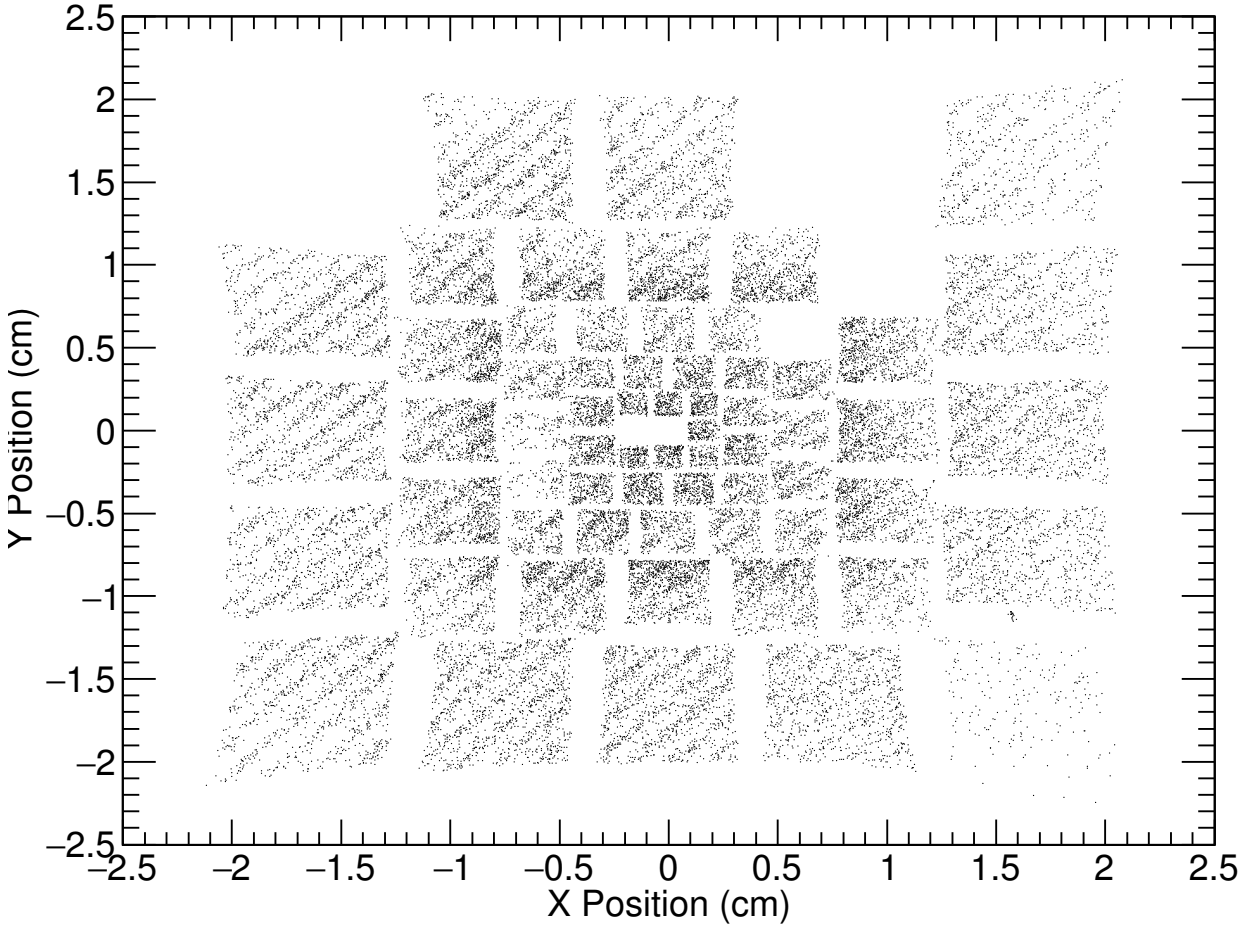

Figure 3.14: Projection of the ^{228}Th source alphas hitting the detectors of the FAUST through the tungsten mask.

$$\Delta E = m_{Si} C_{Si} + b_{Si} \tag{3.4}$$

and

$$E = m_{CsI} C_{CsI} + b_{CsI} \tag{3.5}$$

with the p_0-p_4 parameters varied by hand over a small range of values until linearized. The slopes and intercepts of the CsI and Si (m_{Si}, m_{CsI}, b_{Si}, b_{CsI}) calibrations were also fit parameters. The only significance of the PID values lay in the ability to separate particle types using a single variable,

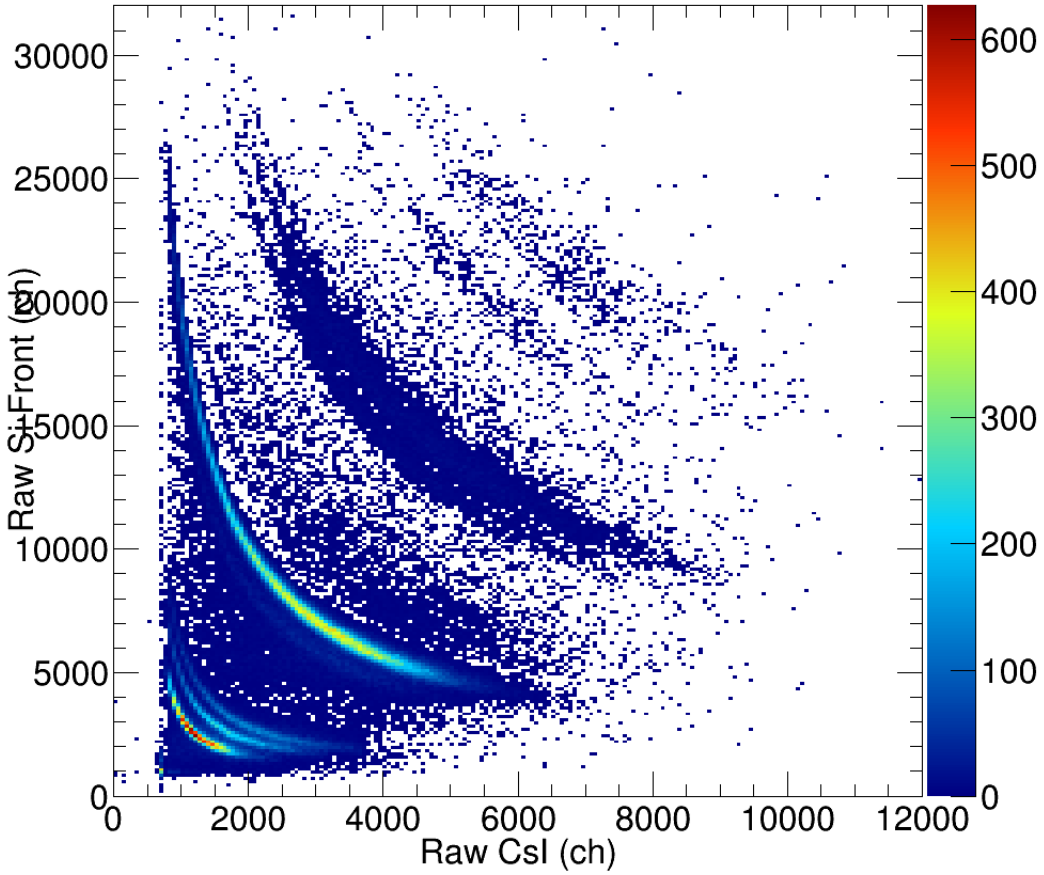

Figure 3.15: Raw 2D spectrum of a representative detector (21) showing reaction products from a representative system (Ar+Fe at 40 MeV/nucleon), demonstrating the excellent particle type resolution achieved in this experiment.

rather than the relationship between the energy deposited in the silicon and cesium iodide. The parameters for detector 21 are shown in table 3.3.

The silicon corrected sum is shown as a function of the linearized value (PID) in figure 3.16. Gates are applied to the PID value distribution to define the partcle types, as indicated by the vertical lines in figure 3.16.

Parameter	Value
p_0	1.00E-8
p_1	2.28E-6
p_2	2.07E-6
p_3	4.93E-6
p_4	6.62E-6
m_{Si}	1.07E-6
b_{Si}	9.23E-7
m_{CsI}	1.07E-6
b_{CsI}	9.23E-7

Table 3.3: Example parameters for PID calibration of telescope 21, a typical detector. The parameters were all varied until the PID values were linearized, the parameters' values are not physically meaningful, so they can be considered unitless. The "energies" procured in equations 3.5 and 3.4 are not in MeV. The energy on the y-axis of figure 3.16 is the calibrated silicon energy.

3.3 Cesium Iodide Energy Calibration

The response of the cesium iodide detectors is non-linear with respect to the energy of the ionizing radiation, and depends on the Z and A of the particles [51]. Once particles were identified using the method described in Section 3.2, the light output (LO) of the CsI(Tl) crystal, read out by the photodiode, was plotted for each particle type vs the energy deposited in the cesium iodide (E) according to a SRIM calculation using the known thickness of the silicon and the calibrated energy deposited in the silicon. This plot of LO vs the E deposited in the CsI(Tl) for that particle type is shown in figures 3.17 and 3.18.

The LO of the CsI(Tl) crystal, incident on the photodiodes, can be parametrized as follows [51]:

$$LO = a_1 \left\{ E \left[1 - \frac{a_2 A Z^2}{E} ln\left(1 + \frac{E}{a_2 A Z^2} \right) \right] + a_4 a_2 A Z^2 ln\left(\frac{E + a_2 A Z^2}{A a_3 + a_2 A Z^2} \right) \right\} + a_5 \tag{3.6}$$

This equation was used to fit the LOvE histograms for protons and alphas resultant from reactions of ^{40}Ar+^{58}Fe and ^{40}Ca+^{58}Ni at 40 MeV/nucleon, detector-by-detector. Each light output measured in the cesium iodide corresponds to an energy deposited in that cesium iodide, based upon a SRIM

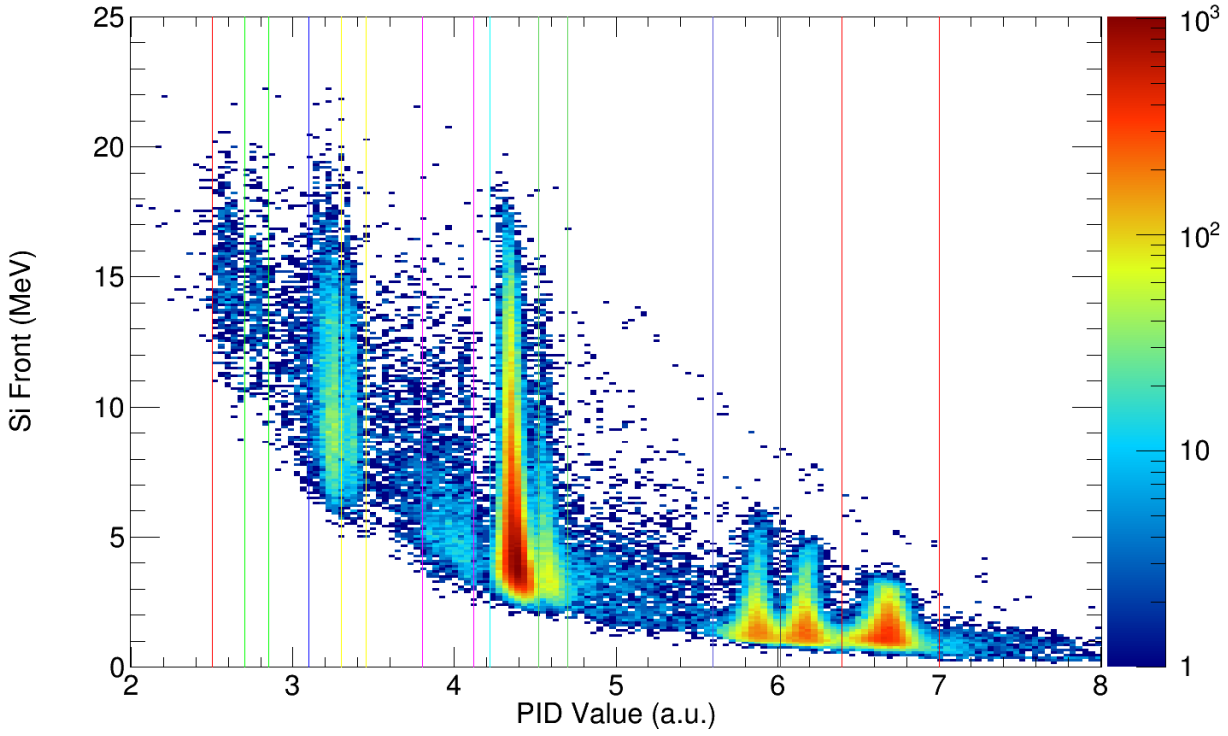

Figure 3.16: Calibrated Si energy vs PID value for detector 21, Ar+Fe at 40 MeV/nucleon.

calculation from the silicon calibration. The resultant fits using equation 3.6 are shown overlaid on the experimental data in figures 3.17 and 3.18. These fits were then used to determine the energy deposited in the cesium iodide crystal for Z=1 and Z=2 particles, respectively, in the experimental data. Total energy is determined by adding the ΔE deposited in the silicon and the remaining E deposited in the cesium iodide for each particle.

3.4 Quality Assessment of Calibrations

After the finalization of each of the calibrations discussed above, Z and A identified particles that met the energy requirements for their particle type were included in the physics events generated from the reduced raw data. Particles from detectors with reasonable energy and PID calibrations in rings C, D, and E were included. Figure 3.19 shows the calibrated dE-E histogram with the calculated missing fourth silicon signals, which still exhibits excellent particle identification

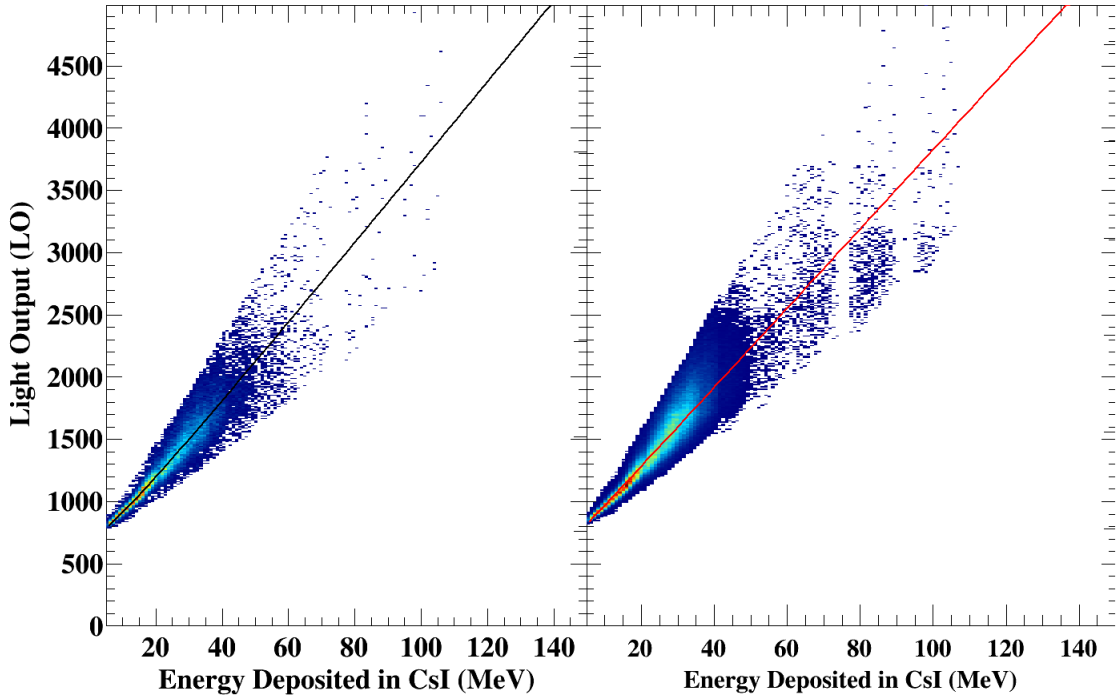

Figure 3.17: Light output vs energy for protons detected in detector 21. Left panel for Ar+Fe at 40 MeV/nucleon, right panel for Ca+Ni at 40 MeV/nucleon. Fit using equation 3.6 shown overlaid.

resolution. The bulk of the particles retrieved via this process are high energy Z=1 particles, which were important for the eventual extraction of proton-proton correlation functions. Many lower energy Z>1 particles, which deposit more energy in the silicon ΔE detector, were also recovered.

Another check that can be made of the physics events is to look at the calibrated dE-E spectrum in another way, cut on particle identification, as in figure 3.20. This space makes the success of particle identification cuts obvious. This figure shows the good separation of the different light charged particles considered in the rest of this analysis: protons, deuterons, tritons, helions, and alphas.

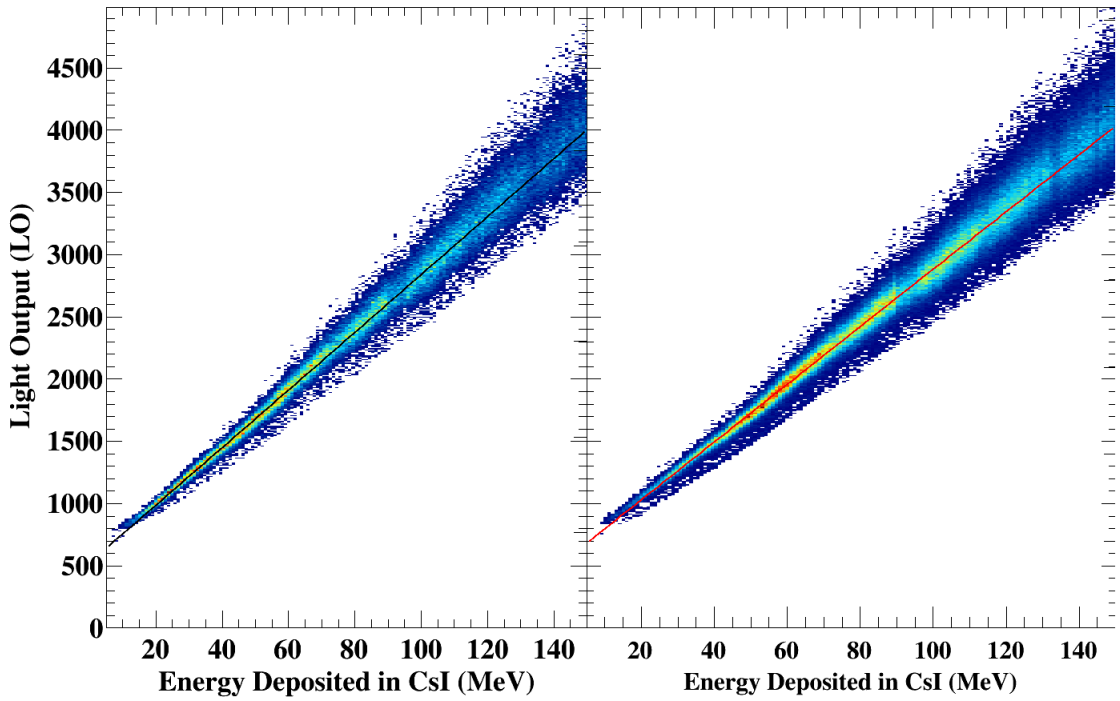

Figure 3.18: Light output vs energy for alphas detected in detector 21. Left panel for Ar+Fe at 40 MeV/nucleon, right panel for Ca+Ni at 40 MeV/nucleon. Fit using equation 3.6 shown overlaid.

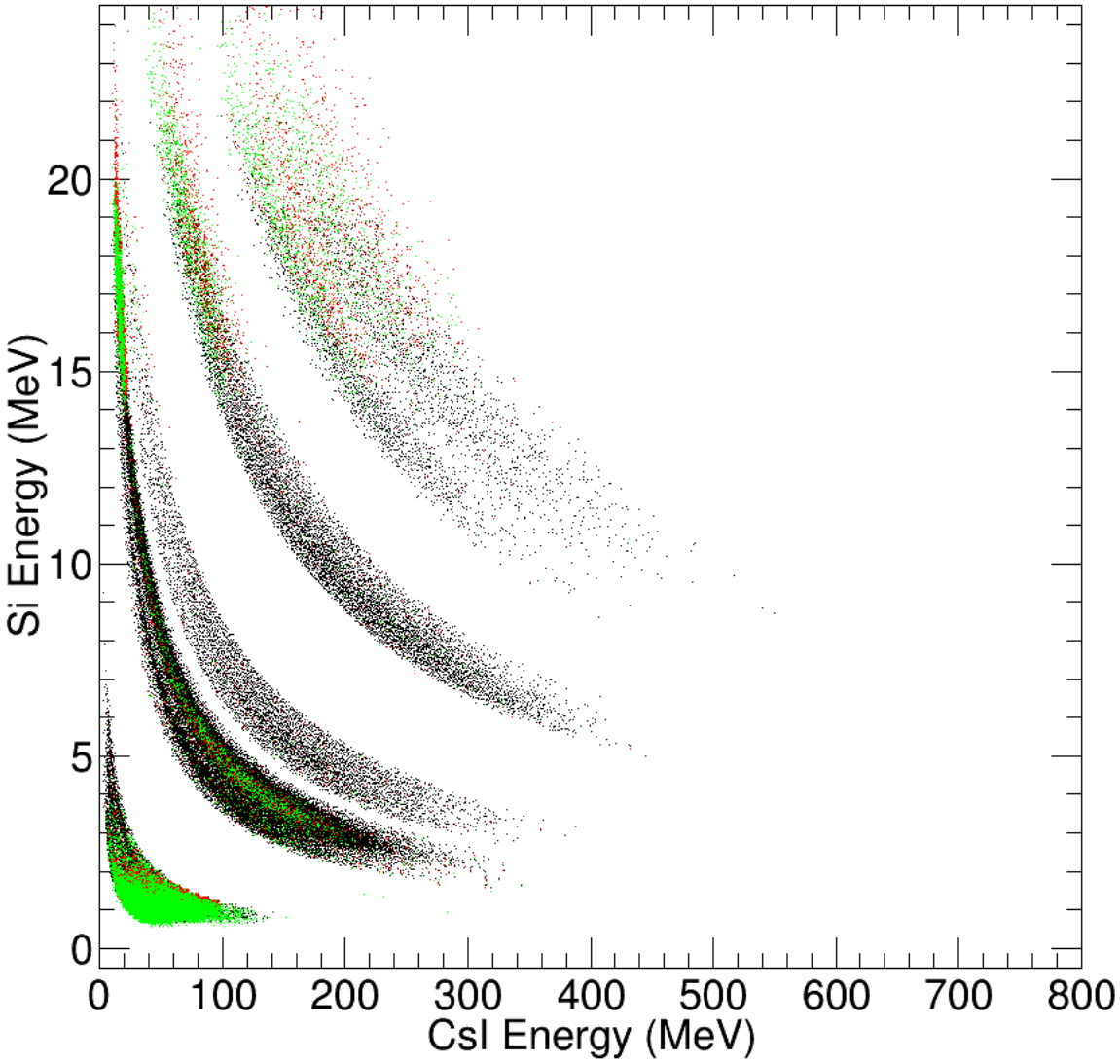

Figure 3.19: Calibrated dE-E histogram for particles that had five (4 Si + CsI) acceptable signals (black) and were added in as a calculated missing front (red) or back (green) signal. Representative detector (detector 21) for representative system (Ca+Ni at 40 MeV/nucleon).

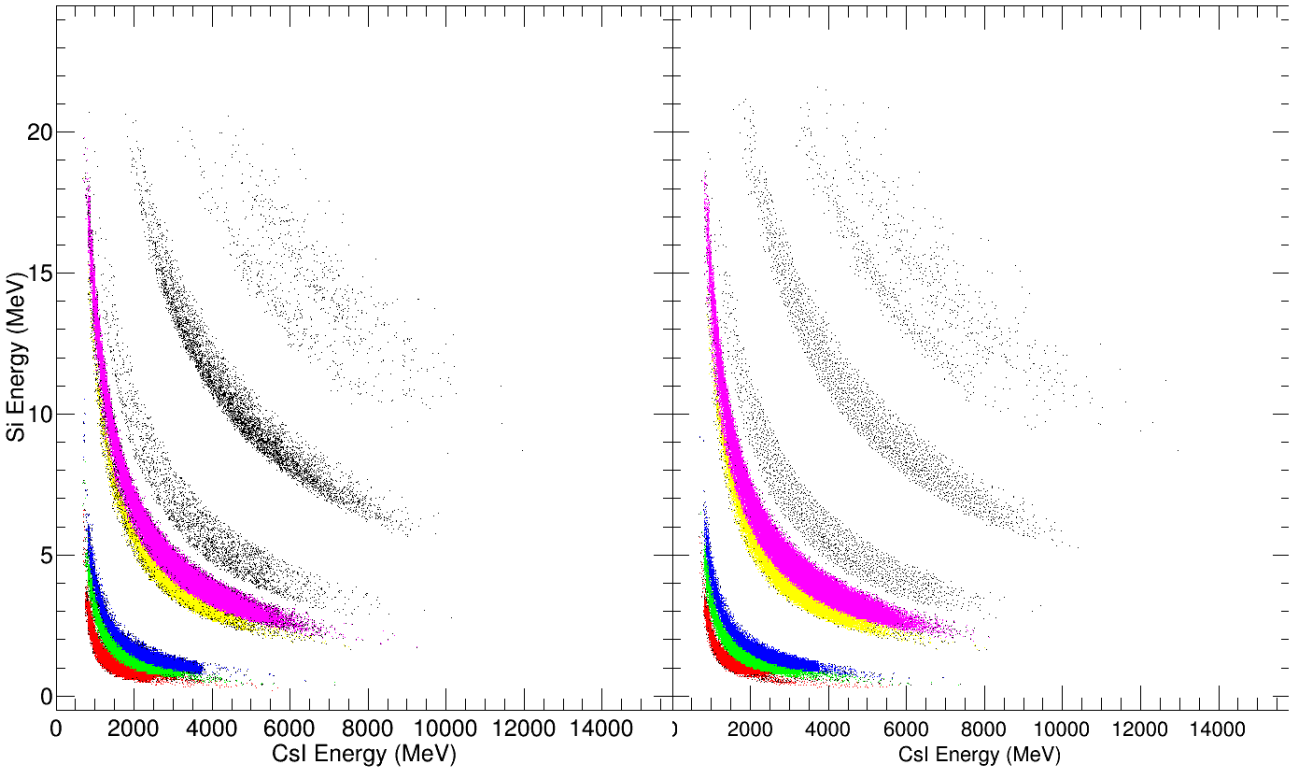

Figure 3.20: Calibrated dE-E plot for detector 21 for the two systems at 40 MeV/nucleon. The first 5 particle-identified isotopes are indicated by red (protons), green (deuterons), blue (tritons), yellow (helions), and pink (alphas) markers. Left: Ar+Fe at 40 MeV/nucleon, Right: Ca+Ni at 40 MeV/nucleon.

4 ANALYSIS

This chapter of the dissertation describes the analysis of this data set. This includes a comparison of energy and momentum distributions between experiment and model calculations in section 4.1. Correlation functions for light charged particles with well-known resonances are shown and discussed in section 4.2. The selection of events and proton pairs for construction of the proton-proton correlation functions and comparison of the different systems are shown in section 4.3. pBUU transport model simulations are discussed and compared to experimental data in that section, also.

4.1 Energy and Momenta of Light Charged Particles

The signals from the detectors were calibrated in the manner described in chapter 3 to isotopically identify and determine the energy of Z=1 and Z=2 particles which were the focus of this work. The resultant normalized energy spectra in the lab frame for protons, deuterons, tritons, helions, and alphas are shown in figure 4.1. Systems with the same beam energy display similar light charged particle distributions. The 40 MeV/nucleon beams extend further in energy. The particles have been truncated at the calculated punch-through energies for each particle type in a FAUST telescope with a 300 μm silicon. Protons are truncated at 98.6 MeV, deuterons at 132.3 MeV, tritons at 157.1 MeV, helions at 349.2 MeV, and alphas at 393.4 MeV.

The Heavy Ion Phase Space Exploration (HIPSE) event generator was designed to emulate heavy ion collisions at intermediate energies [52] and is well suited for the beam energy and mass range in which this experiment was performed. In order to compare to the experimental data and investigate how impact parameter can be extracted via experimental observables, HIPSE was run for all four of the systems studied in this work. The energy spectra in the lab frame for the light charged particles from the HIPSE event generator are shown for the Ca+Ni system in figure 4.2. The dashed line (unfiltered) shows the full data, all energies in all directions. The full line shows the filtered spectra of particles expected to be detected by the FAUST, based upon the geometry

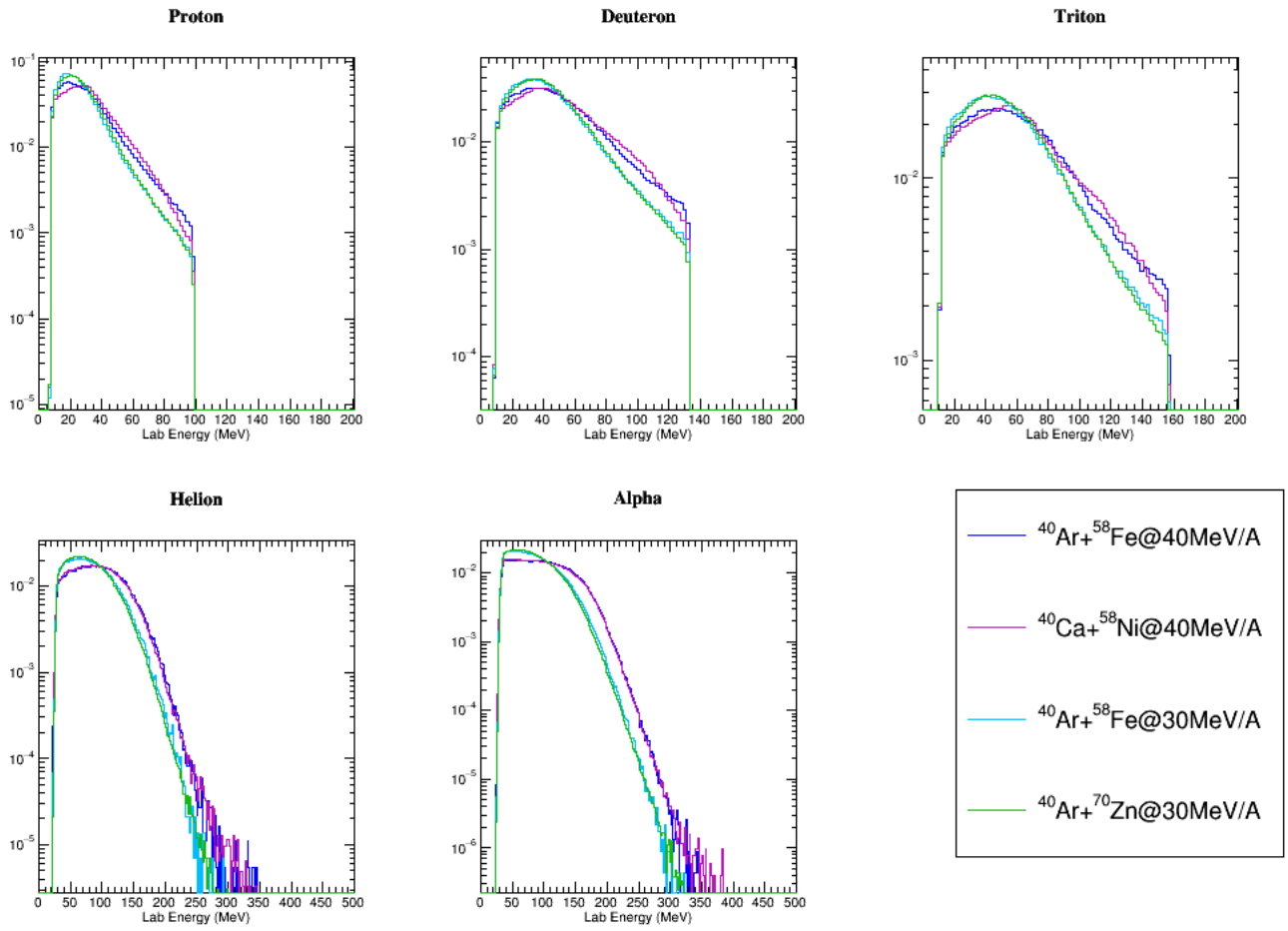

Figure 4.1: Energy spectra for light charged particles from all four measured systems, drawn normalized to compare the four systems.

and the energy of the particles. The energy cuts applied are the same expected punch-in and punch-through energies in a FAUST telescope with a 300 μm silicon from LISE++. The energy aceptance of the FAUST telescopes has a larger impact on the shape of the Z=1 particles than on the Z=2, shown clearly by the sharp cutoffs in the Z=1 filtered spectra. The unfiltered (dashed lines) spectra for protons decrease in yield by a little over a decade between 50 and 100 MeV. This is less steep than the experimental energy spectra over this same range.

As mentioned in the above discussion of figure 4.1, the two 40 MeV/nucleon systems and the two 30 MeV/nucleon systems match each other across a broad scale. The energy spectra for the 40 MeV/nucleon systems, Ca+Ni and Ar+Fe, cross one another twice for Z=1 particles. In the

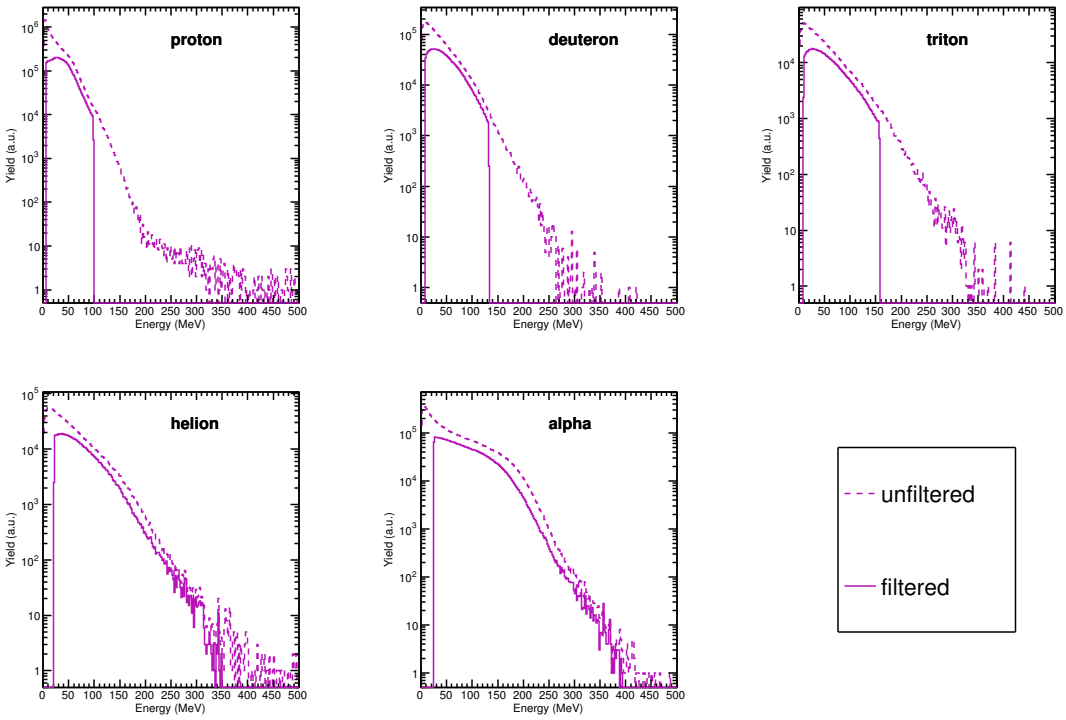

Figure 4.2: Energy in the lab from the HIPSE event generator. These are for Ca+Ni at 40 MeV/nucleon, full statistics (unfiltered) and light charged particles cut on FAUST geometry and energy range (filtered).

proton spectrum the Ca+Ni overtakes the Ar+Fe in yield around 40 MeV and crosses back down to lower yield near 80 MeV. This effect is also in the predictions of the HIPSE event generator. Figure 4.3 shows the energy spectra for all protons that meet the filter requirements to be detected by the FAUST for all four systems from HIPSE.

The pBUU transport model code was also used to simulate the heavy ion collisions. In pBUU, the form of the density dependence of the asymmetry energy was varied, and the predictions of these various calculations were compared to the experimental correlation functions. For the two Ar+Fe systems, three impact parameters (2, 5, and 8 fm) and "impact parameter weighted" proton energy spectra are shown in figure 4.4. The impact parameter weighted figure weights the distributions according to the quantum mechanical cross-section ($\sigma_\ell = \pi\lambda\!\!\!^{-2}(2\ell + 1)$), where $\lambda\!\!\!^{-}$ is the de Broglie wavelength of the projectile. The weights for each impact parameter for the two

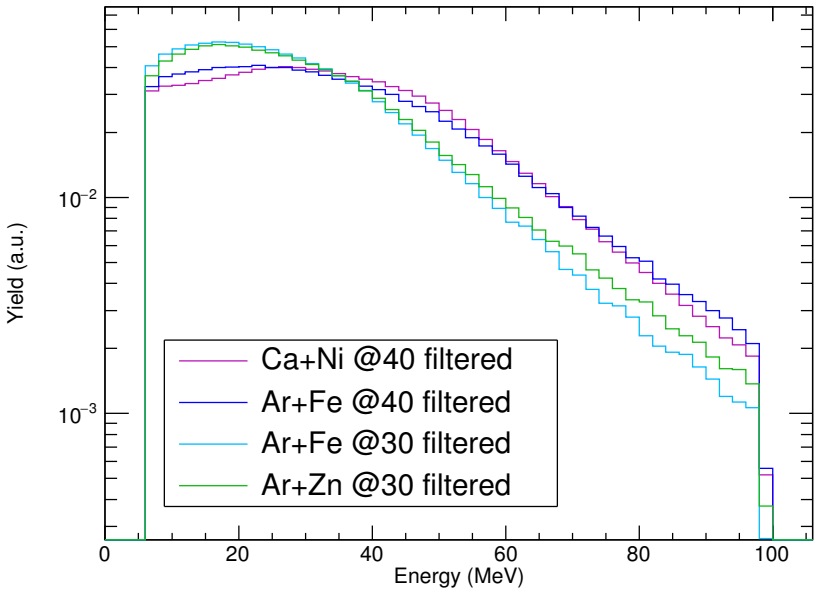

Figure 4.3: Energy spectra for protons from HIPSE for all four systems. The relative behavior of the 40 MeV/nucleon systems is very similar to the protons shown in figure 4.1, and bestows further confidence upon the calibration.

beam energies are shown in Table 4.1. As in the experimental data and HIPSE above, the spectra are basically the same shape, although the lower energy system (cyan) is shifted to slightly lower energies than the higher energy beam (blue). These spectra are drawn normalized on a log scale for shape comparison. The unfiltered (dashed lines) spectra are peaked near 20 MeV and decrease in yield by a decade near 100 MeV in the b=2 fm panel. This is consistent with the HIPSE simulation shown in figure 4.2, but less steep than the two decade difference over the same range in energy in the experimental spectra shown in figure 4.1. As the impact parameter increases, there is less damping, and the yield at higher energies in the lab increases. The energy spectra for the 40 MeV/nucleon Ar beam are shifted higher in energy than the 30 MeV/nucleon beam. The filtered (full lines) for the same systems and impact parameters are also shown. The energy cut on expected FAUST detection removes some of the data at very low lab energy; this affects the shape of the distribution for the b=8 fm calculation most strongly.

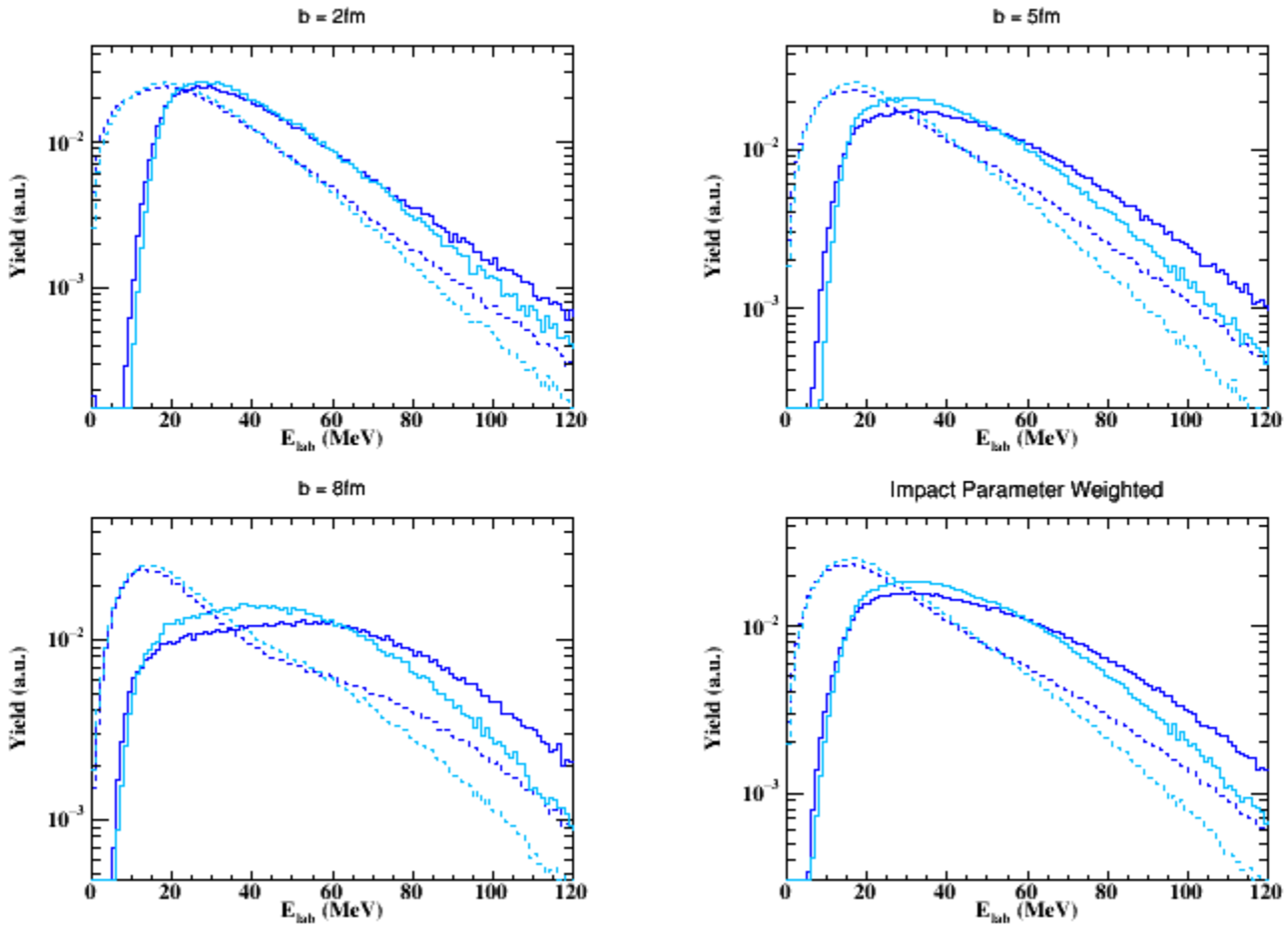

Figure 4.4: Energy spectra for protons resultant from BUU for four different impact parameters (b), drawn normalized. Blue is Ar+Fe at 40 MeV/nucleon, cyan is Ar+Fe at 30 MeV/nucleon. Dashed lines are all of the protons formed in BUU and used for the correlation function, full lines are geometry and energy cut for FAUST acceptance.

b (fm)	^{40}Ar at 40 MeV/A Weight	^{40}Ar at 30 MeV/A Weight
2	0.133297	0.133329
5	0.333333	0.333287
8	0.533370	0.533384

Table 4.1: Weights of contribution of each impact parameter to "impact parameter weighted" proton spectra in figure 4.4.

4.1.1 Velocity Distributions

The velocity of the alphas in the beam direction ($v_{||}$) vs the perpendicular to the beam ($v_{\perp}$) are plotted in units of c in figure 4.5. There are three distinct bands angled with respect to both axes

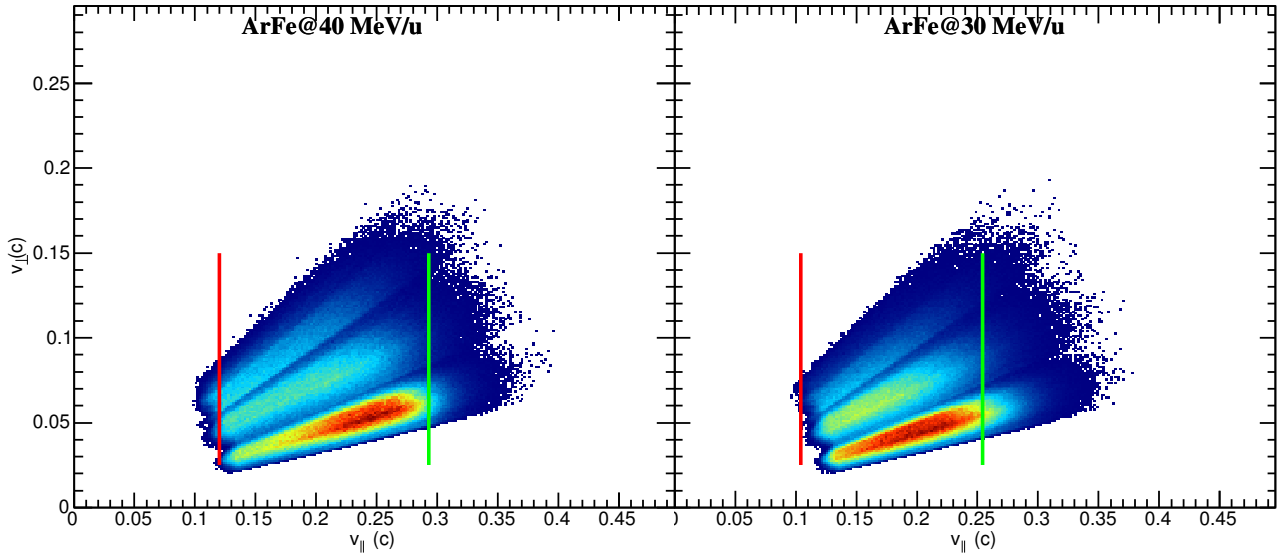

Figure 4.5: Experimental $v_\perp$ vs $v_\parallel$ for alphas. The three bands in each of the plots correspond to the rings of FAUST which are considered for this current data set. Left plot: Ar+F at 40 MeV/nucleon. Right plot: Ar+Fe at 30 MeV/nucleon. Red line: system center of mass velocity. Green line: Beam velocity.

which correspond to the three rings of FAUST which were used in this analysis (from lowest to highest transverse velocity, Rings C, D, and E). The maximum of the parallel velocity decreases with increasing θ of the detector. The beam velocity is indicated on figures 4.5 and 4.7 by the green line. The center of mass of the target-projectile system is indicated on figures 4.5 and 4.7 by the red line. The velocity distribution for the 40 MeV/u Ca+Ni (not shown) system strongly resembles that of the 40 MeV/u Ar+Fe system; similarly, the 30 MeV/u Ar+Zn (not shown) resembles that of 30 MeV/u Ar+Fe.

The parallel vs perpendicular velocity for alpha particles produced by HIPSE event generator are shown in figure 4.6. The top panel shows the unfiltered events, all of the alphas produced by HIPSE. The target source is near 0 c on the left, the projectile source is near 0.27c, and a Coulomb ring is visible around each of them. These two sources are clearly separated in parallel velocity, but there is significant overlap and emission from the mid-velocity source. The bottom panel shows

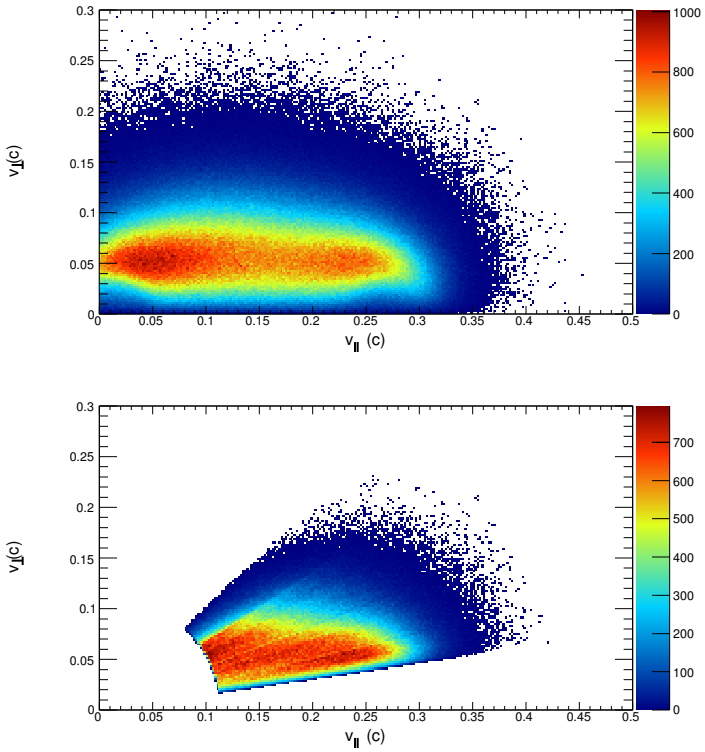

Figure 4.6: HIPSE-generated $v_\perp$ vs $v_\parallel$ for alphas for the Ca+Ni at 40 MeV/nucleon system. Top panel: all alphas produced by HIPSE. Bottom panel: only alphas which hit a FAUST detector in the appropriate energy range.

alphas which pass the FAUST filter. The geometry and energy thresholds of FAUST select for alphas from the projectile and mid-velocity sources. The maximum of the 2D alpha distribution in ring C (the lowest in perpendicular velocity) is in a similar spot as the maximum in figure 4.5.

Figure 4.7 shows experimentally measured $v_\parallel$ vs $v_\perp$ for protons. The three bands correspond to the Rings C, D, and E of FAUST. The corner detectors of FAUST show up as small distinct bands in between the rings, and are more obvious for the protons, which are more spread out in velocity along the beam axis. The protons which are emitted at 0.22c for the 40 MeV/nucleon beam and 0.21c for the 30 MeV/nucleon beam are likely emitted in the PLF frame, which can be clearly seen as the Coulomb ring in the protons from HIPSE shown in the top panel of figure 4.8.

The parallel vs perpendicular velocity for protons produced by HIPSE event generator are shown in figure 4.8. The distributions from HIPSE show that the different sources of alphas (fig.

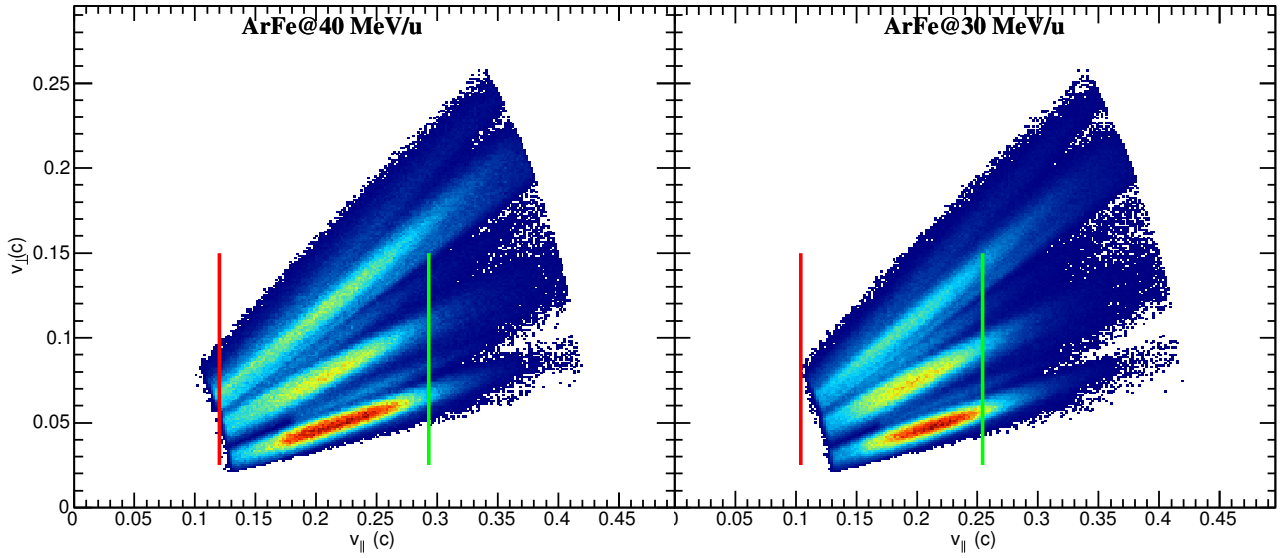

Figure 4.7: Experimental $v_\perp$ vs $v_\parallel$ for protons. The three bands in each of the plots correspond to the rings of FAUST which are considered for this current data set. Red line: system center of mass velocity. Green line: Beam velocity.

4.6) are not as well separated in parallel velocity as the protons (fig. 4.8). This is due to more significant contribution of alpha emission from the mid-velocity source in HIPSE. In the bottom panels of those same figures, the PLF* source is still clearly visible in velocity space after the FAUST geometry and energy cuts to the velocity distributions. The maximum of the distribution in ring C (the lowest in perpendicular velocity) from HIPSE is in a similar spot as the experimental data. There is still some contribution from mid-velocity sources.

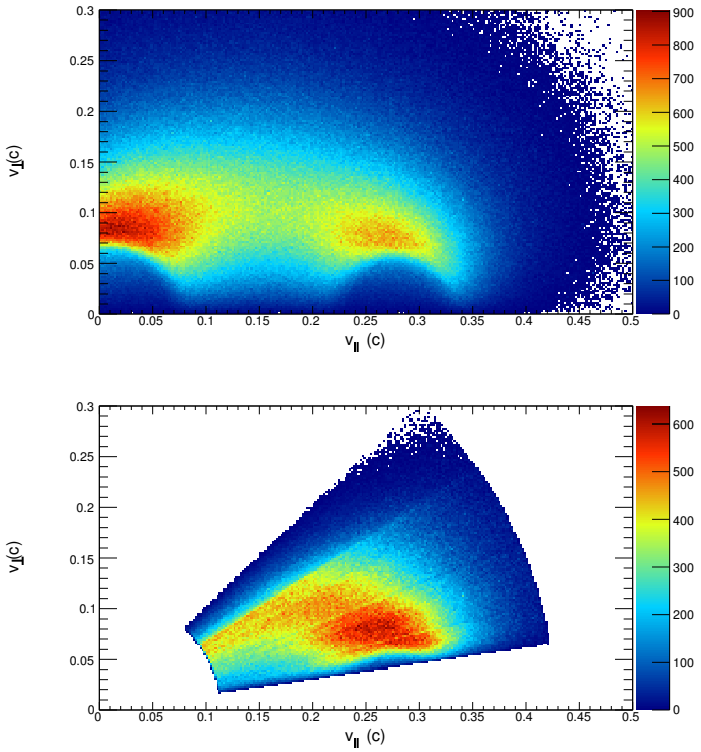

Figure 4.8: HIPSE-generated $v_{\perp}$ vs $v_{||}$ for protons for the Ca+Ni at 40 MeV/nucleon system. Top panel: all alphas produced by HIPSE. Bottom panel: only protons which hit FAUST detectors in the appropriate energy range.

4.2 Light charged particle correlation functions

Correlation functions can be used to measure resonant states [34]. These states can either be produced through the direct emission of an unstable nucleus from an excited source (e.g. ^{8}Be), or from sequentially emitted particles interacting (proton-proton attractive s-wave interaction). The appearance of known resonances in correlation functions can be used as an indicator that calibration of the detection apparatus is accurate. Known states can be found at [53]. The following correlation functions have been extracted from the experimental data using the event-mixing technique without any further cuts to the data than the identification, position determination and energy assignment from the calibration to determine the momentum of all light charged particles. All four systems are shown in each figure (see legend) unless otherwise indicated.

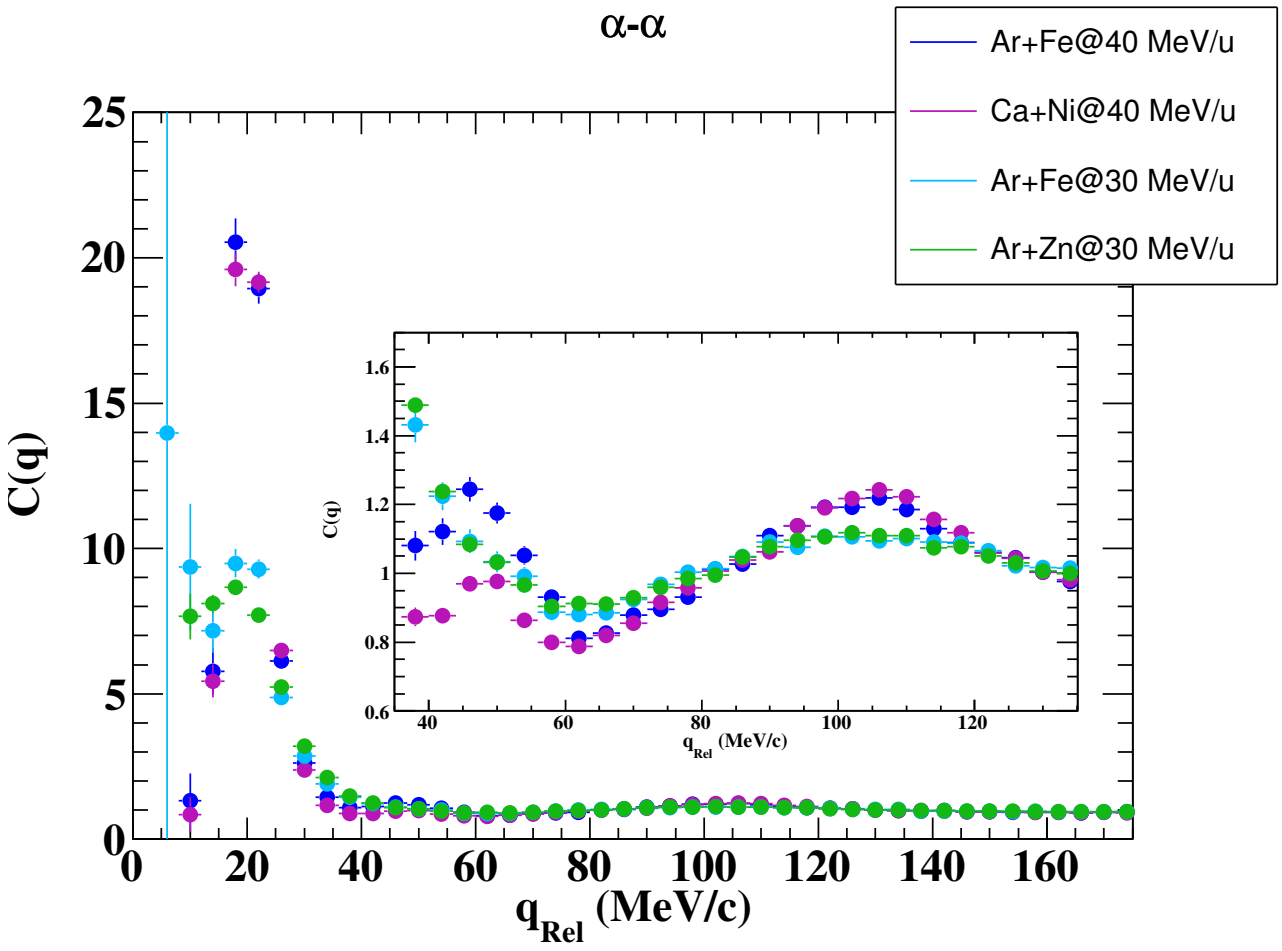

Figure 4.9: Alpha-alpha correlation functions for all systems. The inset is a zoomed in snapshot of the larger canvas.

The alpha-alpha correlation function is shown in figure 4.9. The unstable ground state of ^{8}Be appears as the large resonance around 20 MeV/c. The resonances in cyan and green (30 MeV/nucleon Ar beam) are much lower than for the blue and purple 40 MeV/nucleon beams. The 40 MeV/nucleon systems also have a clear resonance (from the 2.43 MeV state of ^{9}Be, with the concurrent emission of a neutron) near 45 MeV/c, shown in more detail in the inset of figure 4.9. The 30 MeV/nucleon systems do not display this resonance. The lower energy system may not have sufficient excitation energy on average to excite that state often. Resonance of the 3.04 MeV excited state of ^{8}Be is also present near 105 MeV/c. This resonance is more pronounced for the 40 MeV/nucleon beams, which have a similarly sized resonance. The 30 MeV/nucleon beams have

a less pronounced peak for this state, also. The location of these peaks conforms to expectations. This is an indication that the alpha particle calibration is accurate.

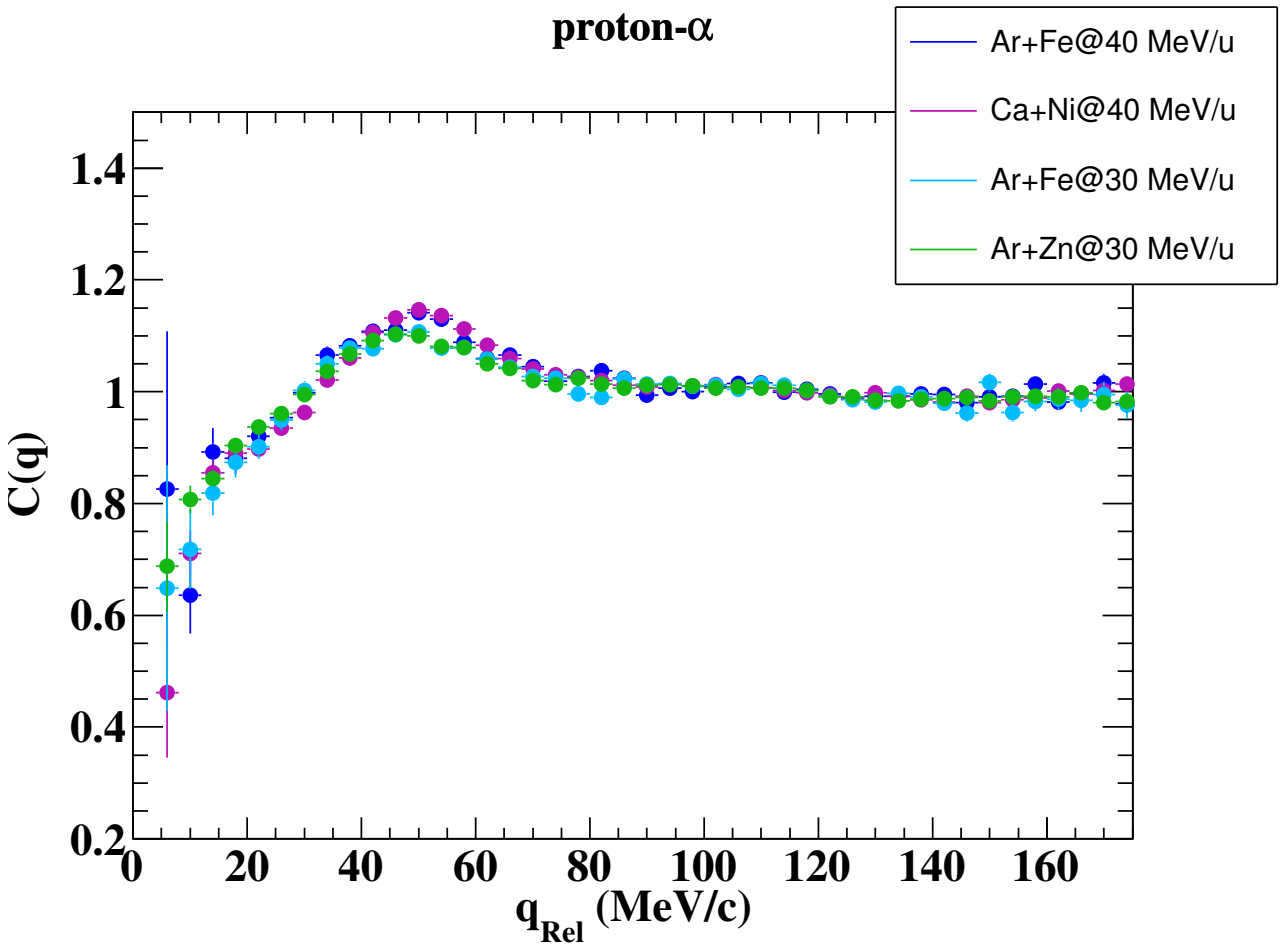

Figure 4.10: Proton-alpha correlation functions measured for all systems.

The particles of particular interest for this dissertation are the protons. The alphas are behaving appropriately, so the correlation function between protons and alphas can be examined as a check on the assignment of proton momenta. Proton-alpha correlation functions result from ^{5}Li and are shown in figure 4.10. The broad peak near 50 MeV/c is from the ground state of ^{5}Li. This resonance is seen in all four systems, while large q_{Rel} evens out at C(q)=1. The green and cyan (30 MeV/u beams) also populate this ground state of ^{5}Li. This characteristic behavior indicates that

the proton calibration is also accurate. In reference [34] and elsewhere, a peak from ^{9}B is seen near q=10 MeV/c for a 60 MeV/nucleon beam. The systems shown are at lower energy (possibly populating the ^{9}B state less) and the detection apparatus does not allow for double hits in a FAUST telescope, so no peak around q_{Rel}=10 MeV/c is observed.

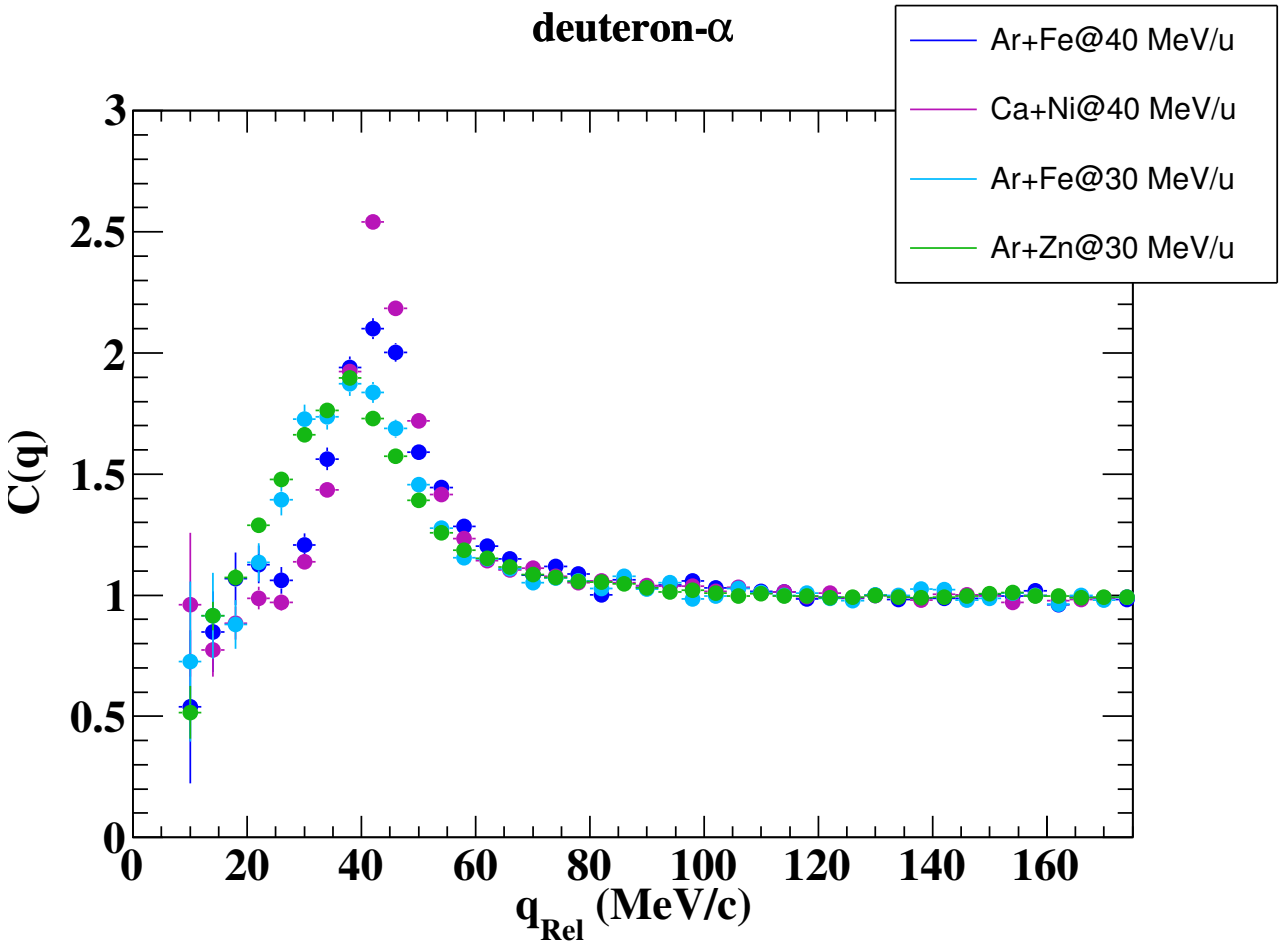

Figure 4.11: Deuteron-alpha correlation functions measured for all systems.

Deuteron-alpha correlation functions were also extracted and are shown in figure 4.11. All spectra are normalized at high q_{Rel}. There is a resonance around 45 MeV/c for the 40 MeV/nucleon beams, which is indicative of the 2.186 MeV excited state of ^{6}Li. This is the dominant resonance for the deuteron-alpha interaction. There is also a small resonance near 20 MeV/c, which is ob-

served in [34]. The lower energy argon beams (cyan and green) exhibit a peak shifted lower in q_{Rel}, near 40 MeV/c. This may indicate that there are slightly different sources from which the t-α particles originate at the two beam energies. Or it could be that the CsI calibration for Z=1 beyond the range of proton energies is somewhat inaccurate.

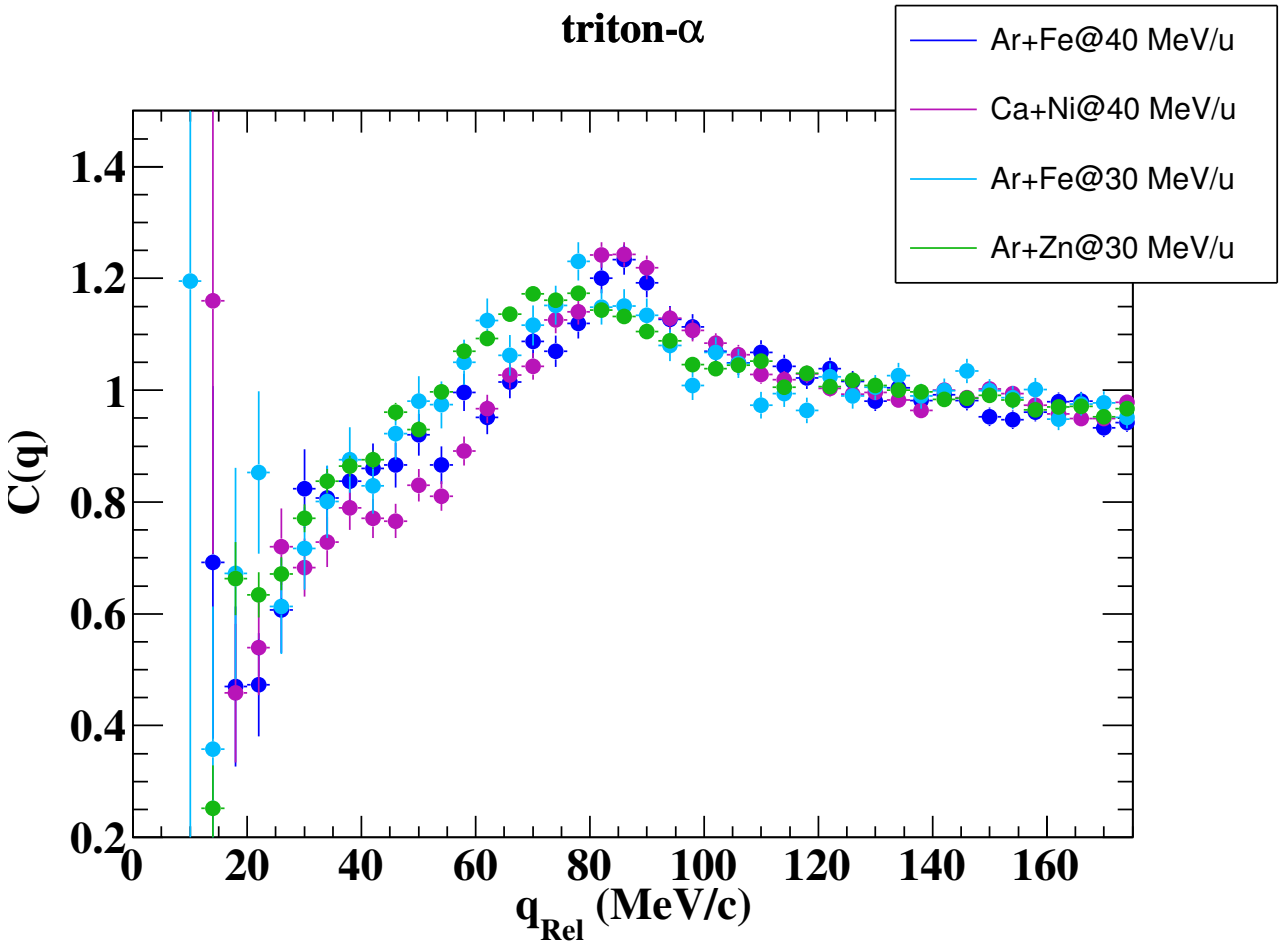

Figure 4.12: Triton-alpha correlation functions measured for all systems.

Experimental triton-alpha correlation functions for all of the systems are shown in figure 4.12, which results from the decay of the ^{7}Li nucleus. This interaction is dominated by the 4.63 MeV excited state of ^{7}Li, which is near 80 MeV/c for the blue and purple 40 MeV/nucleon beams. As observed in the deuteron-alpha correlation functions above, for similar reasons, the 30 MeV/nucleon

beams seem to have a resonance at a slightly lower energy than the 40 MeV/nucleon beams.

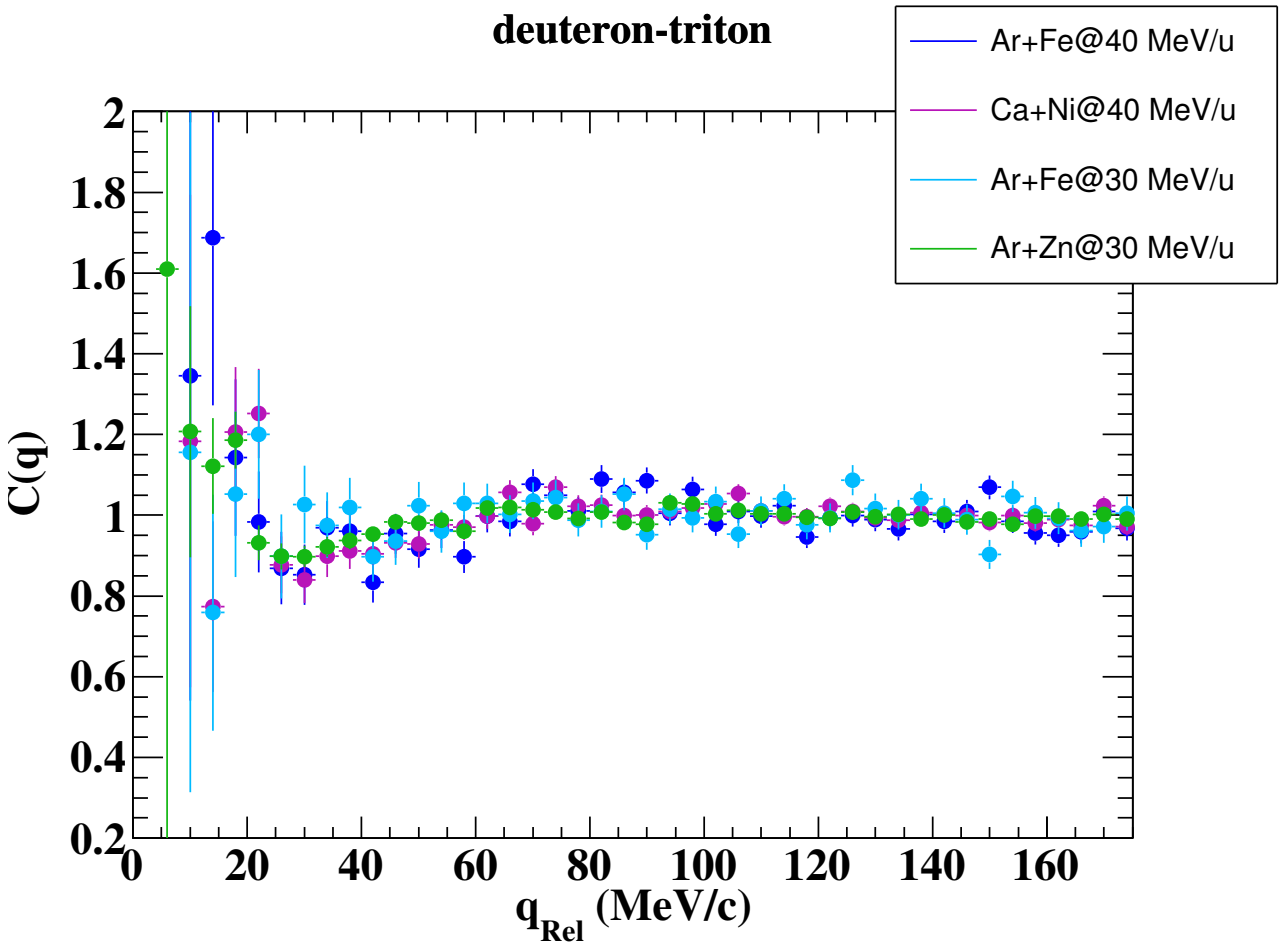

Figure 4.13: Deuteron-triton correlation functions measured for all systems.

Deuteron-triton correlation functions are shown in figure 4.13. Deuteron-triton interactions are dominated by the resonant states of ^{5}He. The characteristic levels of ^{5}He are found near 30 MeV/c (16.76 MeV state) and 80 MeV/c (19.8 MeV state). The 19.8 MeV state can be seen in the correlation functions from the 40 MeV/nucleon beams (blue and purple). As with figure 4.12, the 30 MeV/nucleon beams (cyan and green) display a resonance that is approximately 10 MeV/c lower in relative momentum space than the 40 MeV/nucleon beams. As has been seen for earlier resonances, the 40 MeV/nucleon systems show an enhancement near 20 MeV/c which is much

greater than the 30 MeV/nucleon systems.

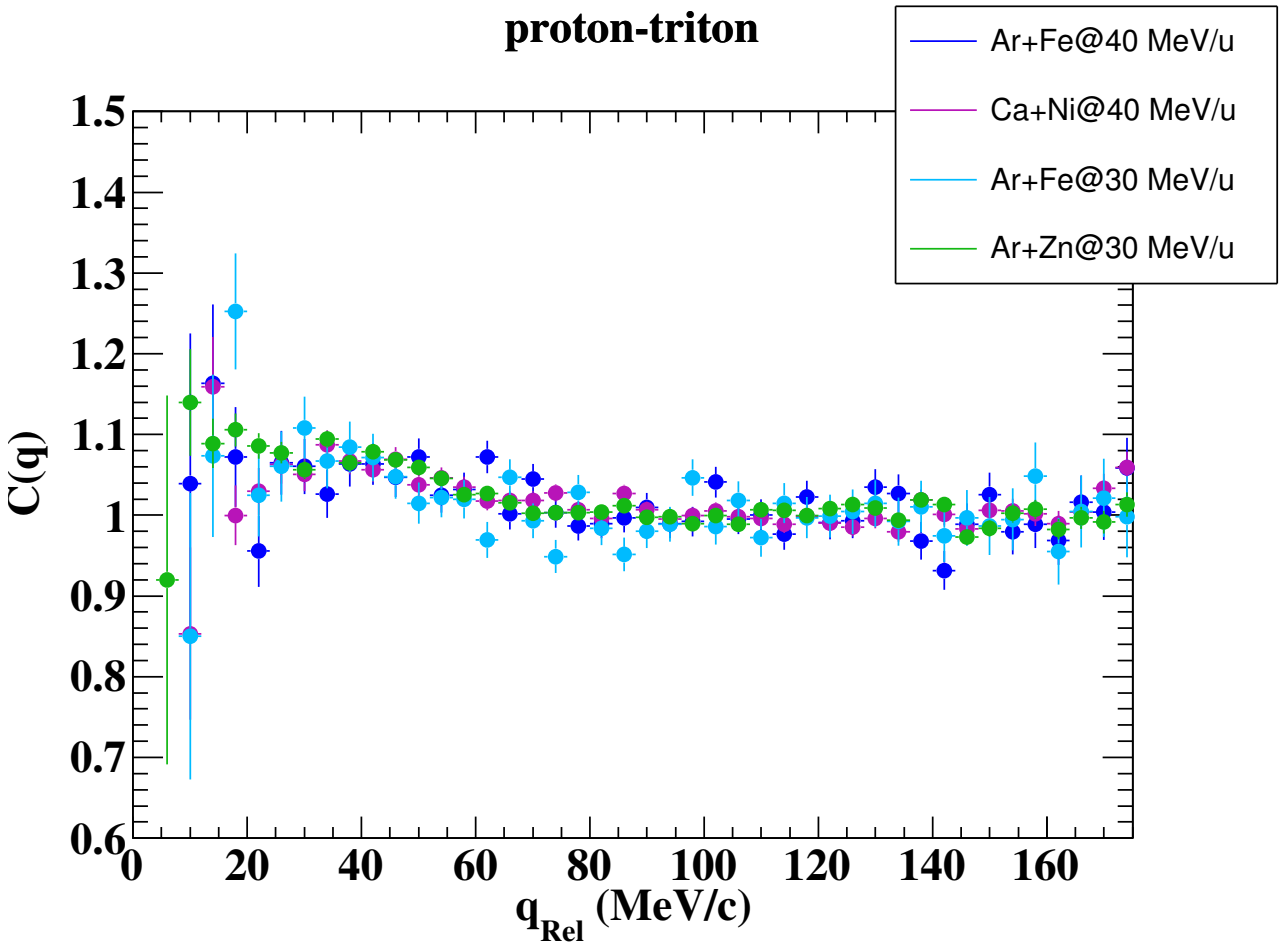

Figure 4.14: Proton-triton correlation functions measured for all systems.

Proton-triton correlation functions are shown in figure 4.14. These resonances come from unstable states in ^{4}He. The structure near 15 MeV/c comes from the 20.1 MeV state, while the broad structure around 45 MeV/c comes from 21.1 and 22.1 MeV states from ^{4}He. The resonances are stronger for the 40 MeV/nucleon beams and are in the correct places, providing yet another check on the overall momentum calibration of the protons measured in this experiment.

4.3 Proton-proton correlation functions

Proton-proton correlation functions, as discussed in section 1.3, have a structure dependent upon the fundamental interactions between protons. Correlation functions have been extracted from the protons measured in this experiment in an analogous way to the light charged particle correlation functions discussed in section 4.2. The resultant correlation functions are shown in figure 4.15. The dashed line at C(q)=1 is included for reference. All of the systems show anti-correlation below 20 MeV/c, but no real characteristic s-wave interaction peak at 20 MeV/c is yet visible. The protons in the pp correlation function may have been emitted from the excited projectile-like fragment or from the mid-velocity source. In order to examine protons from a source of well-defined space-time extent, it is helpful to select on protons emitted early in the interaction and protons emitted from violent collisions. Both are investigated in this analysis.

Impact parameter is a useful quantity for event characterization, but is not directly accessible from experimental data. Transverse energy has been shown to be correlated with violence of the collision. Using the HIPSE event generator, ref [54] has shown a correlation between impact parameter and total transverse energy of the particles produced in the event. Figure 4.16 uses the impact parameter input to HIPSE and the transverse energy from only Z<3 particles to calculate an experimental surrogate that tracks with impact parameter in the method of reference [54]. While anything below approximately 4 fm is indistinguishable, fine binning on the impact parameter is not necessary. Merely a rough cut on the total violence of the collision is sufficient for our purposes. Figure 4.16 shows that distinguishing between central and peripheral collisions is possible via this method. Below, a cut on the transverse momentum of the event is used to select violent collisions.

Transverse energy of light charged particles in the event correlates with impact parameter, so the transverse momentum of the event does, too. The distribution of transverse momentum of the event for proton pairs in figure 4.15 is shown in the left panel of figure 4.17. This impact parameter surrogate is strongly peaked at 200 MeV/c with a broad shoulder starting near 400 MeV/c and a high momentum tail that extends out to 800 MeV/c. Besides selecting events of greatest violence, proton-proton correlation functions are strongest when created using protons emitted earliest in

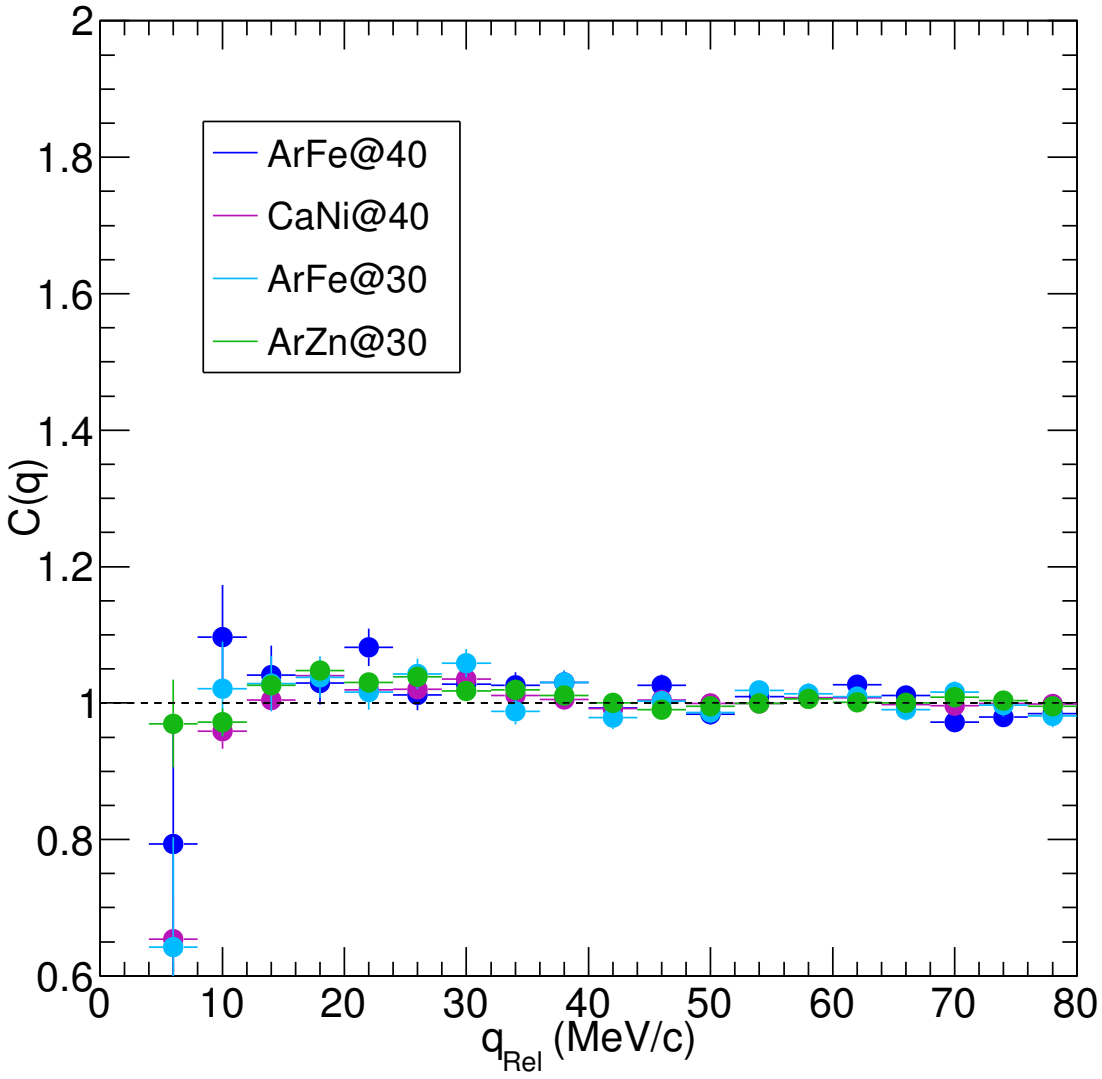

Figure 4.15: Plain proton-proton correlation function.

the event. One experimentally viable and theoretically motivated method of doing this is to select protons with high momentum of the pair [26, 42, 11]. The right panel of figure 4.17 shows the distribution of event transverse momentum vs the total momentum of the proton pair in the frame of the center of mass of the system. These distributions are shown for all four systems. There is a maximum in the distribution at low p_{Pair} and low event transverse momentum. There is a diagonal

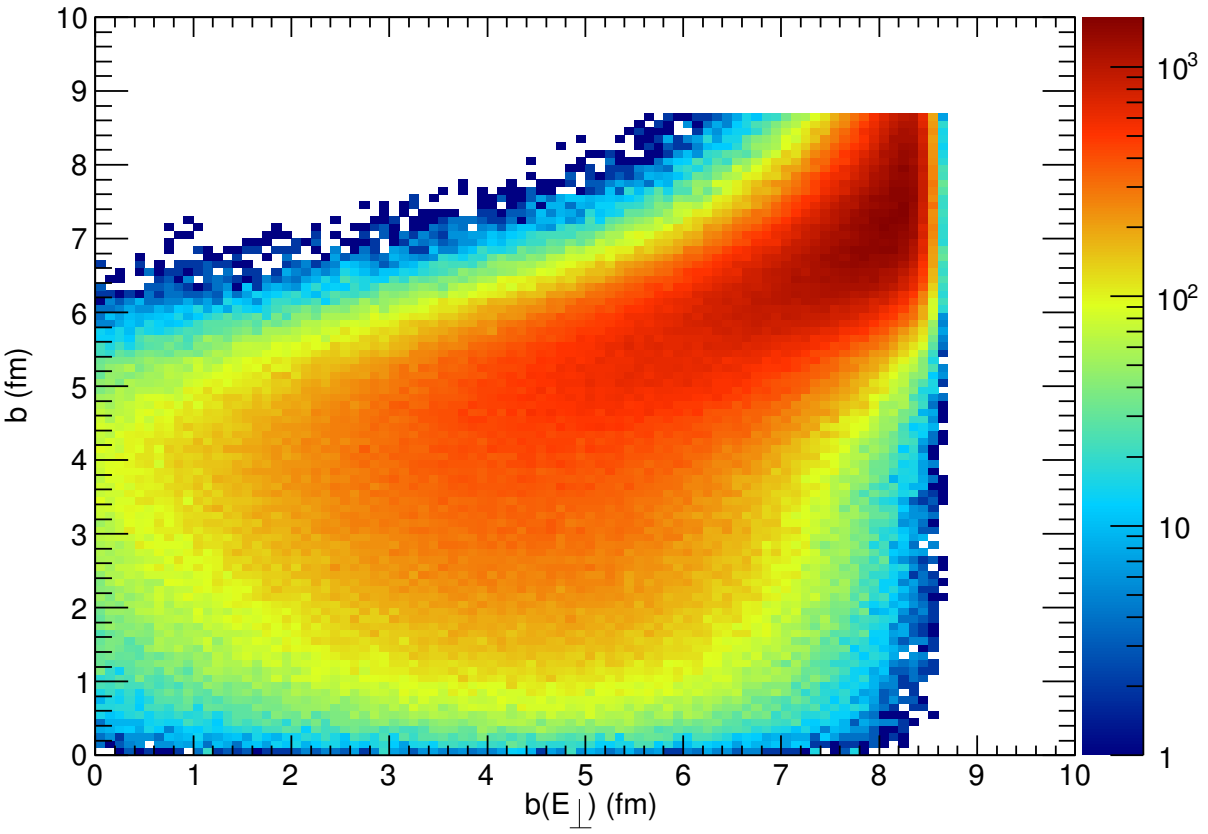

Figure 4.16: Impact parameter vs impact parameter calculated from event transverse energy for HIPSE events, following the method of [54].

slash that continues up and to the right, and then a broad distribution in transverse momentum of the event. The center of mass of the system frame was chosen in order to select for the earliest protons emitted from the hottest part of the system, the mid-velocity source.

The correlation function was extracted with a selection on one of five increasingly severe cuts in transverse momentum of the event and one of three increasingly severe cuts in the total momentum of the proton pair in the center of mass of the system frame. The resultant correlation functions are shown in figure 4.18 for the Ar+Zn and Ar+Fe at 30 MeV/nucleon systems. The top left plot is the two lower energy systems from figure 4.15, with no cuts on the momentum of the proton pair or the transverse momentum of the event. The correlation functions from left to right are cut

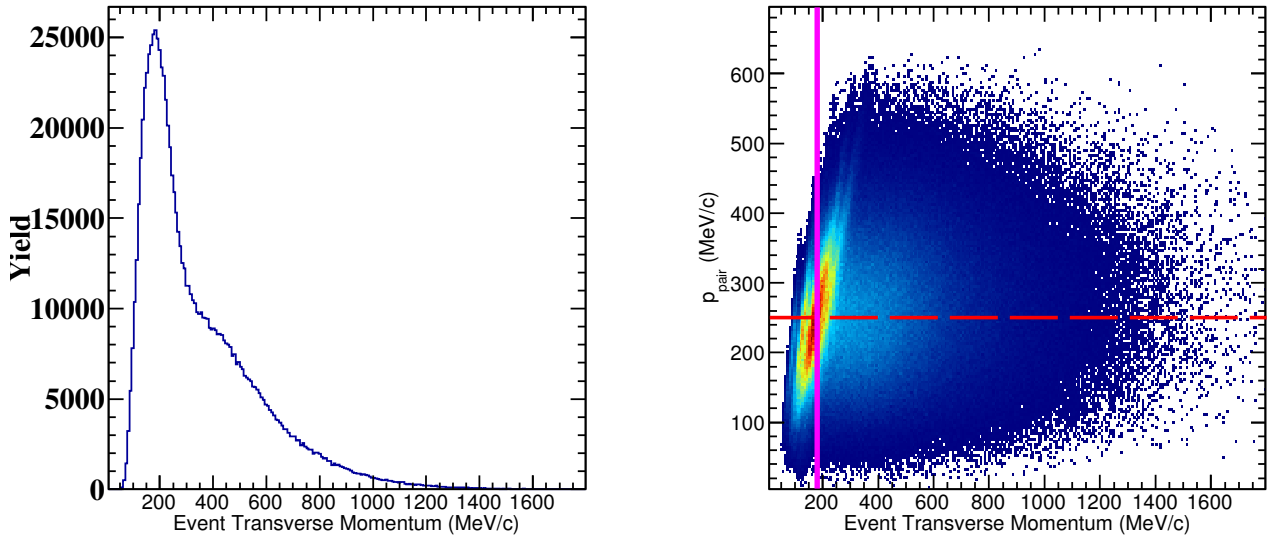

Figure 4.17: Ca+Ni at 40 MeV/u. Left panel: distribution of event transverse momentum. Right panel: total momentum of each proton pair in the system center of mass frame vs the transverse momentum of the event containing the protons.

on increasing transverse momentum of the event, from the leftmost column, which contains no cut through 140, 180, 220, 260 and 300 MeV/c in event transverse momentum. Preferentially selecting events which are, on average, increasing in violence of collision brings out the characteristic anti-correlation at low q_{Rel}.

Moving from top to bottom in the figure increases momentum of the proton pair in the center of mass of the system, moving from no cut to 250 to 300 to 350 MeV/c. As the protons included in the correlation function are selected to be emitted earlier, the correlation peak at 20 MeV/c increases in size. The same cuts are applied to the 40 MeV/nucleon beams in figure 4.19. The trends in behavior of the correlation functions are the same with increasing violence and earliness of emission cuts. Note that regardless of the cuts applied the Ar+Fe systems have consistently stronger correlation functions than both the Ca+Ni and the Ar+Zn systems at 40 and 30 MeV/nucleon, respectively.

When choosing which cuts to examine more carefully, it is advantageous to select on the earliest emitted protons and the most central collisions possible. But this must be balanced with the

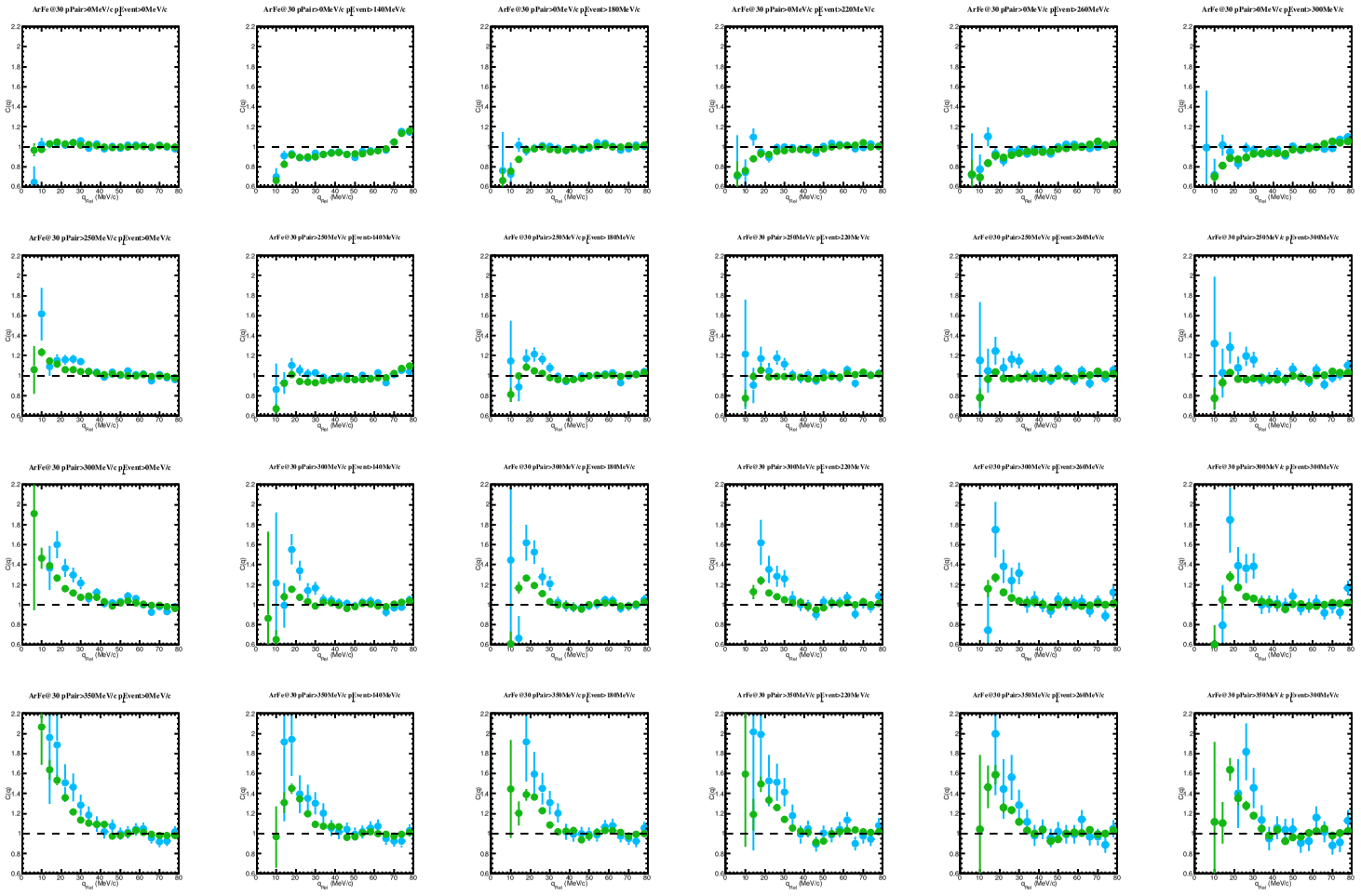

Figure 4.18: Correlation Functions for Ar+Fe (cyan) and Ar+Zn (green) at 30 MeV/nucleon, cut on proton pair total momentum (early emitted protons) and transverse momentum of events (violence of collision).

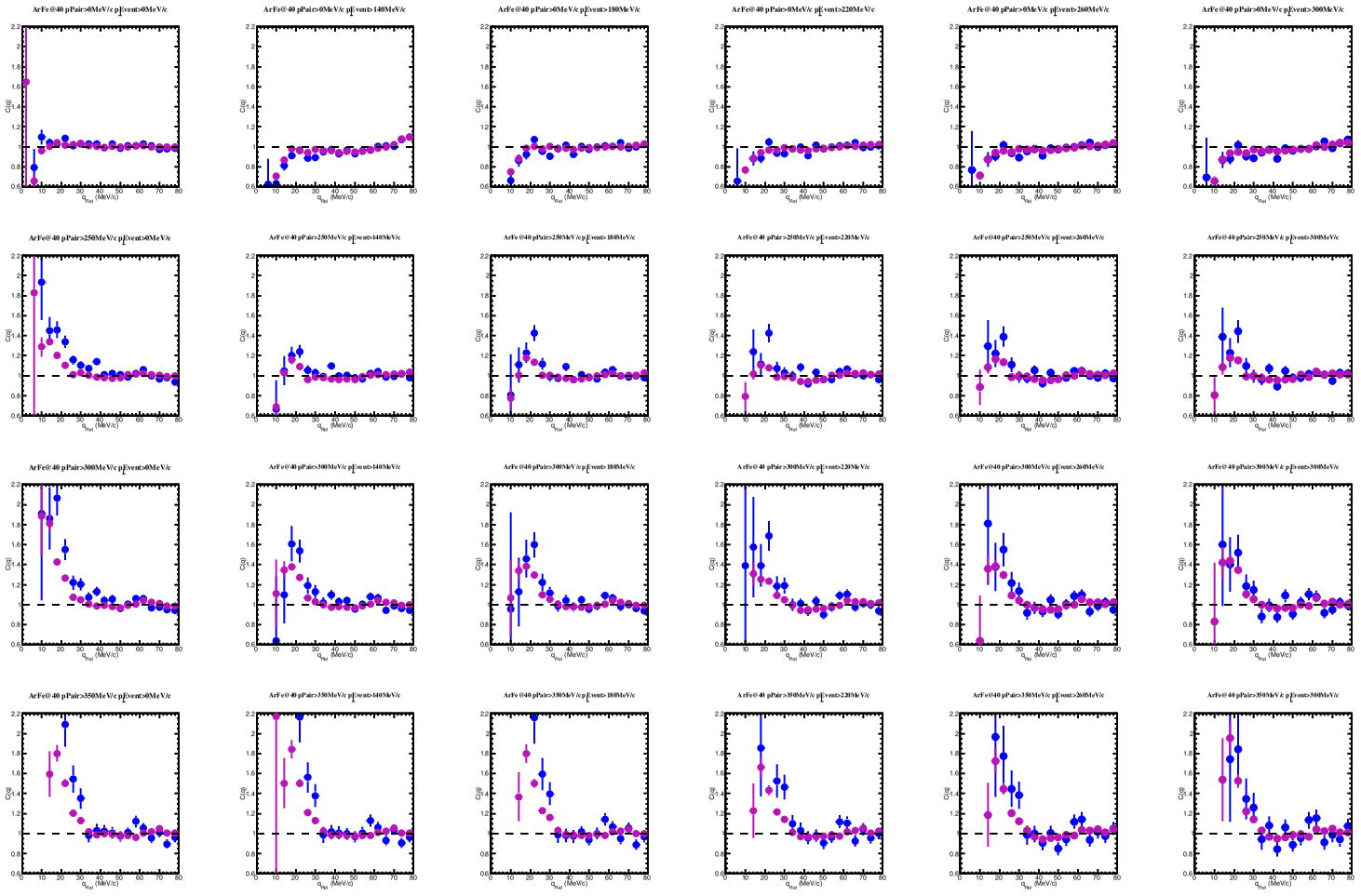

Figure 4.19: Correlation Functions for Ca+Ni (purple) and Ar+Fe (blue) at 40 MeV/nucleon, cut on proton pair total momentum (early emitted protons) and transverse momentum of events (violence of collision).

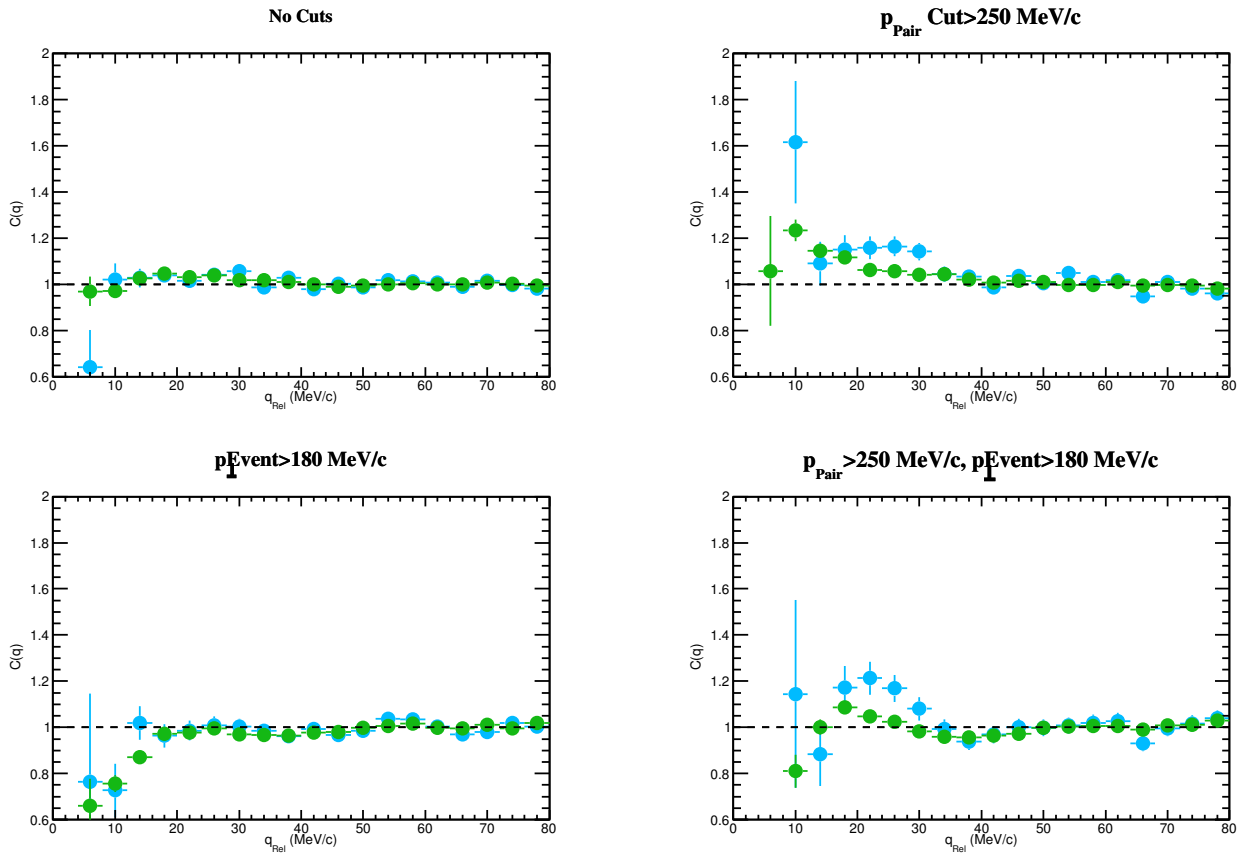

Figure 4.20: Proton-proton correlation functions for 30 MeV/nucleon systems (Ar+Zn green, Ar+Fe cyan) featuring chosen cuts on the early momentum of the proton pair (250 MeV/c) and the violence of the collision (180 MeV/c). Both of the cuts are necessary in order to draw out the proton-proton interaction peak.

need for statistics, particularly at low q_{Rel}, where the proton-proton resonance is. The cuts which maximize statistics at low q_{Rel} and show the greatest resonance in the correlation function across all four systems are shown on figure 4.17 as the vertical solid magenta line (event transverse momentum > 180 MeV/c) and the horizontal dashed red line (proton pair momentum > 250 MeV/c).

The upper left panels of figures 4.20 and 4.21 are figure 4.15 reproduced for reference. In the lower left panel, the effect of a transverse momentum cut is shown, which alone is not enough to draw out the peak in the correlation function. As is shown in the upper right panels of figures 4.20 and 4.21, a cut only on the total momentum of the proton pair results in early emitted protons which are not constrained in phase space to be from similar events. A event transverse momentum

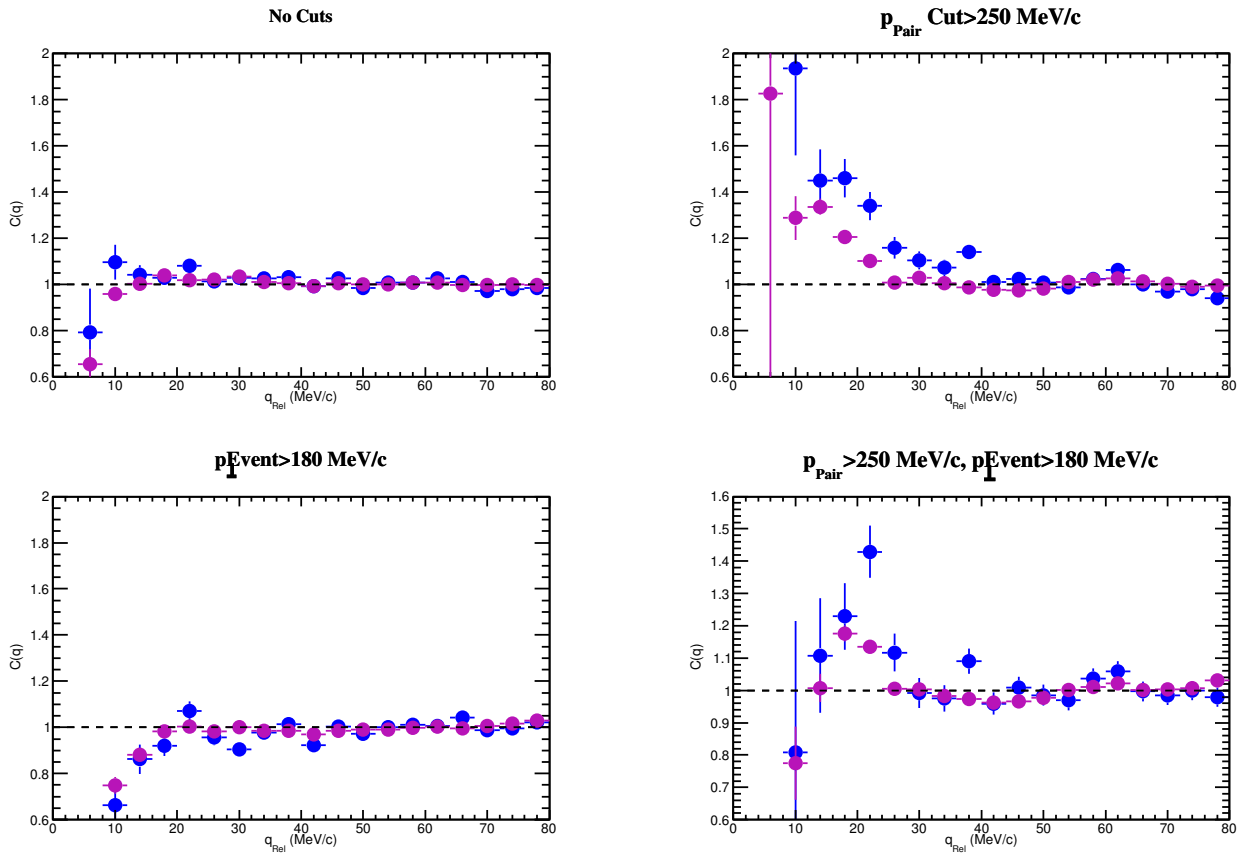

Figure 4.21: Proton-proton correlation functions for 40 MeV/nucleon systems (Ca+Ni purple, Ar+Fe blue) featuring chosen cuts on the early momentum of the proton pair (250 MeV/c) and the violence of the collision (180 MeV/c). Both of the cuts are necessary in order to draw out the proton-proton interaction peak.

cut preferentially selects violent events and enhances the characteristic anti-correlation at low q_{Rel} as expected. This produces the plot in the lower right panel.

The event-mixing method involves extracting measured yield and mixed yield proton pairs which make up the numerator and denominator of the correlation function in figures 4.20 and 4.21 according to equation 1.4. These numerators and denominators are shown in figure 4.22. Aside from below q_{Rel}=20 MeV/c, the numerator (filled) and denominator (open) are nearly identical on the upper left "No Cuts" panel. The upper right panel has an increasing distance between the numerator and denominator moving from right to left, which results in a very high correlation function at very low q_{Rel}. The lower left panel resembles the upper left very closely, and results

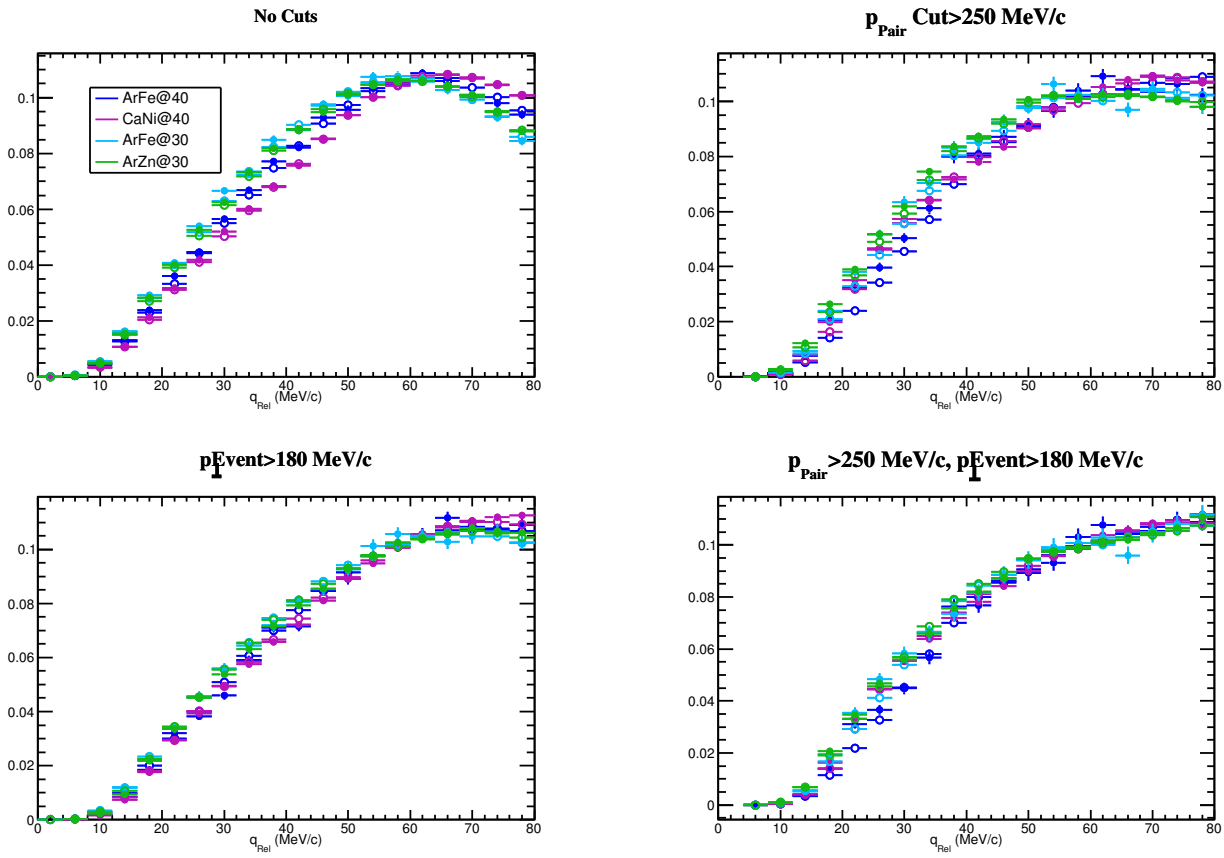

Figure 4.22: Scaled measured yield numerators (filled) and mixed yield denominators (open) for corresponding panels of figures 4.20 and 4.21.

in a very similar correlation function. There is more of a difference between the numerator and denominator in the area of interest near 20 MeV/c, which results in the peak in the correlation function. These correlation functions can be compared to the predictions of a transport model calculation.

4.4 Comparison of experimental data to transport model

4.4.1 pBUU description and parameters

Correlation functions have been shown to be sensitive to the asymmetry energy of the nEOS in theoretical models due to emission timescale effects [30]. Because it is not possible to vary this term of the nEOS in experiment, it is helpful to compare experimental data to simulations

which contain this parameter and can reproduce experimentally observable characteristics. For correlation functions at these energies, comparisons are often to a transport model, which describes the early stages of reactions well [42, 55].

Boltzmann-Uehling-Uhlenbeck (BUU) transport models like pBUU, developed by Danielewicz and described in [56, 57, 58] use the BUU transport equation (a modified Boltzmann equation shown explicitly in equation 1.6 of reference [42] first used to describe gases in ref [59]). Transport models solve a semi-classical equation classically using test particles to approximate a mean field. In the pBUU model, at the beginning of the calculation (0 fm/c) the heavy ions involved are nearly touching, beginning the collision. A reduced nucleon-nucleon cross-section (the effects of which have been studied [42, 50]) is used to account for Pauli blocking and higher order effects. The observables of interest from the transport model for each test particle are the time of the last nucleon-nucleon collision, as well as the position, momenta, and local density at that time. This information is used to generate a source function, looking at the density of protons which were involved in a nucleon-nucleon collision. This information is turned into a source function via the anstice code developed by B. Barker [60]. This source function is then combined with a proton-proton interaction in momentum space kernel (K(q) described briefly in section 1.3) via the spCoral code [60] to extract a proton-proton correlation function.

The parameters that were chosen for the pBUU run in this project were: 400 test particles/nucleon, Rostock in-medium cross-section, run length: 300 fm/c, soft mean field compressibility (K=210 MeV), and clusters created (A<4). Three values of γ (0.33, 1.0, 2.0) were used. The parametrization asymmetry energy in this version of pBUU, described more fully in chapter 3 of reference [61], is:

$$E_{asy} = S_{kin}\left(\frac{\rho}{\rho_0}\right)^{(2/3)} + S_{int}\left(\frac{\rho}{\rho_0}\right)^{\gamma}, \tag{4.1}$$

where the kinetic part of the asymmetry energy, from Fermi motion of the test particles is S_{kin}=12.5 MeV and the interaction asymmetry energy, S_{int} ~19 MeV, which adds up to an asymmetry energy of ~31 MeV at saturation density. The values of the asymmetry energy in the model for this study as a function of density are shown in figure 4.23. There is a quite wide range from a very soft

parametrization to a quite stiff one.

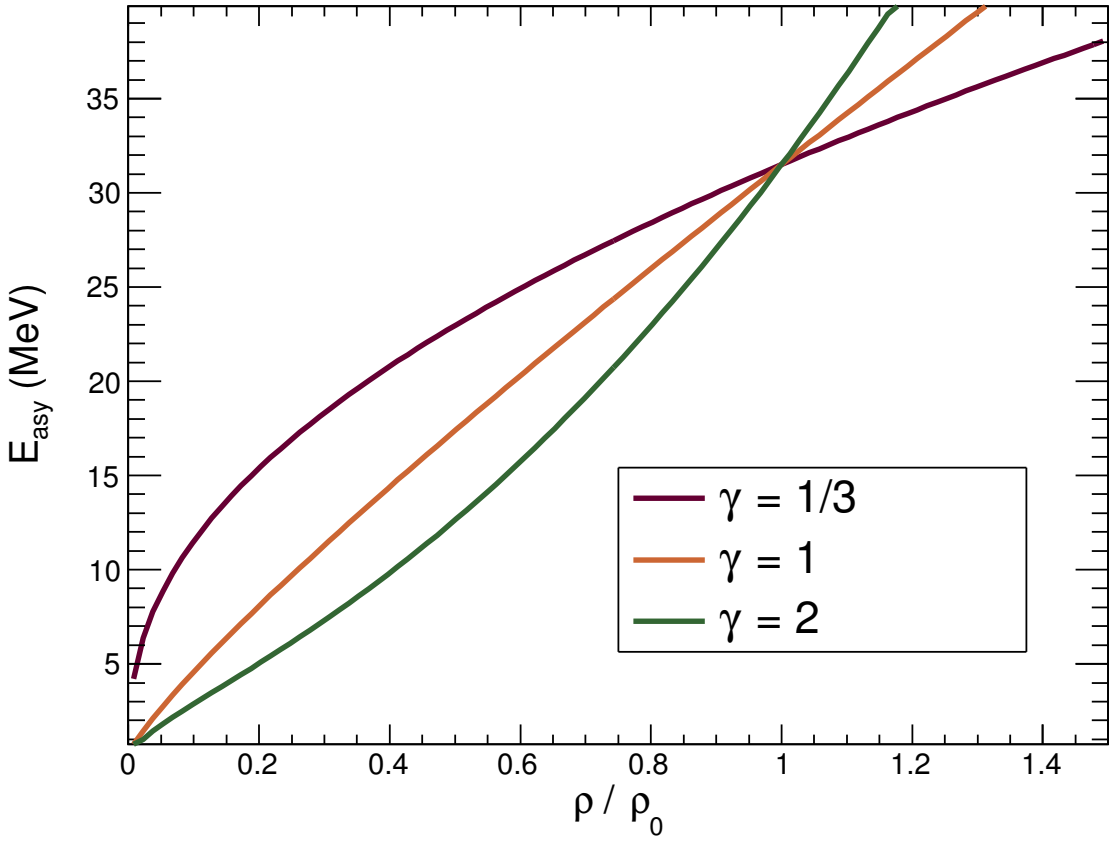

Figure 4.23: Comparison of γ from pBUU, according to equation 4.4.1.

4.4.2 Correlation functions from pBUU

In order to compare the transport simulation with the experimental data, it is important to first understand the effect of the detection apparatus on the observables of interest. Figure 4.24 shows correlation functions extracted from pBUU for Ca+Ni at 40 MeV/nucleon for all protons involved in a nucleon-nucleon collision, run with the $\gamma = 1$ parametrization of the asymmetry energy. The gray lines are for all protons emitted. Dashed lines are for the raw output from pBUU, full lines are for pBUU that has gone through a FAUST geometry and energy cut. The gray corelation

functions are very similar and do not have a very strong correlation peak at 20 MeV/c. In red are shown correlation functions for protons which are emitted "early" in the reaction. That is, their last nucleon-nucleon collision occured before 100 fm/c. These early protons show a much stronger correlation function, although the FAUST filter does not make a large difference in the strength of the correlation. The FAUST filter actually slightly increases the correlation, possibly by removing contributions from the target-like source. The rest of the pBUU shown in this dissertation will have the FAUST filter applied.

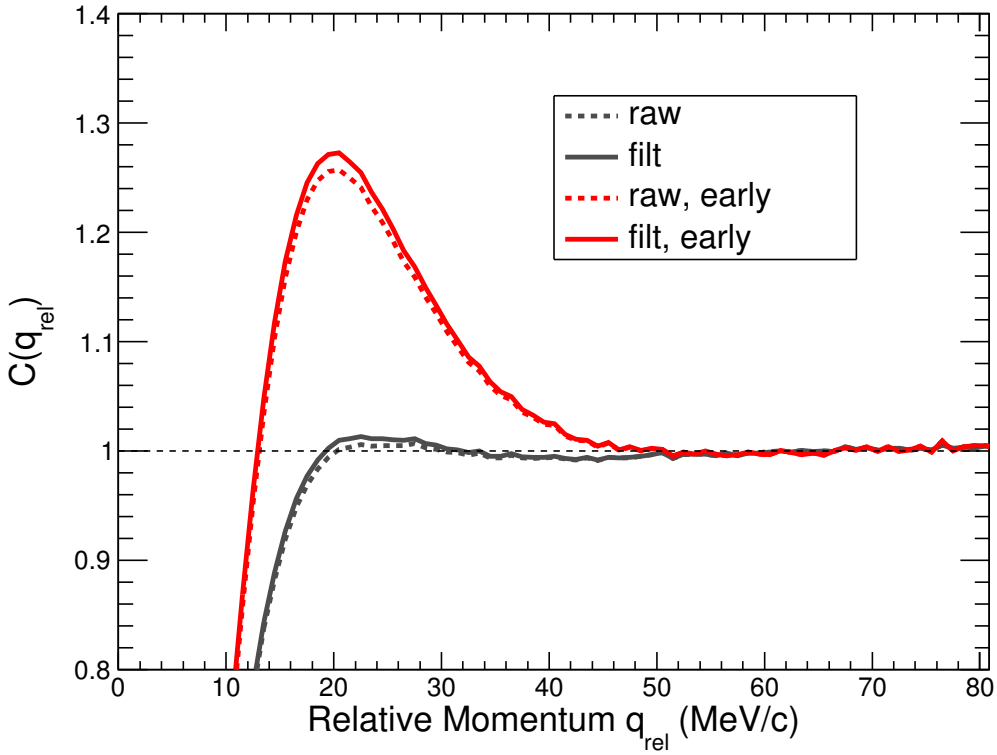

Figure 4.24: Correlation functions extracted from pBUU for Ca+Ni at 40 MeV/nucleon, γ=1. The gray lines are all particles which had a nucleon-nucleon interaction. The red lines are only particles which participated in their last nucleon-nucleon collision before 100 fm/c. "Filt" refers to the FAUST filter in geometry and energy.

It is desirable to select protons emitted early in the reaction in the pBUU as well as in the

experimental data in order to have the most correlated protons. In the pBUU, there is the option to simply select protons emitted early in the reaction to be included in the correlation function, as mentioned above. A selection for earlier emitted protons can also be done in a way analogous to the experimental data by cutting on the total momentum of the proton pair in the center of mass frame. These two cuts are applied to the pBUU in order to select for protons emitted early in the event. The resultant correlation functions are shown in figure 4.25. The gray uncut correlation function is shown for reference, as well as the line at C(q)=1. The pink correlation function has a cut on the total momentum of the proton pairs above 350 MeV/c. This cut was chosen slightly higher than the experimental cut because the momentum distributions from pBUU are slightly higher than the experimental distributions. The strength of the correlation function is increased by this cut, so earlier proton emission is being selected on average. However, it is not nearly as strong a correlation as the protons emitted before 100 fm/c, shown in red. In order to pull out the largest effect, this early cut is used for the remainder of the analysis.

Another interesting aspect of the transport model is the ability to select on impact parameter and observe how the violence of the collision affects the observables. From pBUU, correlation functions were extracted from the Ca+Ni at 40 MeV/nucleon system for b_{imp}=2, 5, and 8 fm. The resultant correlation functions for "early" emitted protons are shown in figure 4.26. Perhaps somewhat surprisingly, the most central collision, b_{imp}=2 fm exhibits the lowest correlation function, shown in red. As the impact parameter increases to 5 (green) and 8 (blue), the correlation function increases in strength and width, which is indicative of a smaller emitting source.

Some insight into why the more central impact parameters appear to have a larger source according to pBUU can be found in the density profiles resultant from the code at time steps 27 fm/c apart, shown for each impact parameter in figures 4.27, 4.28, and 4.29. For the most central collision, b=2 fm, the projectile and target overlap nearly completely, creating a relatively large region from which protons are rapidly ejected.

As the impact parameter increases to 5 fm in figure 4.28 and 8 fm in figure 4.29, the projectile-like source (right region of greater density) is more separated from the target-like source (region

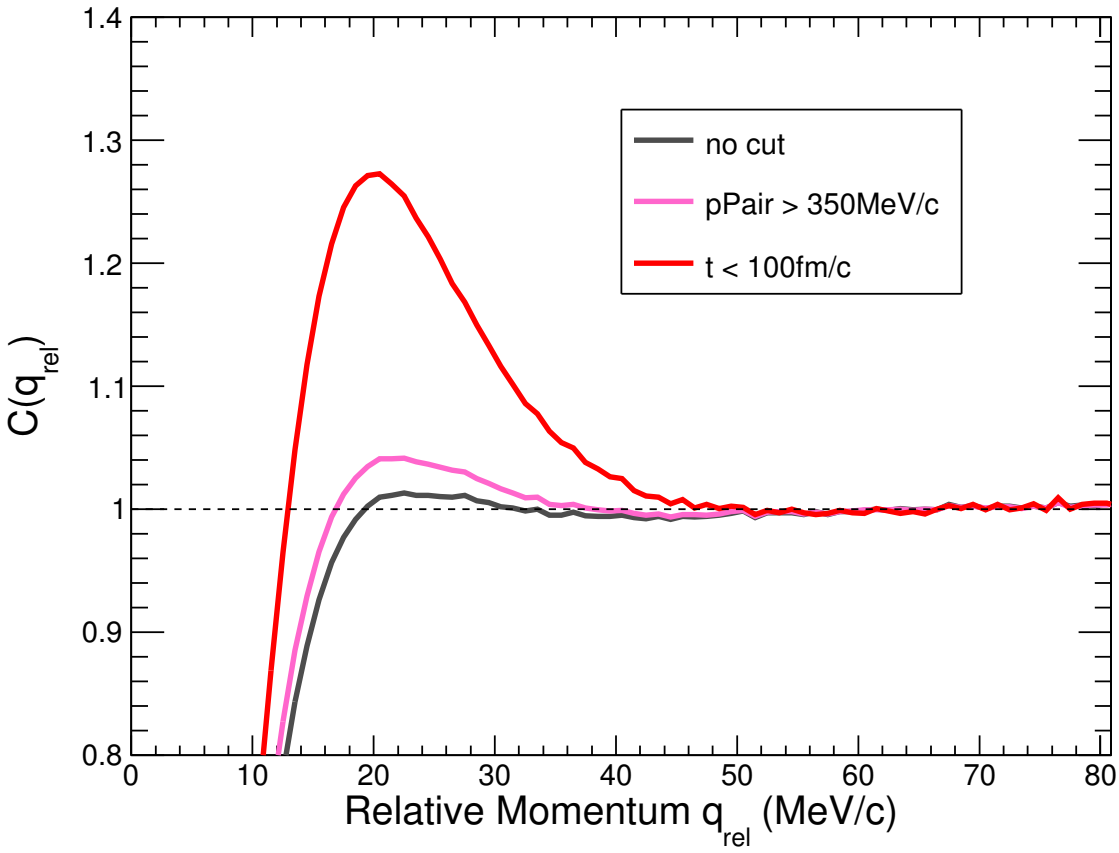

Figure 4.25: Correlation functions extracted from pBUU for Ca+Ni at 40 MeV/nucleon, γ=1. The gray correlation function includes all particles which had a nucleon-nucleon reaction. The pink correlation function has a high sum of momentum of the proton pair above 350 MeV/c, analogous to the experimental cut in figure 4.20. The red correlation function shows only particles which had their last nucleon-nucleon reaction before 100 fm/c.

of greater density on the left) at the time of the early emission of the protons in the 5th panel from the left on the top row. Fewer nucleons in the overlap zone implies a smaller mid-velocity source which leads to a larger peak in the correlation function.

The 2 fm impact parameter was chosen to compare the relative strengths of the correlation functions between the systems at different parametrizations of the asymmetry energy. In pBUU, the asymmetry energy is changed as the γ parameter in equation 4.4.1. Three different parameters were used in running the pBUU for this project. The above simulations were run at $\gamma = 1$, a stiff parametrization of the density-dependence of the asymmetry energy.

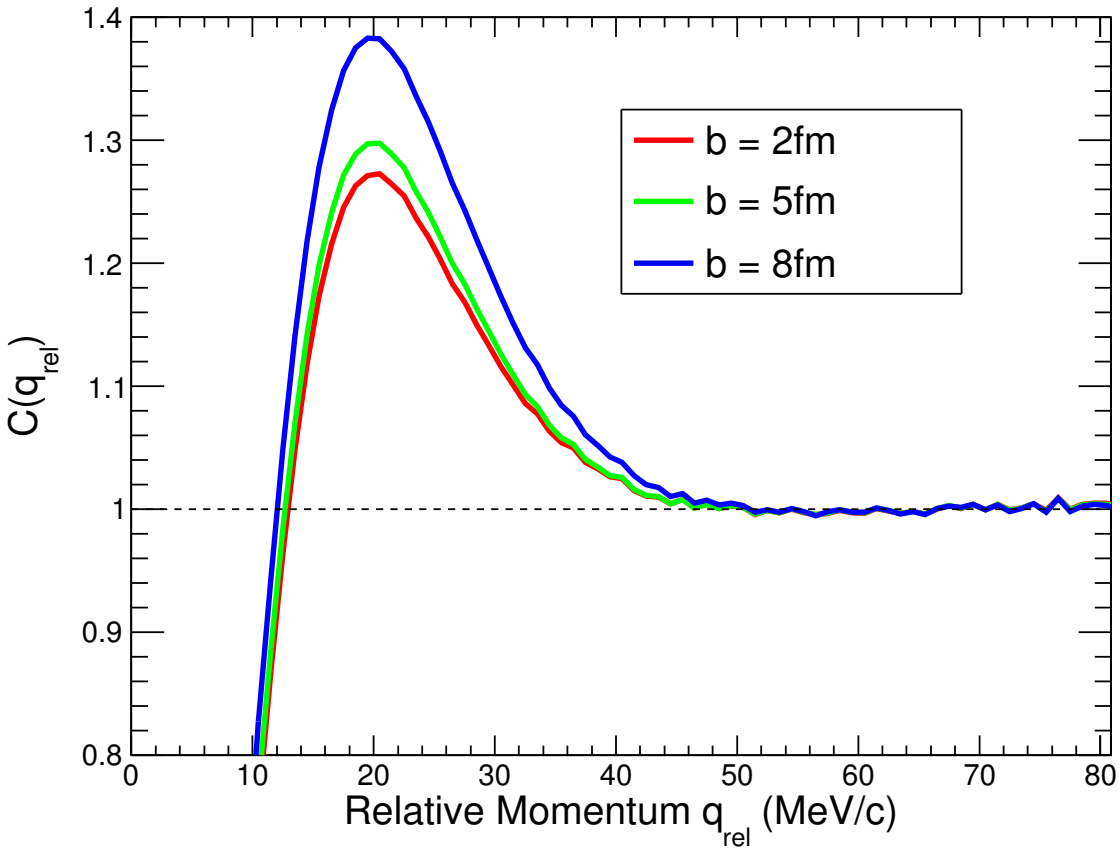

Figure 4.26: Correlation functions extracted from protons emitted "early" from pBUU for Ca+Ni at 40 MeV/nucleon, γ=1 for three different impact parameters (b).

Figure 4.30 shows correlation functions extracted for the 30 MeV/nucleon systems from the pBUU. For all values of γ shown in figure 4.30 the less neutron-rich system, Ar+Fe, shows a stronger correlation function than the Ar+Zn in pBUU. This ordering matches the experimental data in the left most panel of figure 4.31. This ordering is consistent with previous results, that systems with smaller total numbers of nucleons produce more highly peaked correlation functions.

All of the parametrizations of the asymmetry energy show stronger correlation functions for the 40 MeV/nucleon Ar+Fe system than the 30 MeV/nucleon Ar+Fe system, as demonstrated in figure 4.32. The 40 MeV/nucleon system emits protons which are moving more quickly (from a hotter source). These more energetic protons tend to be emitted earlier in the event. So it is expected that

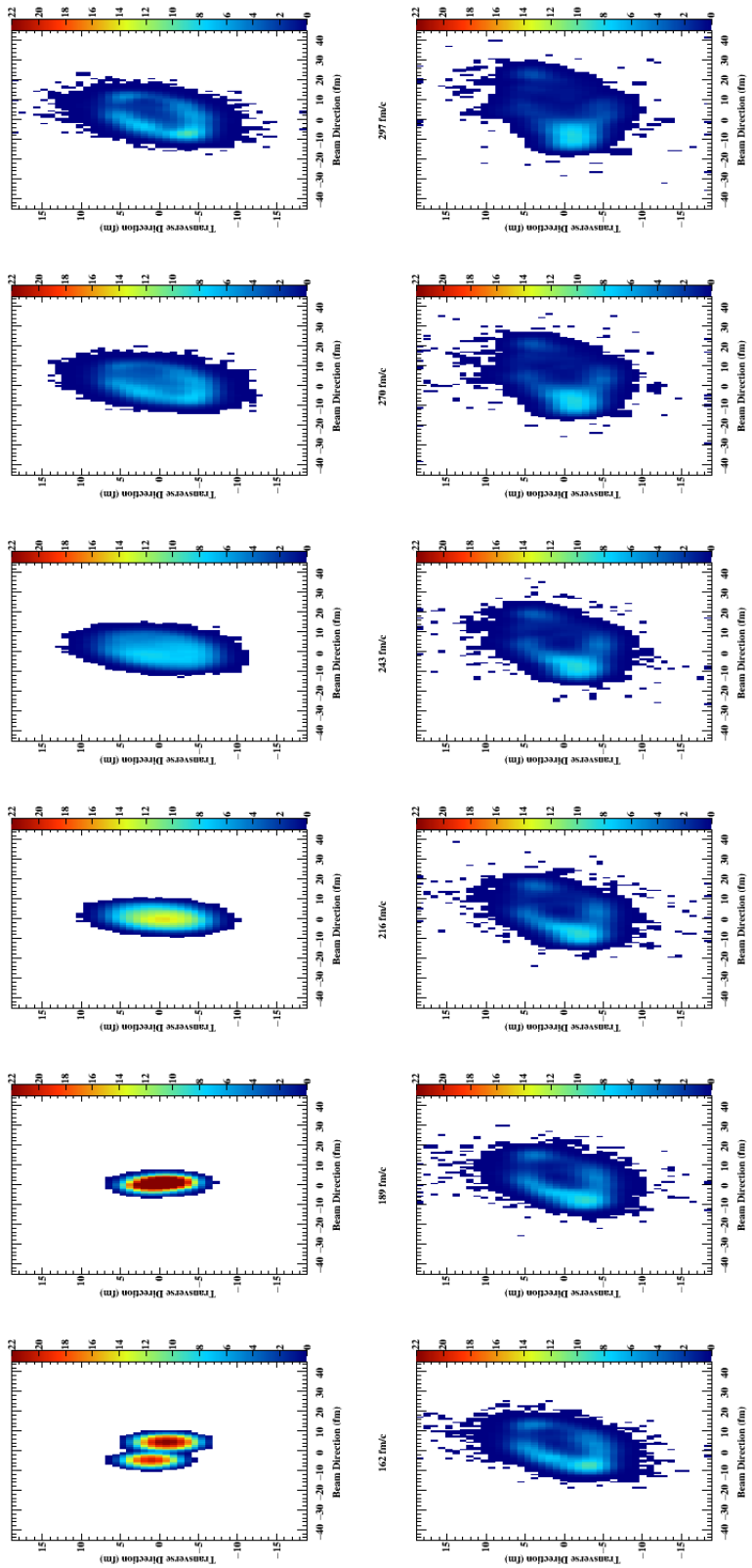

Figure 4.27: Density profile of representative 2 fm collision of Ar+Fe at 40MeV/nucleon in pBUU at time steps of 27 fm/c. "Early" protons are emitted by 5th panel from the left on the top row.

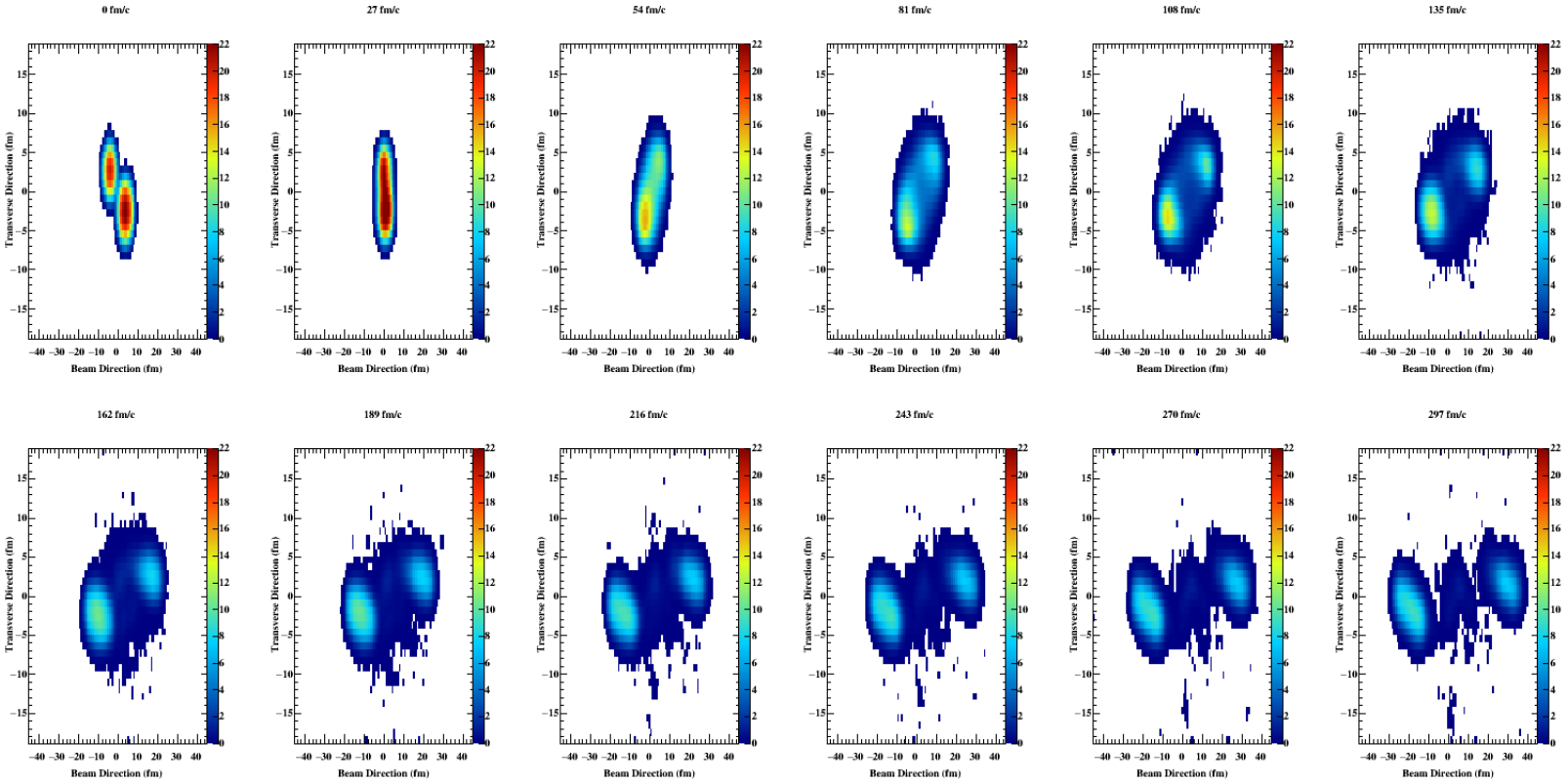

Figure 4.28: Density profile of representative 5 fm collision of Ar+Fe at 40MeV/nucleon in pBUU at time steps of 27 fm/c. "Early" protons are emitted by 5th panel from the left on the top row.

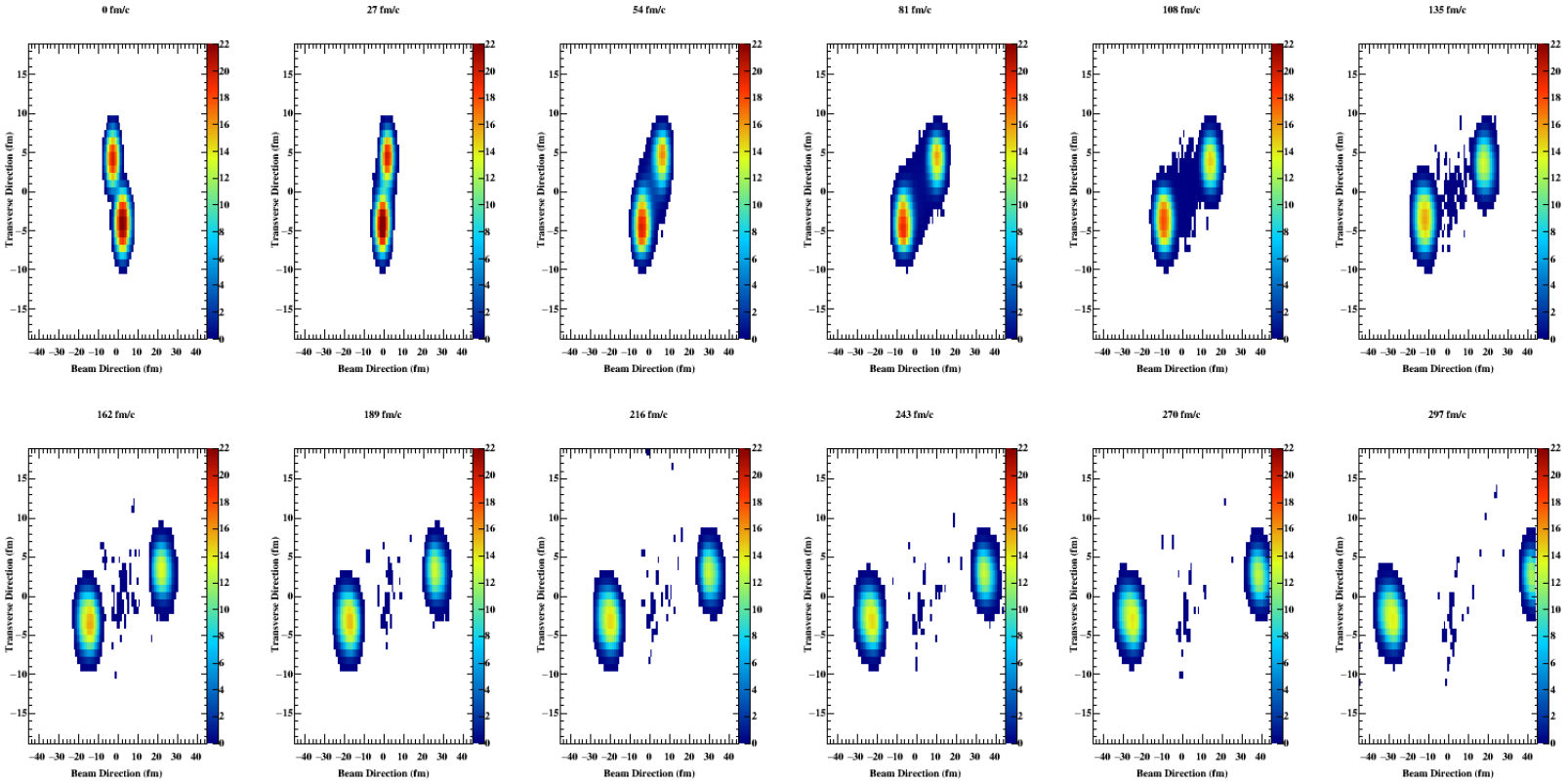

Figure 4.29: Density profile of representative 8 fm collision of Ar+Fe at 40MeV/nucleon in pBUU at time steps of 27 fm/c. "Early" protons are emitted by 5th panel from the left on the top row.

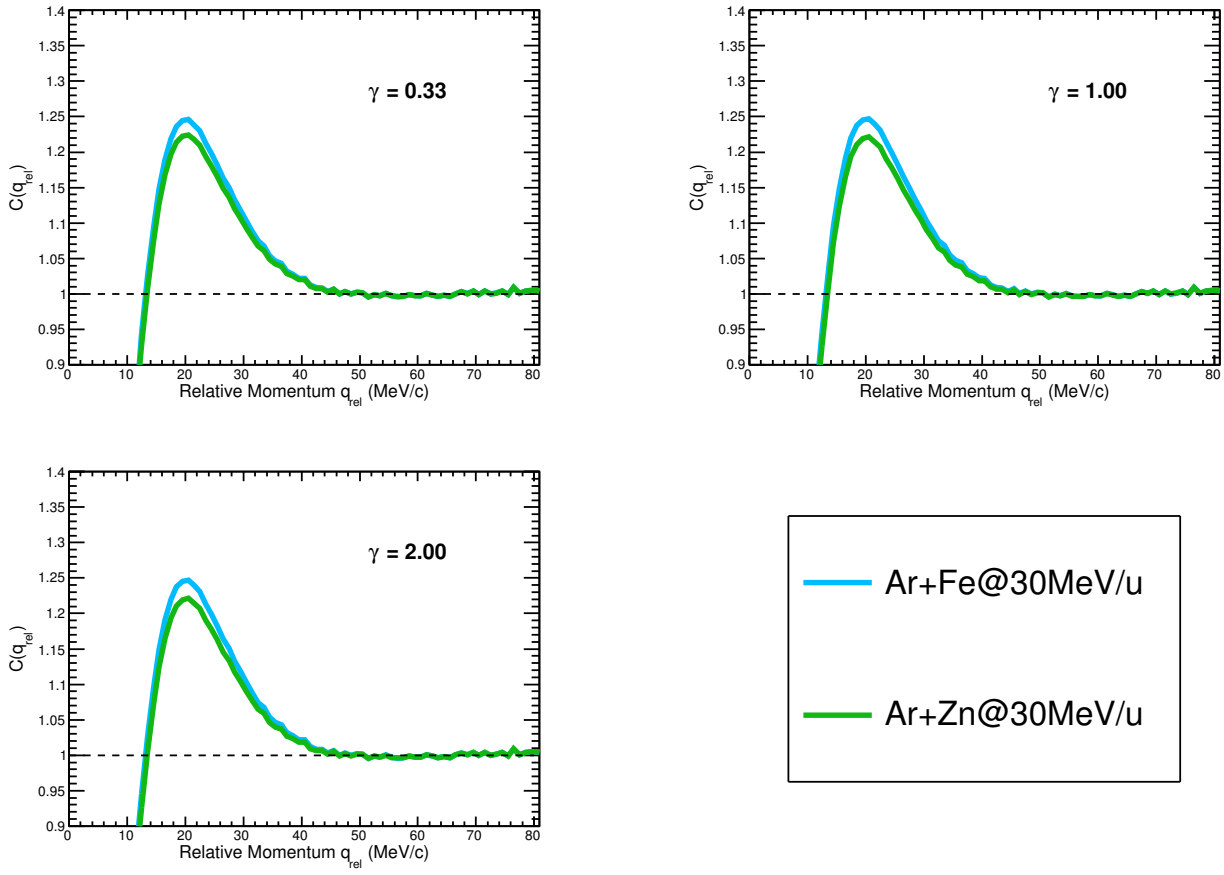

Figure 4.30: Comparison of correlation functions for the 30 MeV systems at impact parameter of 2 fm, considering only protons emitted before 100 fm/c.

the higher energy beam will result in a stronger correlation function. This is indeed the case both in the pBUU and the experimental data in the middle panel of figure 4.31. It is difficult to quantify the difference in amplitude for the two Ar+Fe correlation functions for the experimental data, but the difference is small, which is consistent with the small difference in correlation functions extracted from different parameterizations of the asymmetry energy for pBUU.

Figure 4.33 shows correlation functions extracted from pBUU for the 40 MeV/nucleon systems. The less neutron-rich system, Ca+Ni, shows a slightly stronger correlation function than the Ar+Fe in pBUU for all three γ parameters. For this energy and these equally sized systems, pBUU does not show a significant difference in the correlation functions calculated using the different

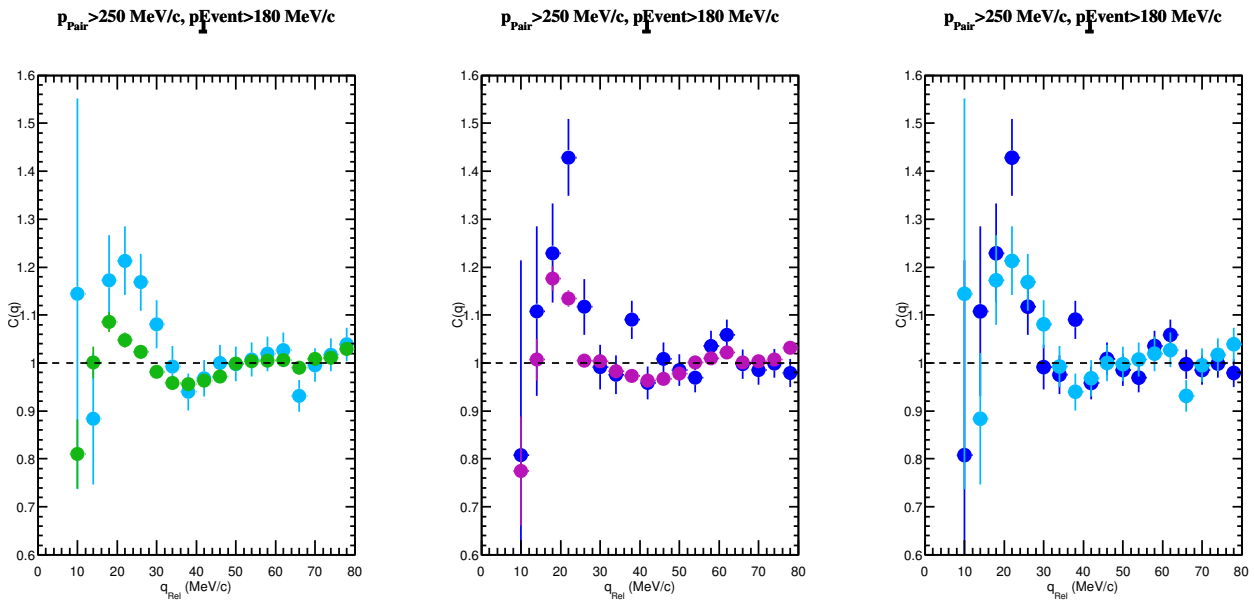

Figure 4.31: Proton-proton correlation functions featuring chosen cuts on the early momentum of the proton pair (250 MeV/c) and the violence of the collision (180 MeV/c). Both of the cuts are necessary in order to draw out the proton-proton interaction peak. From left to right: the 30 MeV/nucleon systems (Ar+Zn green, Ar+Fe cyan), 40 MeV/nucleon systems (Ca+Ni purple, Ar+Fe blue), and the Ar+Fe systems at 40 MeV/nucleon (blue) and 30 MeV/nucleon (cyan).

asymmetry energies. Because there is no variation, a conclusion cannot be drawn about a preferred asymmetry energy, but this does not contradict the conclusions drawn above. The experimental data in figure 4.31 shows a stronger correlation function for the Ar+Fe system than for the Ca+Ni. This observation is in agreement with previously published experimental studies showing a lower correlation function for the less neutron-rich system [26].

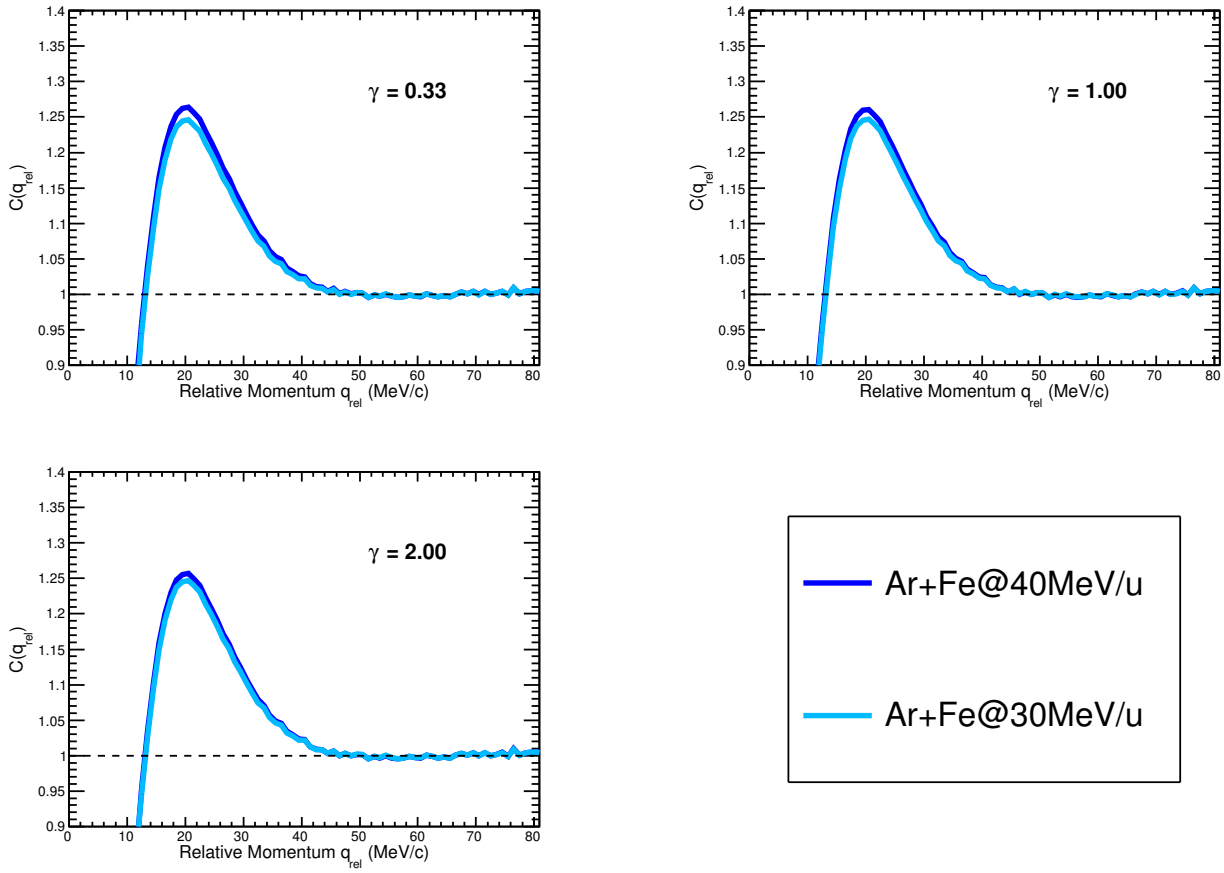

Figure 4.32: Comparison of correlation functions for the Ar+Fe systems at two energies for impact parameter of 2 fm, considering only protons emitted before 100 fm/c.

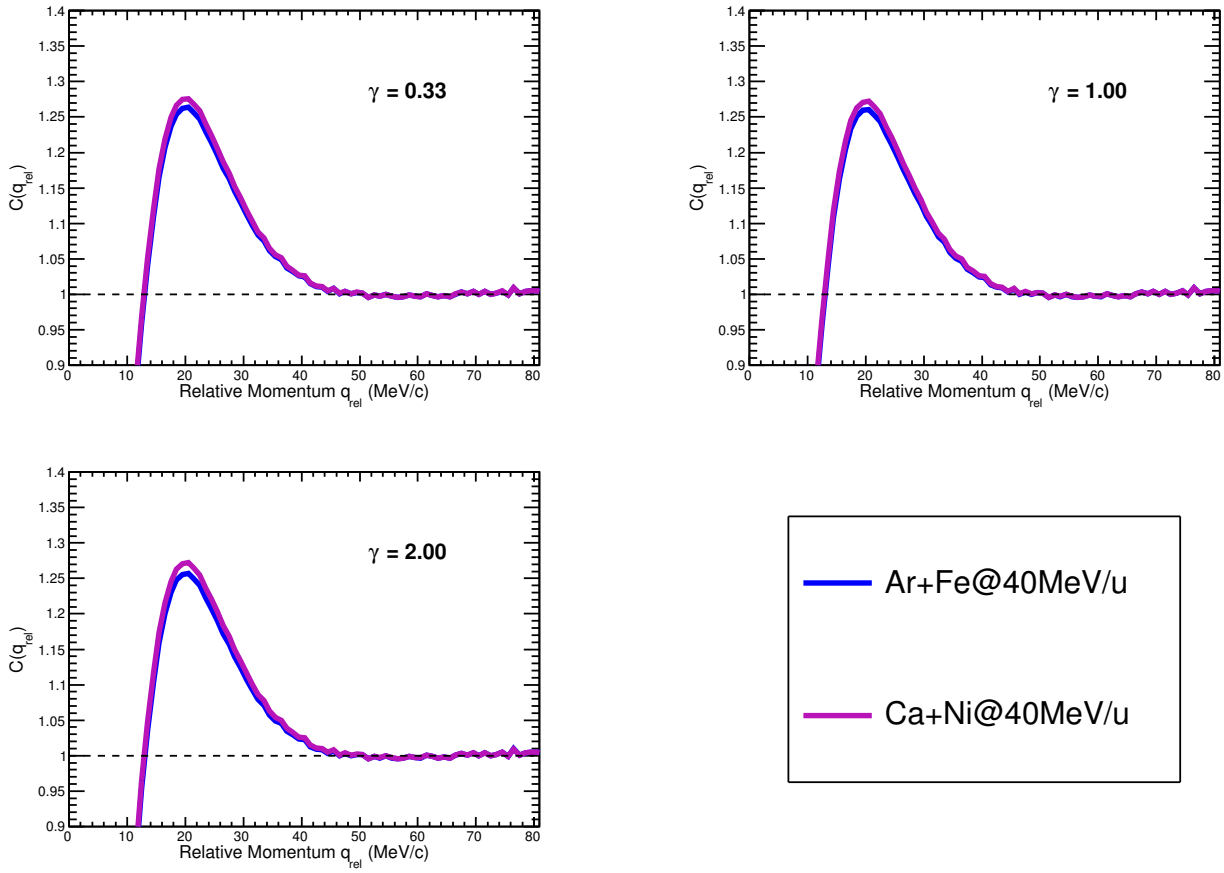

Figure 4.33: Comparison of correlation functions for the 40 MeV systems at impact parameter of 2 fm, considering only protons emitted before 100 fm/c.

5 CONCLUSIONS

5.1 Summary

The resolution and efficiency at low q_{Rel} of FAUST acheived in this experiment is sufficient to extract light charged particle correlation functions, particularly proton-proton correlation functions, which was the goal of this undertaking. Experimental data will always benefit from gathering more statistics, but the four systems included in this analysis (^{40}Ca+^{58}Ni at 40 MeV/nucleon, ^{40}Ar+^{58}Fe at 40 and 30 MeV/nucleon, ^{40}Ar+^{70}Zn at 30 MeV/nucleon) have sufficient data to consider the ordering of the strength of the proton-proton correlation functions when varying system (asymmetry and size) and beam energy. The correlation functions were selected for early emitted protons with a cut on the momentum of proton pairs and for central collisions with a cut on the transverse momentum of the event. The correlation functions to be compared with the transport model were selected from a cohort of cuts for early emitted protons and more violent collisions where the low q_{Rel} distributions had sufficient statistics to see the characteristic features of proton-proton correlation functions.

Correlation functions were also extracted from pBUU, which showed no dependence on the asymmetry energy at low impact parameter selected for early emitted (last collision before 100 fm/c) protons. All three parameterizations of γ produced correlation functions very close in shape and size for all four systems studied. No parameterizations were conclusively excluded in this work. In the future, the ordering of the strength of the correlation functions for systems of different beam energies and asymmetries (Δ) may be considered when investigating the asymmetry energy.

In order to extract this information, the angular resolution of the FAUST array was enhanced significantly by using a new style of position-sensitive dual-axis duolateral silicon detectors in every Si-CsI telescope. The new position-sensitive configuration along with the infrastructure established in this project and discussed herein (cabling, electronics, GUI, calibration methods) for running in this mode was used for the first time in this campaign. The slotted mask, designed for

use with the FAUST, has appropriately sized slits to verify the position calibration. The upgraded configuration has already been used in a subsequent experiment.

5.2 Outlook

This experiment focused on light charged particles (Z<3), which were solely used in this analysis. The data set includes particles up to Z<5 in many detectors. It may be useful to include these larger particles in further analysis, to more fully characterize the violence of events.

The correlation functions extracted from the systems with the same number of nucleons looked similar at the same energy. It would be interesting to run two systems of different sizes but similar asymmetries at a couple of different energies to separate out the dependencies upon system size and beam energy observed in this work. Transport model codes may offer some guidance here.

Position-sensitive FAUST can of course also be used to measure heavier particles. For future experiments, the slotted mask can provide a check and, if necessary, calibration of the position at which the particles strike detectors.

Now that we know we can extract correlation functions for light charged particles using position-sensitive FAUST, it would be intriguing to couple FAUST with neutron detectors with energetic and position resolution to extract neutron-proton (and neutron-neutron) correlation functions. These have been predicted to be even more sensitive to the asymmetry energy than the proton-proton correlation functions achieved here.

REFERENCES

[1] C. Horowitz and J. Piekarewicz, Phys. Rev. Lett. **86**, 5647 (2001).

[2] D. Youngblood, H. Clark, and Y.-W. Lui, Phys. Rev. Lett. **82**, 691 (1999).

[3] D. Youngblood, Nucl. Phys. A **687**, 1c (2001).

[4] V. Baran, M. Colonna, V. Greco, and M. D. Toro, Physics Reports **410**, 335 (2005).

[5] J. Lattimer and M. Prakash, Astrophys. J. **550**, 426 (2001).

[6] J. Lattimer and M. Prakash, Science **304**, 536 (2004).

[7] B.-A. Li, L.-W. Chen, and C. M. Ko, Physics Reports **464**, 113 (2008).

[8] P. Demorest *et al.*, Nature **467**, 1081 (2010).

[9] C. Fuchs and H. H. Wolter, Eur. Phys. J. A **30** (2006).

[10] J. Natowitz *et al.*, Phys. Rev. Lett. **104**, 202501 (2010).

[11] L. Chen, V. Greco, C. Ko, and B. A. Li, Phys. Rev. C **68** (2003).

[12] A. Michelson and A. Morley, Philos. Mag. S. **151**, 449 (1887).

[13] T. Young, Philos. Trans. R. Soc. Lond. **92**, 12 (1802).

[14] G. R. Fowles, *Introduction to Modern Optics*, 2nd ed. (Dover Publications, Inc., 1989).

[15] R. H. Brown and R. Q. Twiss, Nature **178**, 1046 (1956).

[16] D. H. Boal, C. Gelbke, and B. K. Jennings, Rev. Mod. Phys. **62**, 553 (1990).

[17] S. J. Gaff, *Two-proton and two-neutron correlation functions from intermediate-energy heavy-ion reactions*, Ph.D. thesis, Michigan State University, East Lansing, MI (1997).

[18] C. Davisson and L. H. Germer, Nature **119**, 558 (1927).

[19] G. Goldhaber, S. Goldhaber, W. Lee, and A. Pais, Phys. Rev. **120**, 300 (1960).

[20] S. Koonin, Phys. Lett. B **70**, 43 (1977).

[21] S. Pratt and M. B. Tsang, Phys. Rev. C **36**, 2390 (1987).

[22] G. Verde *et al.*, Eur. Phys. J. A **30**, 81 (2006).

[23] G. Verde *et al.*, Phys. Rev. C **65**, 054609 (2002).

[24] K. M. Watson, Phys. Rev. **88**, 1163 (1952).

[25] B. J. Morton, E. E. Gross, E. V. Hungerford, J. J. Malanify, and A. Zucker, Phys. Rev. **169**, 825 (1968).

[26] R. Ghetti *et al.*, Nucl. Phys. A **765**, 307 (2006).

[27] R. Ghetti, C. Collaboration, *et al.*, Nucl. Phys. A **674**, 277 (2000).

[28] V. Henzl *et al.*, Phys. Rev. C **85**, 014606 (2012).

[29] D. A. Brown and P. Danielewicz, Phys. Lett. B **398**, 252 (1997).

[30] L. Chen, V. Greco, C. Ko, and B. Li, Phys. Rev. Lett. **90** (2003).

[31] G. Kopylov, Phys. Lett. **50B**, 472 (1974).

[32] W. G. Lynch *et al.*, Phys. Rev. Lett. **51**, 1850 (1983).

[33] J. Pochodzalla *et al.*, Phys. Lett. B **174**, 36 (1986).

[34] J. Pochodzalla *et al.*, Phys. Rev. C **35**, 1695 (1987).

[35] P. Chomaz, M. Colonna, A. Guarnera, and J. Randrup, Phys. Rev. Lett. **73**, 3512 (1994).

[36] M. Parlog *et al.*, Eur. Phys. J. A **25**, 223 (2005).

[37] M. Colonna, P. Chomaz, A. Guarnera, and B. Jacquot, Phys. Rev. C **51**, 2671 (1995).

[38] G. Tabacaru, I. Collaboration, *et al.*, Nucl. Phys. A **764**, 371 (2006).

[39] H. Sorge, H. Stocker, and W. Greiner, Nucl. Phys. A **498**, 567c (1989).

[40] H. Boggild *et al.*, Phys. Lett. B **458**, 181 (1999).

[41] D. A. Brown and P. Danielewicz, Phys. Rev. C **64**, 014902 (2001).

[42] M. Kilburn, *Proton-proton correlation functions as a probe to reaction dynamics*, Ph.D. thesis, Michigan State University (2011).

[43] A. L. Keksis, *N/Z equilibration in deep inelastic collisions and the fragmentation of the resulting quasiprojectiles*, Ph.D. thesis, Texas A&M University (2007).

[44] S. Soisson *et al.*, Nucl. Instr. and Meth. A **613**, 240 (2010).

[45] G. Engel *et al.*, Nucl. Instr. and Meth. A **573**, 418 (2007).

[46] R. Todd, RIS-Corp, 5905 Weisbrook Lane, Suite 102 Knoxville, TN 37909 (2013).

[47] C. Northcliffe and R. Schilling, Nucl. Data Tables A7 **233** (1970).

[48] F. Hubert, R. Rimbot, and H. Gauvin, Atom. Data and Nucl. Data Tables **46**, 1 (1990).

[49] The Stopping and Range of Ions in Matter (2018 (accessed July 2018)), https://www.srim.org.

[50] M. Youngs, *Using light emitted clusters as a probe of the symmetry energy in the nuclear equation of state*, Ph.D. thesis, Michigan State University (2013).

[51] M. Parlog *et al.*, Nucl. Instr. and Meth. A **482**, 693 (2002).

[52] D. Lacroix, A. V. Lauwe, and D. Durand, Phys. Rev. C **69** (2004).

[53] National Nuclear Data Center, Brookhaven National Laboratory (2018 (accessed July 2018)), https://www.nndc.bnl.gov/.

[54] J. Gauthier *et al.*, Phys. Rev. C **90**, 034618 (2014).

[55] R. Ghetti and J. Helgesson, Nucl. Phys. A **752**, 480c (2005).

[56] P. Danielewicz and G. Bertsch, Nucl. Phys. A **533**, 712 (1991).

[57] P. Danielewicz, Nucl. Phys. A **545**, 21c (1992).

[58] P. Danielewicz, arXiv:nucl-th/020132v1 (2002).

[59] E. Uehling and G. Uhlenbeck, Phys. Rev. C **43**, 552 (1933).

[60] B. Barker, Private communication (2015-2018).

[61] L. Shi, *Transport phenomena in heavy-ion reactions*, Ph.D. thesis, Michigan State University (2003).

APPENDIX A

TOWER BOARDS AND OTHER DIAGRAMS FROM FAUST CABLING UPGRADE

The adapter boards from section 2.3 are depicted schematically in figure A.1.

These boards were made in four layers, to minimize cross-talk between the signals. Each of the four layers are depicted separately in figures A.2, A.3, A.4 and A.5. This board took the four detector cables and condensed them spatially to 24 channels on a very low capacitance ribbon cable, well shielded with grounding braid, inside of the chamber, which then attached to the feedthrough on the upstream end of the FAUST chamber. The cables were kept as short as possible.

The DADL detectors were biased as shown in table 2.5 and figure 2.12. The boards to facilitate this and connect to the preamplifiers are the "tower boards", which go inside of the tower boxes. The layers for these boards are depicted in figures A.7, A.8, A.9, A.10, A.11, A.12, and A.13.

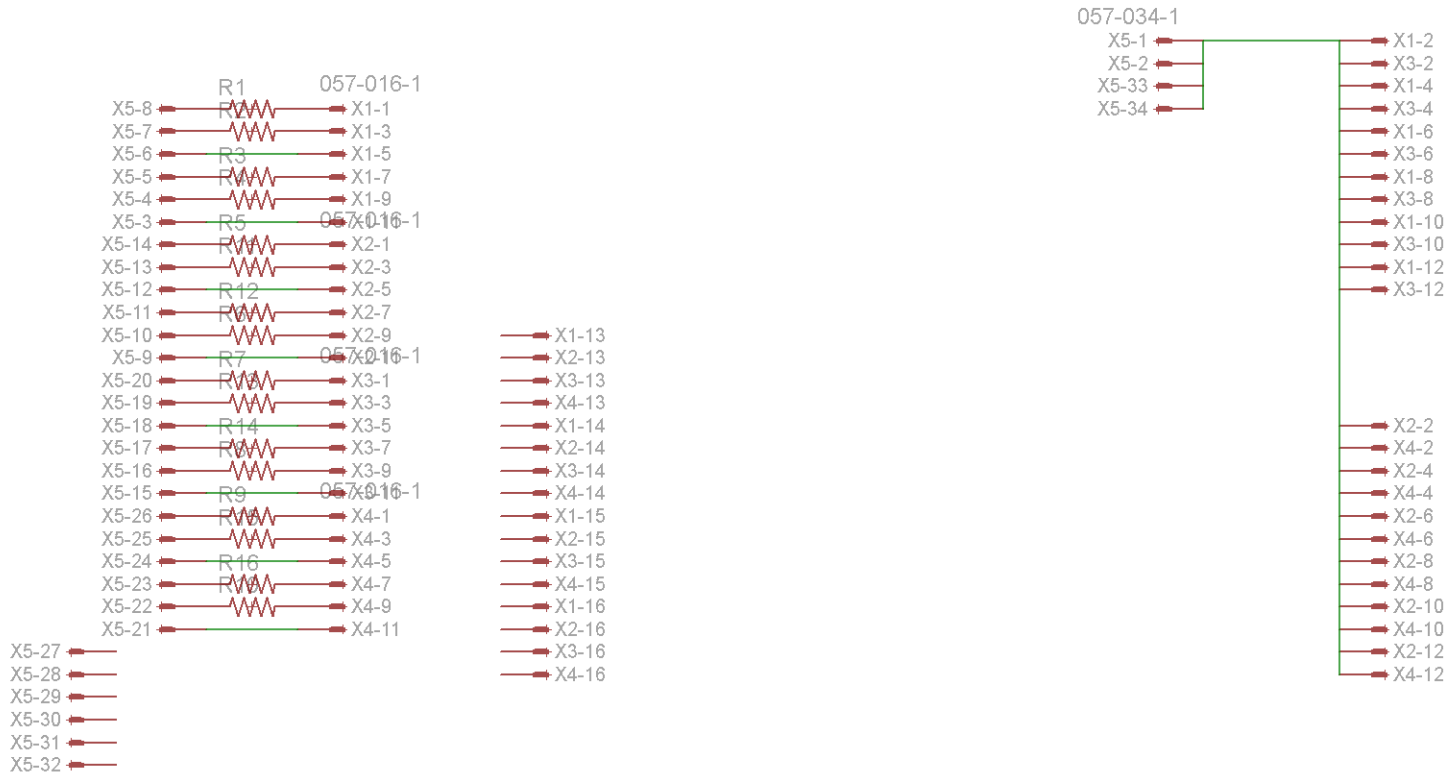

Figure A.1: Eagle layout of the logic for the adapter board.

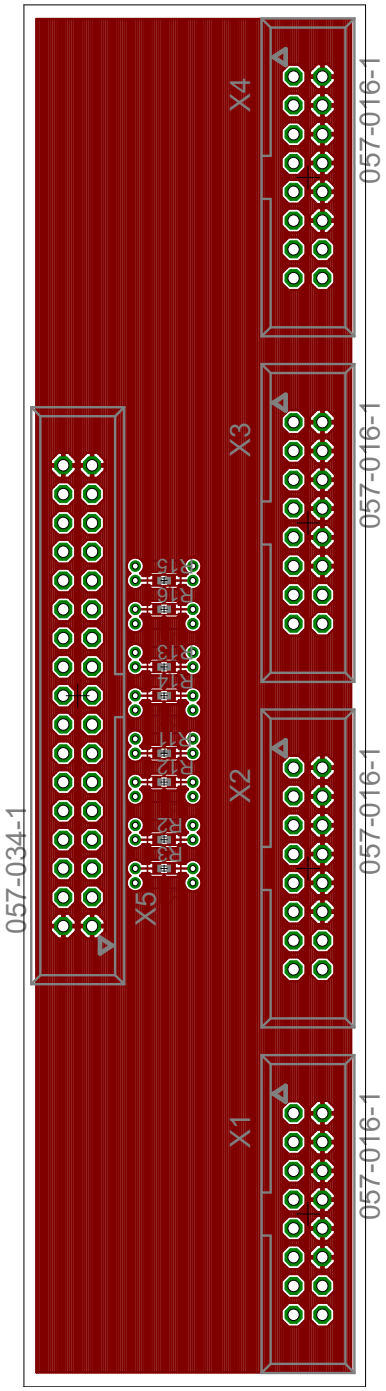

Figure A.2: Layer 1 of the adapter board.

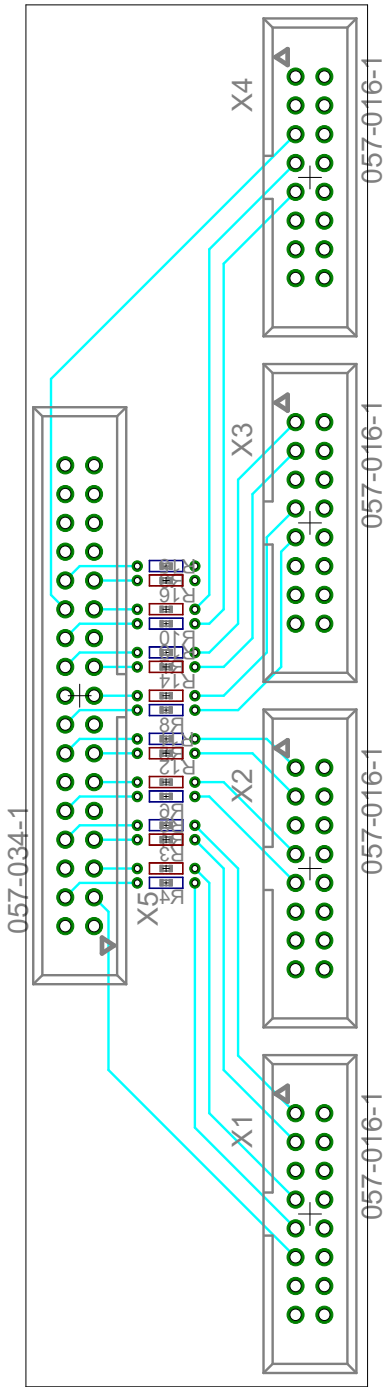

Figure A.3: Layer 2 of the adapter board.

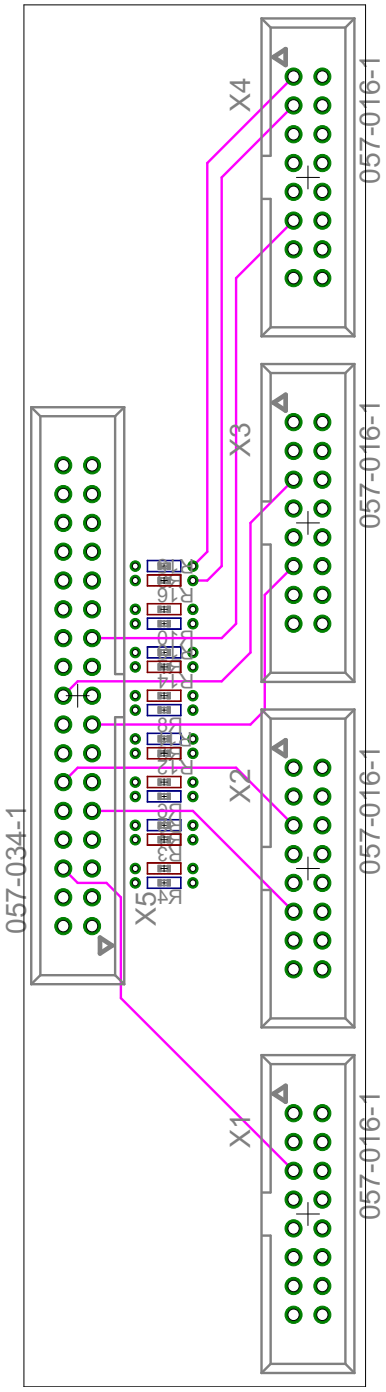

Figure A.4: Layer 3 of the adapter board.

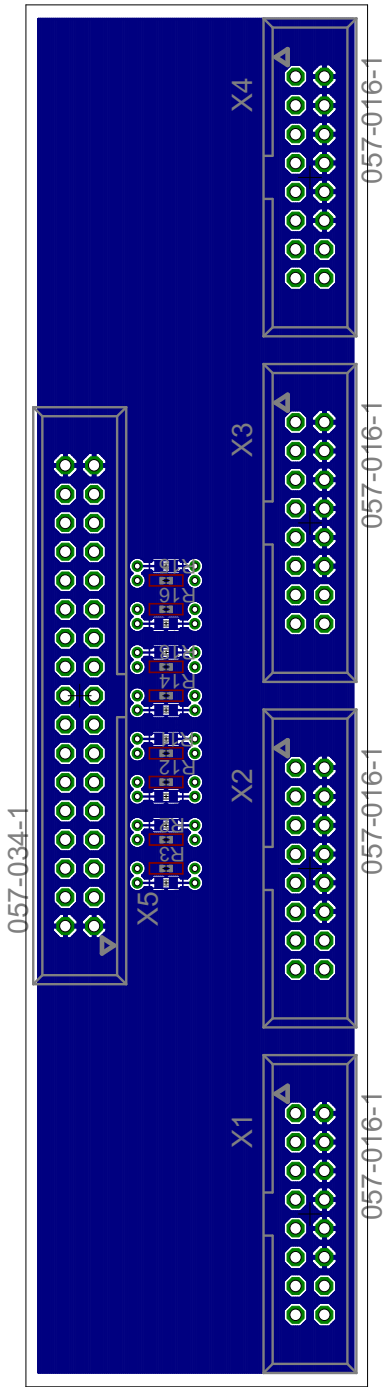

Figure A.5: Layer 4 of the adapter board.

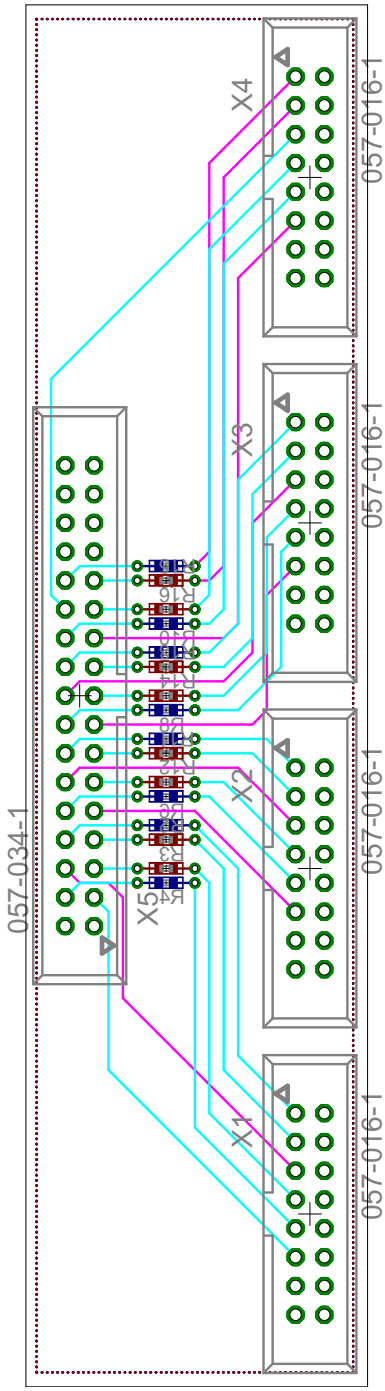

Figure A.6: Adapter Board–The ribbon cable that brought bias from the chamber feed-through to the adapter board.

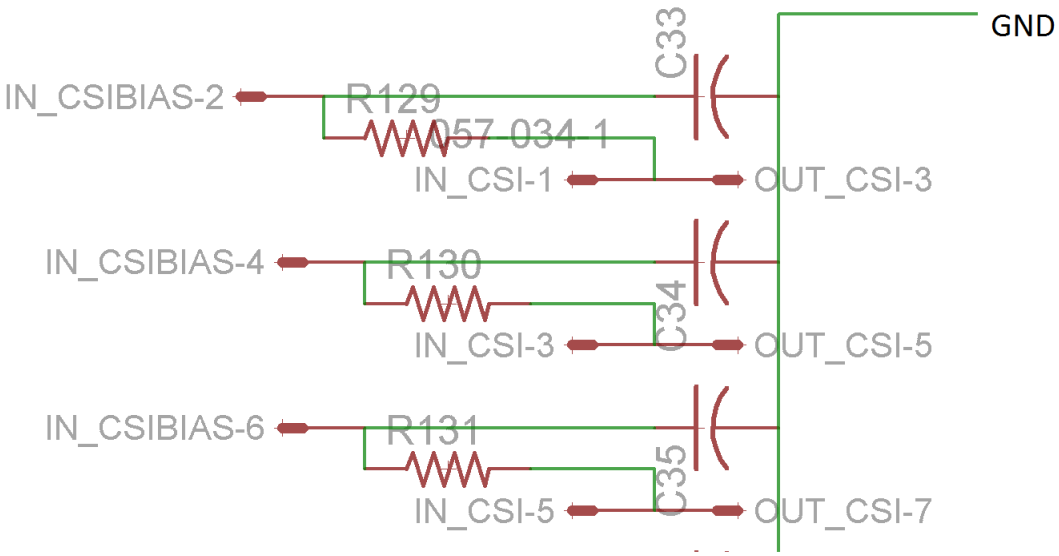

Figure A.7: Logic for CsI's on the tower board.

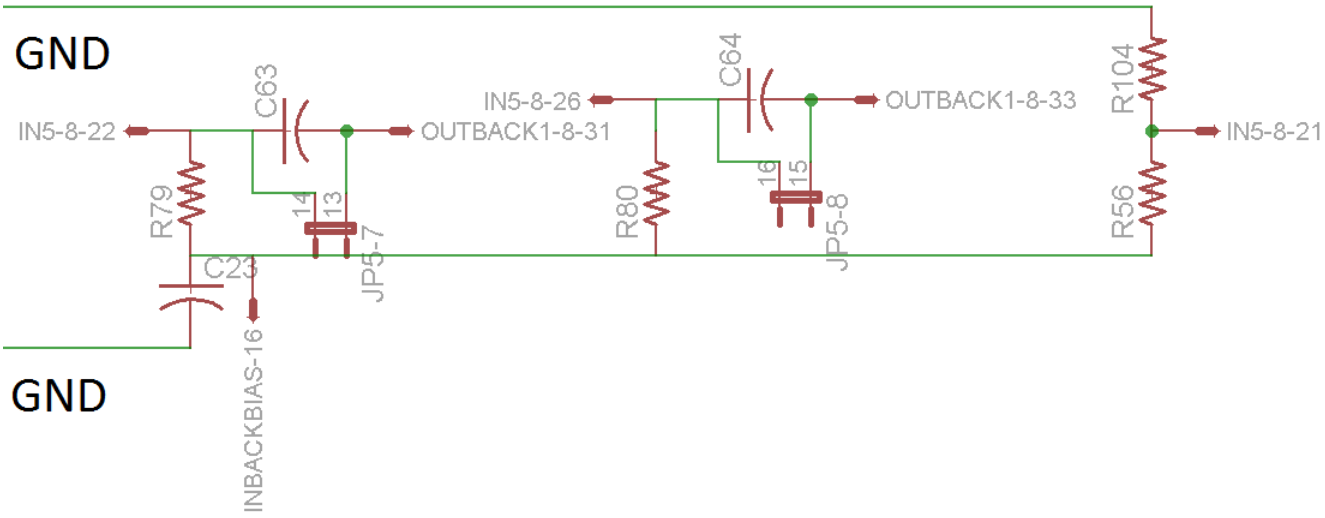

Figure A.8: Logic for Si's on the tower board.

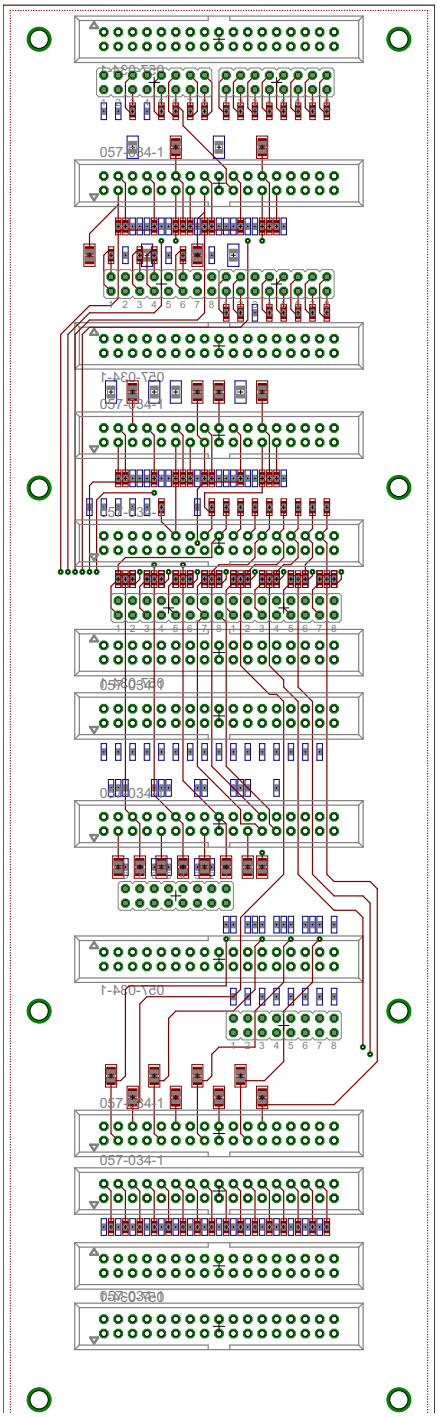

Figure A.9: Layer 1 of the tower board.

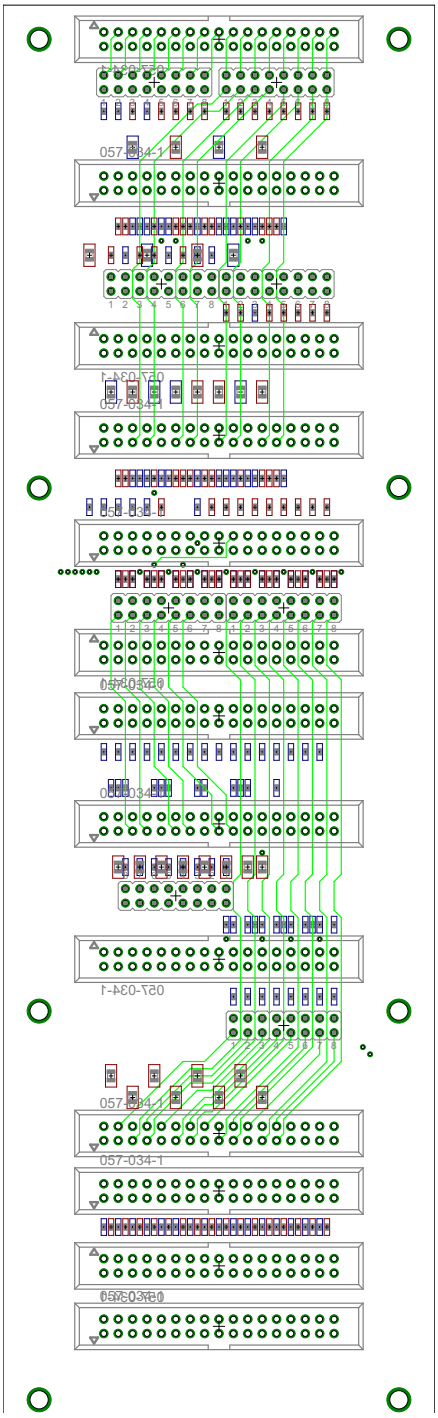

Figure A.10: Layer 2 of the tower board.

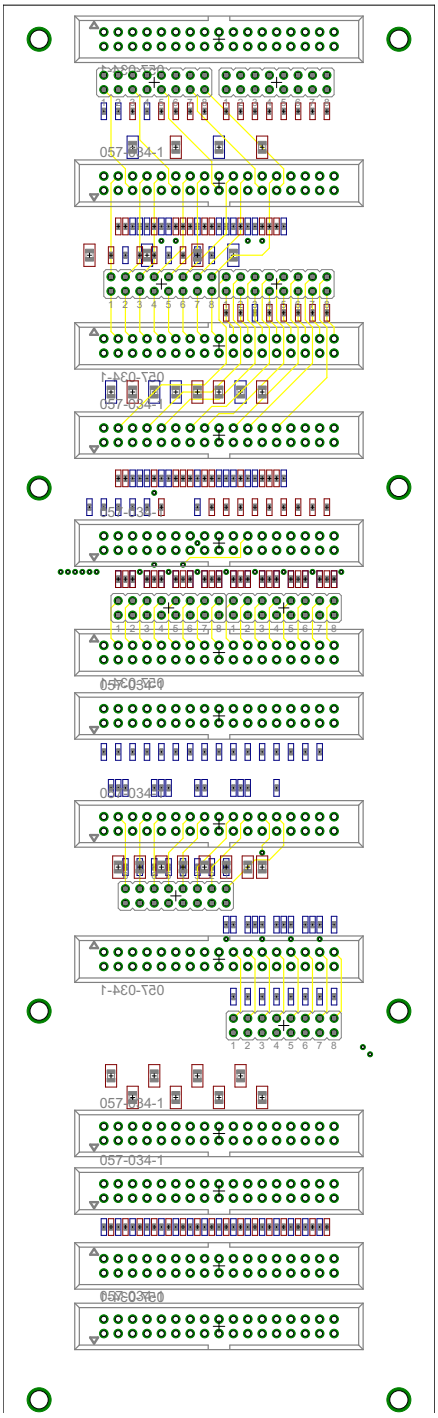

Figure A.11: Layer 3 of the tower board.

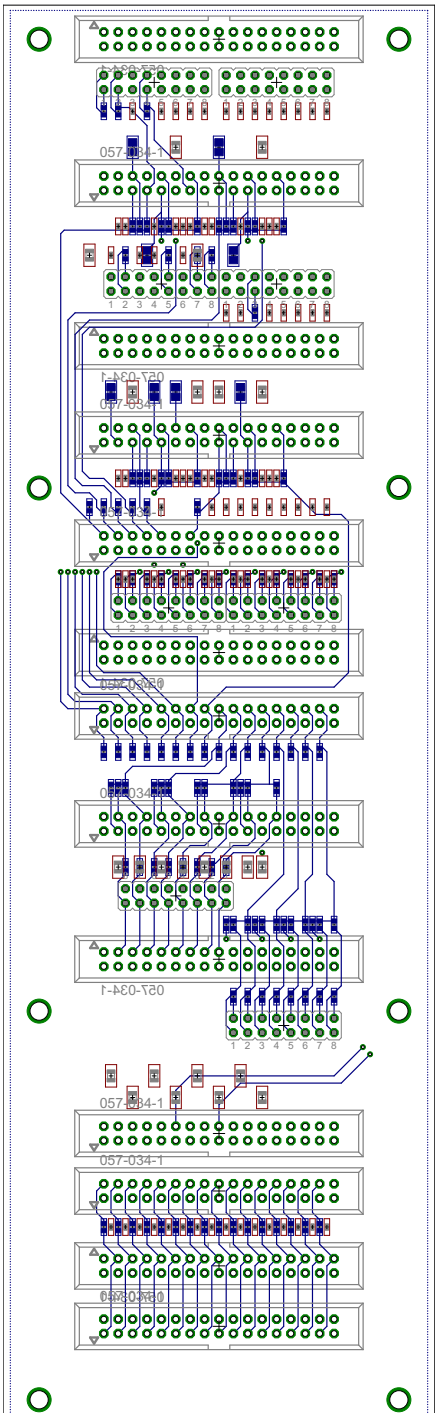

Figure A.12: Layer 4 of the tower board.

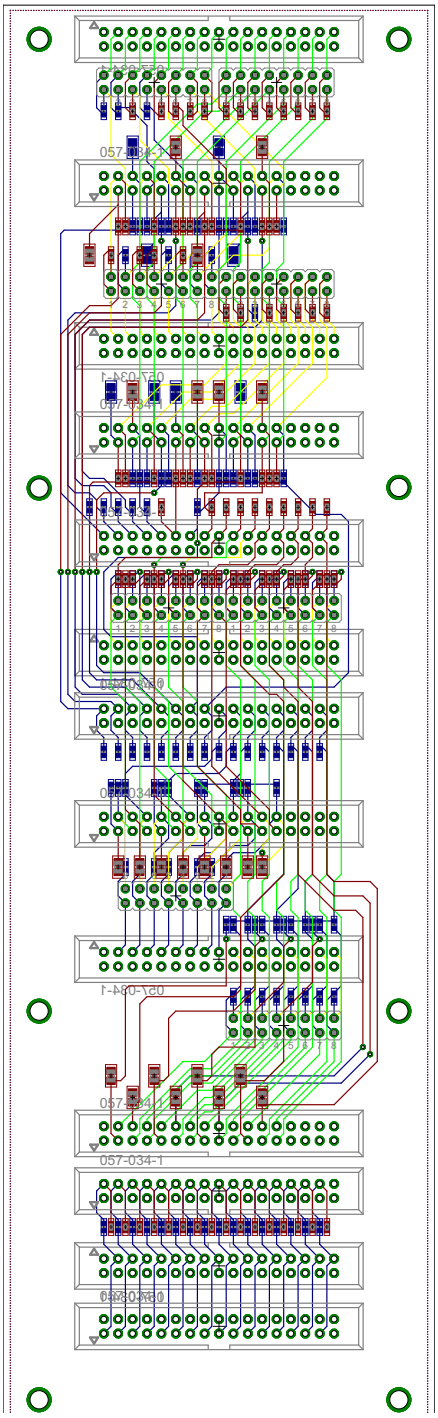

Figure A.13: All layers of the tower board.

APPENDIX B

DADL NUMBERS

Table B.1: Serial numbers from Micron and SJY group Detector number.

Detector	Thickness (μm)	PC board #	Micron # (3006−)
0	316	25	11−2
1	311	21	10−6
2	324	18	15−7
3	311	22	10−7
4	324	19	15−8
5	311	23	10−8
6	310	20	16−2
7	316	24	11−1
8	314	50	13−6
9	324	42	17−2
10	325	43	14−4
11	320	51	9−8
12	324	44	15−1
13	324	45	15−2
14	324	52	17−5
15	317	46	12−4
16	324	47	15−5
17	324	53	17−6
18	310	48	16−7
19	310	49	16−5

Detector	Thickness (μm)	PC board #	Micron # (3006−)
20	317	13	5−3
21	316	5	8−3
22	321	1	4−5
23	324	6	17−7
24	324	17	15−6
25	314	14	2−3
26	324	2	17−4
27	320	8	9−5
28	314	15	2−4
29	320	9	9−2
30	317	3	5−1
31	315	10	7−2
32	322	70	1−2
33	322	71	1−3
34	316	4	8−2
35	316	12	8−6

Detector	Thickness (μm)	PC board #	Micron # (3006−)
36	314	38	2−8
37	315	30	7−6
38	325	26	14−5
39	314	31	2−5
40	314	39	2−1b
41	321	32	4−4
42	317	27	12−3
43	321	33	4−3
44	325	40	14−2
45	310	34	16−1
46	311	28	10−5
47	324	35	15−3
48	322	69	1−1
49	314	36	13−5
50	314	29	13−1
51	314	37	2−6

Detector	Thickness (μm)	PC board #	Micron # (3006−)
52	316	65	11−3
53	317	58	5−2
54	311	57	10−3
55	322	72	1−4
56	320	66	9−4
57	316	59	8−5
58	322	73	1−5
59	322	74	1−6
60	317	68	5−4
61	314	61	13−8
62	314	55	2−2
63	317	62	12−1
64	320	67	9−1
65	324	64	17−1
66	314	54	2−1a
67	316	63	11−6